Vysoká škola báňská - Technická univerzita Ostrava
Univerzitní studijní programy
Institut fyziky

Structural, optic and magnetooptic properties of epitaxial thin film ferrites

Strukturní, optické a magnetooptické vlastnosti epitaxních tenkých vrstev feritů

Autor: Bc. Michaela Tomíčková
Vedoucí diplomové práce: Mgr. Jaroslav Hamrle, Ph.D.
Místo, datum odevzdání: Ostrava, 16. 05. 2016

Místopřísežné prohlášení

Prohlašuji, že jsem diplomovou práci vypracovala samostatně pod vedením vedoucího diplomové práce a že všechny použité podklady a literární zdroje jsem správně a úplně citovala.

V Ostravě dne 16. 05. 2016 .....

podpis studenta

Prohlašuji, že,

- jsem byla seznámena s tím, že se na mou diplomovou práci plně vztahuje zákon č.121/2000 Sb., autorský zákon, zejména §35 - užití díla v rámci občanských a náboženských obřadů, v rámci školních představení a užití díla školního a §60 - školní dílo.
- beru na vědomí, že Vysoká škola báňská - Technická univerzita Ostrava (dále jen VŠB - TUO) má právo nevýdělečně ke své vnitřní potřebě diplomovou práci užít (§35 odst. 3).
- souhlasím s tím, že diplomová práce bude v elektronické podobě uložena v Ústřední knihovně VŠB - TUO k nahlédnutí a jeden výtisk bude uložen u vedoucího diplomové práce. Souhlasím s tím, že údaje o diplomové práci budou zveřejněny v informačním systému VŠB-TUO.
- bylo sjednáno, že s VŠB - TUO, v případě zájmu z její strany, uzavřu licenční smlouvu s oprávněním užít dílo v rozsahu §12 odst. 4 autorského zákona.
- bylo sjednáno, že užít své dílo - diplomovou práci nebo poskytnout licenci k jejímu využití mohu jen se souhlasem VŠB - TUO, která je oprávněna v takovém případě ode mne požadovat přiměřený příspěvek na úhradu nákladů, které byly VŠB - TUO na vytvoření díla vynaloženy (až do jejich skutečné výše).
- beru na vědomí, že odevzdáním své práce souhlasím se zveřejněním své práce podle zákona č.111/1988 Sb., o vysokých školách a o změně a doplnění dalších zákonů (zákon o vysokých školách), ve znění pozdějších předpisů, bez ohledu na výsledek její obhajoby.

V Havířově dne 16. 05. 2016 .....

Jméno a příjmení studenta

Acknowledgements

I would like to express my deep gratitude to my supervisor Mgr. Jaroslav Hamrle Ph.D. for very helpful, constructive advices and last but not least for his friendly approach.

I would like to extend a very honest "thank you" to Prof. Dr. Joachim Wollschläger from University in Osnabrück in and to all members of his working group. The time spent at university in his laboratories during preparation of epitaxial thin films and their characterization was very beneficial for me.

Finally, I thank to my parents and all who supported me with my thesis and during study.

Abstrakt

Cílem práce je příprava epitaxních tenkých vstev feritů a jejich následná strukturní a optická charakterizace. Budou připraveny vstvy magnetických feritů (např. magnetit (Fe_3O_4), nikl-feritu ($NiFe_2O_3$) nebo kobalt-feritu ($CoFe_2O_3$)) na monokrystalických substrátech MgO nebo $SrTiO_3$ pomocí reaktivní epitaxe z molekulárních svazků. Struktura těchto vrstev bude určena pomocí XRD a LEED. Optické a magnetooptické vlastnosti pak budou spektroskopicky charakterizovány pomocí elipsometrie a magnetooptické spektroskopie, což umožní určit spektra tenzoru permitivity těchto materiálů.

Bibliografická citace

TOMÍČKOVÁ, Michaela, Bc. *Strukturní, optické a magnetooptické vlastnosti epitaxních tenkých vrstev feritů.* Ostrava, 2016. 100 s. Diplomová práce. Vysoká škola báňská - Technická univerzita Ostrava. Vedoucí práce Mgr. Jaroslav Hamrle, Ph.D.

Abstract

The goal of thesis is preparation of epitaxial thin films of ferrites, and their subsequent structural and optical characterization. The ferrites films (e.g. magnetite (Fe_3O_4), nickel-ferrite ($NiFe_2O_3$) and cobalt-ferrite ($CoFe_2O_3$)) will be deposited on monocrystalline substrates MgO or $SrTiO_3$ using reactive molecular beam epitaxy. The film structure will be determined using XRD and LEED. Optic and magnetooptic properties will be spectroscopically characterized by ellipsometry and magnetooptic spectroscopy, allowing to determine spectra of permittivity tensor of those materials.

Bibliographic citation

TOMÍČKOVÁ, Michaela, Bc. *Structural, optic and magnetooptic properties of epitaxial thin film ferrites*. Ostrava, 2016. 100 p. Diploma thesis. VŠB - Technical university of Ostrava. Supervisor Mgr. Jaroslav Hamrle, Ph.D.

Contents

1 Introduction

The focus of this thesis is preparation of epitaxial thin films of magnetite and Ni-ferrite on MgO(001) substrate. Magnetite and ferrites are iron oxides, exhibiting an inverse spinel structure. These layers were prepared using reactive Molecular Beam Epitaxy that enables epitaxial growth of the layers. In epitaxy the lattice parameter of substrate must be similar to lattice parameter of deposited layer. For example, the lattice parametr of magnetite is twice large then lattice parameter of MgO that has rocksalt structure. Furthermore, the lattice mismatch is only 0.33 %. Therefore, MgO(001) substrate is suitable to prepare of layers crystallizing at the inverse spinel structure.

The layers of magnetite and Ni-ferrire were prepared at University in Osnabrück in working group that is led by Prof. Dr. Joachim Wollschläger. The prepared layers were characterized there using Vibrating Sample Magnetometry, X-Ray Photoelectron Spectroscopy and X-Ray Reflection technique. At the Technical university of Ostrava the prepared samples were measured using Ellipsometric Spectroscopy and Magneto-optical Spectroscopy.

In the first part of this thesis basic information about iron and its oxides are introduced. The epitaxial thin films were prepared and therefore the information about nanomaterials, namely thin films and corresponding techniques of preparation are described.

In the end of the theoretical part the used techniques are described to a better understanding of the results. In the experimental part, the results of used techniques are described and evaluated.

2 Theoretical part

2.1 Iron and its oxides

Iron is technically the most important metal. It has a wide range of applications at production of alloys and at production of large amount of technical means used by man. Iron is a transition metal with chemical symbol Fe. Chemically pure iron is lustrous metal, relatively soft, ductile and malleable. Nevertheless, addition of only very small amount of carbon to pure iron, changes significantly properties of pure iron. Iron is chemically considerably unstable and reactive. It dissolves readily with mineral acids. Atomic nucleus of iron has the highest binding energy of all known elements. [1]

We can find a several allotropic forms of pure iron. In solid state, three allotropic forms of iron are distinguished. The first form of iron is $\alpha-$Fe. This modification crystallizes in body-centered cubic lattice (bcc) (Fig. 2.1). The $\alpha-$Fe is stable until temperature 906 °C. The lattice parameter a of the $\alpha-$Fe is dependent on temperature. At 20 °C the lattice parameter a equals 2.8664 Å. The second form of iron crystallizes in face-centered cubic lattice (fcc). This form occurs in temperature range from 906 to 1401 °C, denoted $\gamma-$Fe. The lattice parameter a of $\gamma-$Fe equals 3.6468 Å at 916 °C. Above the 1401 °C Fe again transfers to bcc lattice. This high-temperature form of iron is called $\delta-$Fe. [2]

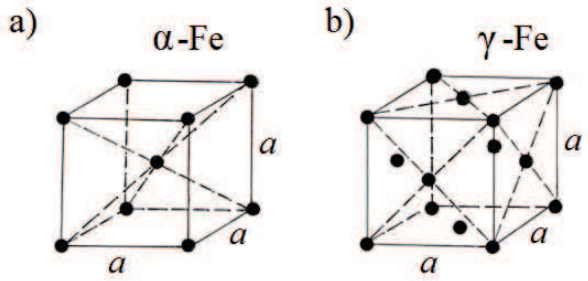

Figure 2.1: *a) Body-centered cubic lattice (bcc) that is typical for $\alpha-$Fe. b) Face-centered cubic lattice (fcc), beings structure of $\gamma-$Fe.* [3]

The Curie's temperature of iron is 768 °C. It means that $\alpha-$Fe is ferromagnetic below this temperature. Above this temperature all forms of iron are marked $\beta-$Fe and they are paramagnetic. The Curie's point is on the curve of heating and cooling accompanied by a time delay. Time delay is also observed at points 991 °C, 1392 °C,

leading to structural changes of iron (Fig. 2.2). [1, 4]

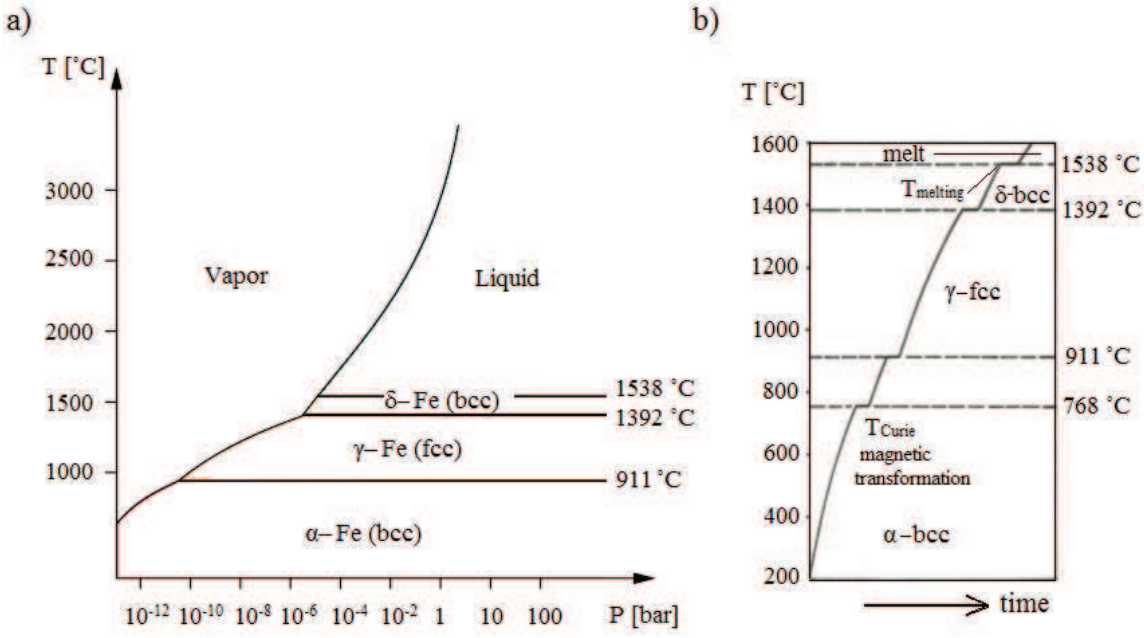

Figure 2.2: *a) The phase diagram of Fe. b) The dependence of temperature on time, showing heating of Fe by the constant power. The steps (time delays) correspond to either phase or structural transformation* [4]

Iron has atomic number 26. The electron configuration of this element is $3d^6$ $4s^2$ and its valence electrons are in d orbital. This element has 8 oxidation states (-IV, -II, I, II, III, IV, V, VI). [2]

Organic and anorganic compounds of iron are very significant and widely used. Anorganic compounds of iron occur predominantly in oxidation state II and III. Compounds with oxidation state -II, I, IV, V and VI are less stable than compounds with oxidation state II or III. Compounds with oxidation state II are denoted as ferrous. Compounds with oxidation state III are then called as ferric. We can also find compounds of iron containing two types of oxidation states of Fe, namely II and III oxidation states. This combination of iron atoms with two oxidation states and oxygen in one compound is denoted magnetite. The goal of this thesis was prepare thin films of magnetite and nickel-ferrite. The next chapter we will introduce with these materials.

2.1.1 Magnetite

Magnetite is a mineral that ordinarily occurs in the nature. This material has strong magnetism and typically black color. Large crystals of magnetite can be found in the nature, being very stable. This is in contrast for example with nanoparticles of magnetite. Synthetic nanoparticles of magnetite with the size smaller than 100 nm oxidate already during synthesis, if suitable passivating compounds are not used. [5]

The chemical formula of magnetite is Fe_3O_4. Magnetite contains both Fe^{2+} and Fe^{3+} ions. We can also write formula of magnetite as $FeO \cdot Fe_2O_3$. Magnetite contains two types of ions of iron with oxidation number 3+ and one ion with oxidation number 2+. Therefore, the magnetite can be also denoted as ferrous - ferric oxide (Fig. 2.3). The formula can then be written as $Fe^{2+}Fe_2^{3+}O_4$.

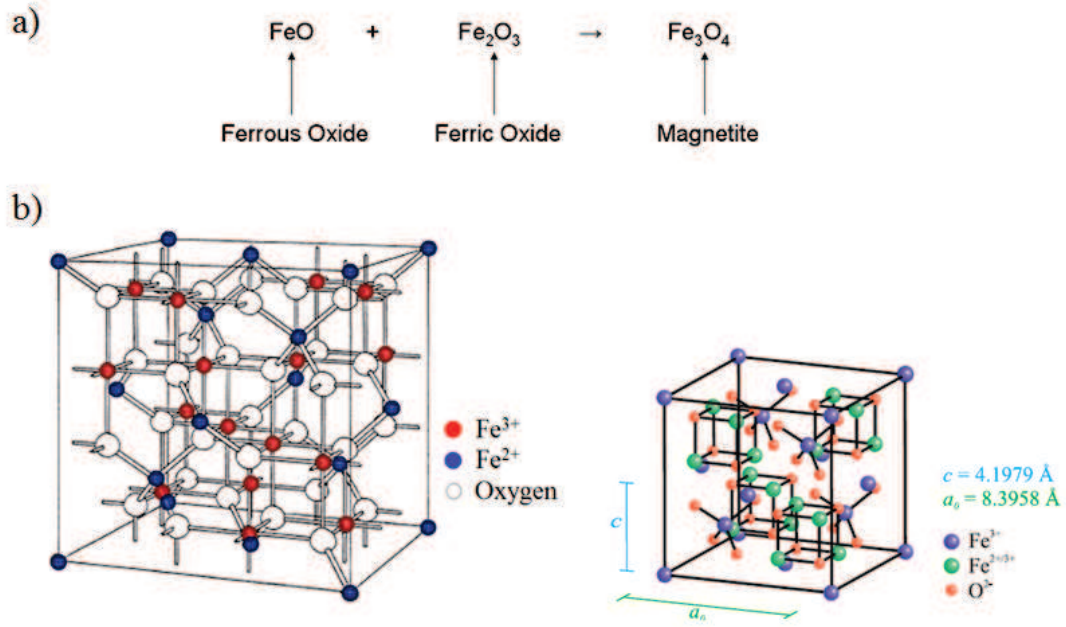

Figure 2.3: *a) The schematic chemical equation of magnetite that contains ferrous and ferric oxides. b) Two sketches of the inverse spinel structure of magnetite and corresponding lattice parameters of the structure are illustrated below in the figure.* [5]

Crystalographic structure of magnetite is a cubic inverse spinel structure without any vacancies, in the contrast with maghemite. Maghemite contains only ferrous ions Fe^{3+} in spinel structure and the chemical formula of maghemite is $\gamma - Fe_2O_3$.

In the spinel structure of magnetite (Fig. 2.3), the atoms of oxygen occupy fcc lattice. Between oxygen atoms are Fe^{3+} ions on the tetrahedral site. Ions Fe^{3+} and Fe^{2+} are on the octahedral site in antiparallel arrangement. [6]

Magnetite is ferrimagnetic with Curie's temperature 858 K. Structure of ferrimagnetic materials is very similar to structure of antiferromagnetic materials. In ferromagnetic materials the electron spins (the magnetic moments) are arranged in same direction. The spins in anti-ferromagnetic materials are arranged in opposite directions and resulting magnetic moment is zero. The spins in ferrimagnetics are also aligned in opposite directions, but not with the same magnitude, providing non-zero magnetic moment (Fig. 2.4). The Fe^{3+} ions at antiparallel positions in tetrahedral (A) and octahedral (B) sites provide zero magnetic moment. The magnetic moment of unit cell is caused only by Fe^{2+} ions, wherein each of the ions has magnetic moment 4 μ_B. The magnetic moment per unit cell is thus equal to 24 μ_B and 4 μ_B per formula unit (f.u.). [1, 7]

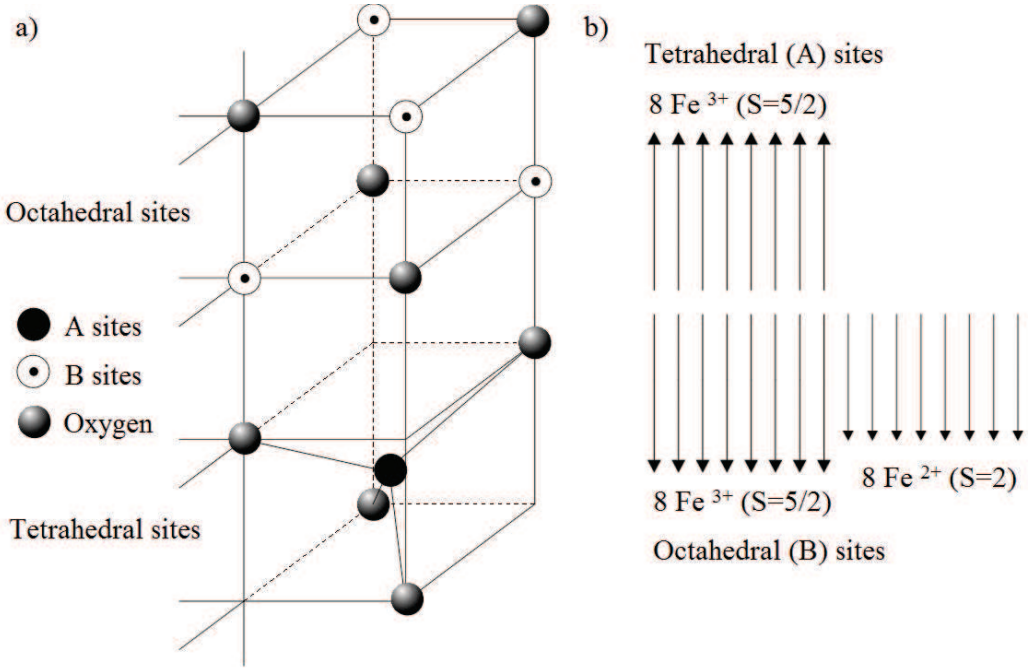

Figure 2.4: *a) Tetrahedral and octahedral sites of magnetite structure and b) corresponding ferrimagnetic arrangement of electron spins in a unit cell of magnetite.* [7]

Magnetic properties change with decreasing size of magnetite. With decreasing size of magnetite, the number of magnetic domains is also decreasing. When we achieve the critical size, the particle of magnetite starts to behave as monodomain. At this critical size, quantum effects such as superparamagnetism start to appear. The critical size is usually around 128 nm. Magnetite is usually electrically conductive. [8, 9]

2.1.2 Ferrite

Ferrites are very interesting material group. They have large applications mainly in transformers and electromagnetic cores as conductor of magnetic field due to their high Curie's temperature, high saturation magnetization, low conductivity and possibility to have low coercivity. The general formula of ferrites is $M^{2+}Fe^{3+}{}_2O_4$. The element M^{2+} are usually transition metal elements, for example Ni^{2+}, Zn^{2+}, Co^{2+}, Fe^{2+}, Mn^{2+} or element Mg^{2+}. Ferrites have spinel structure (Fig. 2.5), same as magnetite. Ferrites are also called ceramic compounds. [8, 10]

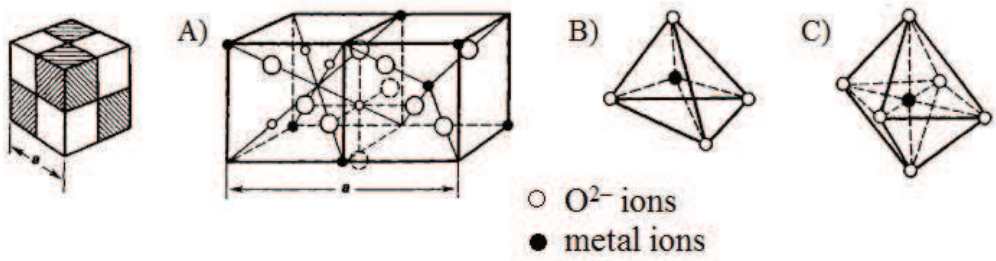

Figure 2.5: *The arrangement of ions in spinel structure of ferrite. On the left side we can see shematic representation of the unit cell, which is dived to 8 octants. There are drawn A) O^{2-} ions and metal ions in octahedral and tetrahedral sites, B) metal ions in a tetrahedral site and C) metal ions in an octahedral site.* [11]

The ferrites are ferrimagnetic, but non conductive. Ferrites with low coercivity are denoted as soft ferrites. It means that we need small energy to demagnetize or reverse magnetization. On the other side, we can tune ferrites to have high coercivity. These materials are called hard ferrites and they are used as ferrite permanent magnets.

In general, ferromagnetic properties in materials are given by the spins of unpaired electrons. This is typical for few metal elements as Fe, Co, Ni, Mn or some rare earth elements. These elements and their alloys have high magnetic moment and high saturation magnetization. On the other side, the oxygen atoms reduce ferromagnetic alignment of atomic spins and moreover they localize electrons, resulting in an increase in resistance. This is important in applications employing magnetism at higher frequencies.

In context with this thesis we prepared epitaxial thin films of Ni-ferrites. Ni-ferrites have the formula $NiFe_2O_4$. Ni-ferrites have also inverse spinel structure, where tetrahedral sites are occupied by both Fe^{2+} and Ni^{2+} ions. We will investigate

optical and magneto-optical properties of Ni-ferrite thin films. [10, 12]

2.2 Nanomaterials

Large amount of research is focused on nanomaterials and their new properties which are not common in compare with bulk materials. The goal of this thesis is preparation of thin films. Thin films generally belong to group of nanomaterials. We can at first define nanomaterials and split them to basic groups. The European commission 2011/696/EU admit the definition of nanomaterials. According to the Recommendation a „Nanomaterial“ means: „*A natural, incidental or manufactured material containing particles, in an unbound state or as an aggregate or as an agglomerate and where, for 50 % or more of the particles in the number size distribution, one or more external dimensions is in the size range 1 nm - 100 nm.*“ [13]

In other words, every material that has at least in one direction the size smaller than 100 nm is denoted as nanomaterial.

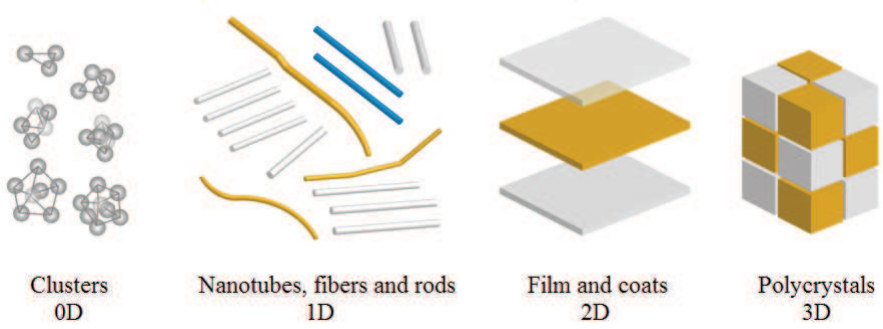

Figure 2.6: *Basic groups of nanostructured materials: 0D nanomaterials (clusters), 1D nanomaterials (nanotubes, fibers, rods), 2D nanomaterials (thin films, nanolayers) and 3D nanomaterials (polycrystals).* [14]

Then, according norm ISO/TS 27687, we can split nanostructured materials to four groups. Nanomaterials are distributed according to dimensions of material. Regarding dimension of material we consider the direction of material in which the size of material is bigger than 100 nm. [13]

Material with size in all three coordinate axes smaller than 100 nm is denoted as 0D („*zero-dimensional*“) material. Nanoparticles or nanodots and also nanocluster materials and nanodispersions are 0D nanostructured materials. The material that has in one coordinate axis the size larger than 100 nm is denoted as 1D („*one-dimensional*“) nanostructured material. To this group belong nanofibers (nanorods)

and nanotubular materials with fibres (rods). [14]

Material with one size of material smaller than 100 nm is 2D („*two-dimensional*“) nanomaterial. As 3D („*three-dimensional*“) nanomaterials we denote powders, fibrous, multilayer and polycrystalline materials in which the 0D, 1D and 2D structural elements are in close contact with each other and form interfaces (Fig. 2.7).

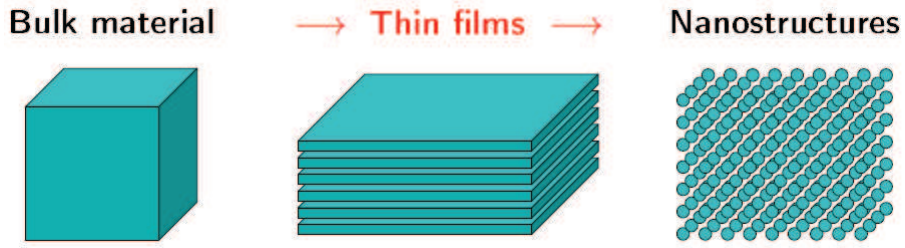

Figure 2.7: *Schematic pictures of the reduction in size of the material in the certain direction or directions and formation of periodic nanostructures. Thin films are the first step to preparation of more nanostructured material, nanostructures.* [15]

Due to the nanoscale size of the material the quantum phenomena appears, providing new properties and functionalities of the material. This is mainly due to a huge increase of the ratio between surface area and volume of the nanomaterial. Large particles have larger number of atoms in the volume than on the surface. In the contrast are nanoparticles. Decrease of size of the particle brings increase of the surface to volume ratio. When we look on thin film, the number of atoms constituting the surface is disproportionately higher than the number of atoms within the thin film. Nanostructured materials can show for example different mechanical, optical, magnetic or electrical properties in the contrast with bulk materials with the same composition.

In this work we will investigate thin layers. In general, thin layer are used for many years for surface treatment of various substrates. Thin films have wide possibilities for applications. We can use them in electrical engineering, mechanical engineering, energy, decorative technique and lot of others. For example, thin layers can be used as infrared mirrors, optical filters, antireflective layers or front electrodes in flat panel displays. Thin films are also use for realization of electronic components and circuits. [16, 17]

2.3 Preparation of nanomaterials

In general nanomaterials can be prepared using two different principals. The first one is process, where we nanomaterial is obtained from bulk material. This approach of nanomaterials preparation is called „top-down“. During this process the compact, bulk material is reduced. This can be achieved for example by abrasion, etching or bombardment of the surface of the material by fast moving ions. Nanoparticles can be obtained for example by the high energy ball milling, e.g. using the planetary ball mill or attritor mill. Fabrication of the thin films using this approach is usually very hard. Disadvantage of this approach is a large consumption of used material. For this reason top-down techniques are rarely used for preparation of thin films.

The second approach is called „bottom-up“. In this approach the nanomaterial is built from single atoms or clusters usually on a substrate. In this area we can find a lot of techniques for preparation of the nanomaterials from individual atoms. Table 1 shows overview of techniques for preparation of the nanomaterials. [18]

Although the second approach bottom-up is more common and used for preparation of nanomaterials, a few techniques using the first top-down approch are used very often. [19]

One of them are lithographic techniques which belong to top-down approach. Lithography is widely used in electronic industry. The lithography is generally the set of methods which are used for accurate chemical-physical treatment of selected parts of the surface.

The principle of lithography starts by deposition of the resist on the substrate. This resist is sensitive on certain type of radiation. If the resist is irradiated by this radiation, causing the chemical reaction in the resist. Then the irradiated or unirradiated places of the resist are removed by solvents. In this context, positive and negative resists are distinguished. If we want to remove irradiated places of the resist, we must use a positive resist (Fig. 2.8). When we want to remove the unirradiated places of the resist, negative resist must be used. The resist is usually irradiated through a mask. The resolution of these methods depends on the type of used radiation and the interaction between radiation and the resist. [20]

Other techniques which belong to top-down approach for preparation nanomaterials are Severe Plastic Deformation methods (SPD) which does not have a large consumption of the used material. The bulk material is exposed to high pressure. The deformed material is subjected to shear or torsion during the SPD. The SPD methods are used for obtaining of the ultrafine grained materials. For example, the Equal Channel Angular Pressing (ECAP) and High Pressure Torsion (HPT) belong to SPD techniques and they are used very often (Fig. 2.9). Other techniques which are written in Table 1 belonging to SPD are Accumulative Roll-Bonding (ARB) and cyclic extrusion compression (CEC). [22]

In the following chapters we will focus on preparation of the thin films. Namely, we discuss about deposition techniques, epitaxy and epitaxial growth of the thin films. Epitaxy is very important if we want to prepare clean and monocrystalline thin films.

Phase	Method	Category	Dimensions	Technique	Approach
Gas	Physical	PVD	2	Evaporation, Sputtering	Top-down
				MBE, PLD	Top-down
	Chemical	CVD	2	TCVD, PACVD, ALD	Top-down
		chemical reactions	0	combustion flame	Bottom-up
				Synthesis in plasma, electric arc	Bottom-up
				Laser, UV, Rtg	Bottom-up
Liquid	Physical	campaign	1	Spinning	Top-down
		chemical reactions		VLS (vapour-liquid-solid)	Top-down
		delf-organization	2	Langmuir-Blodgett (LB)	Bottom-up
	Chemical	chemical reactions	0	Synthesis	Bottom-up
				Sol-gel processes	Bottom-up
Solid	Lithography	with the mask	2,(1,0)	Spinning	Top-down
		without the mask	2,(1,0)	Interference lithography	Top-down
				Focused laser beam (FLBL)	Top-down
				E-beam lithography (EBL), FIB, AFM	Top-down
	Physical	deformation	0	ECAP, HPT, CEC, ARB	Top-down

Table 1: Techniques to prepare nanomaterials. [18]

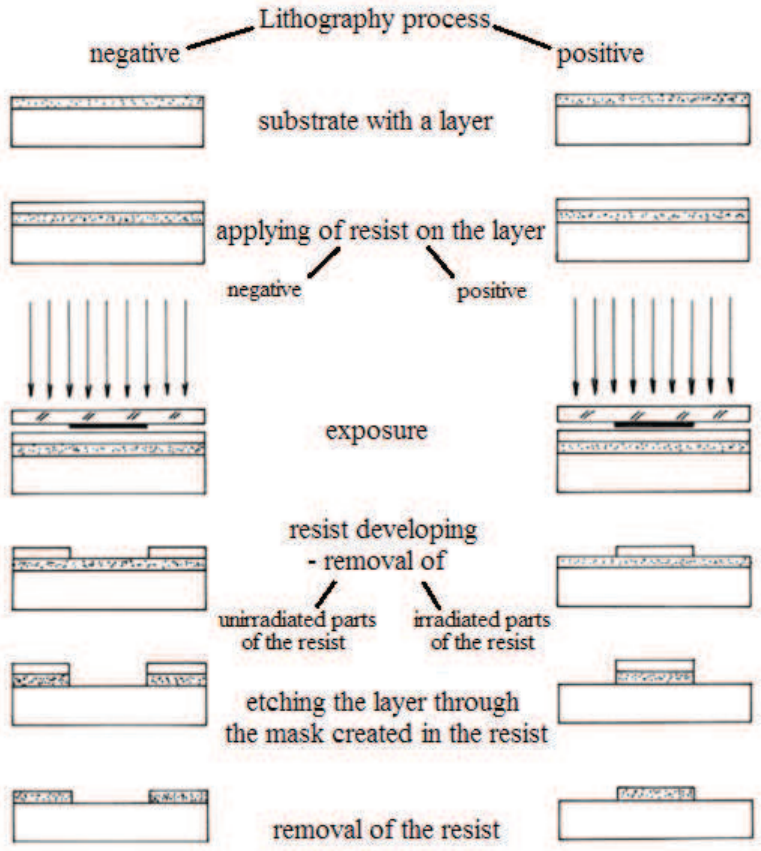

Figure 2.8: *Schematic principle of the Lithography technique. The individual steps for both negative and positive types of lithography are shown in the figure. On the left side the negative resist is applied on the layer. After exposure the unirradiated parts of the resist are removed. On the right side the opposite case with positive resist is shown. After exposure the irradiated places are removed. By these steps the pattern of the mask is transferred to the resist. Subsequently, this pattern is transferred to the layer and rest of the resist on layer is also removed.* [21]

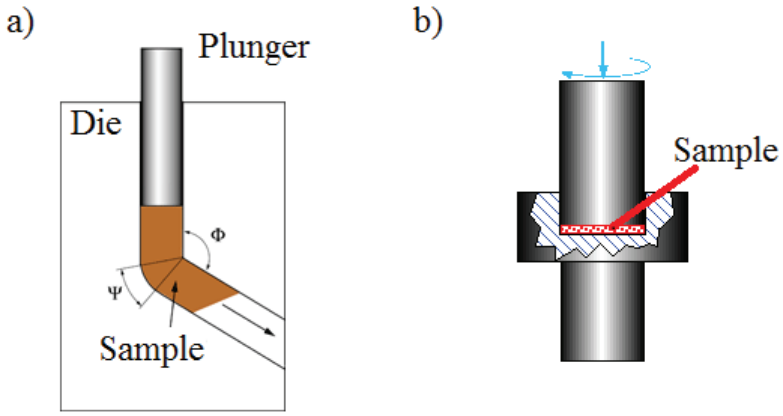

Figure 2.9: *Schematic principles of a) ECAP - Equal Channel Angular Pressing and b) High Pressure Torsion techniques.* [22]

2.4 Preparation of thin films

In following chapters we focus on preparation and principle of growth of thin films. We distinguish two basic deposition techniques. The first one is the physical vapor deposition (PVD) and the second is chemical vapor deposition (CVD). [15]

The physical mechanism of removing of atoms from source and physical mechanismus of the deposition process are observed during PVD (Fig. 2.10). The source is usually solid or molten material. According to way how atoms are removed from the source, two methods of PVD are distinguished. The first method is evaporation, where the atoms are thermally removed from the source. The second method is sputtering and the atoms are dislodged from the surface of source by the impact of gaseous ions.

The chemical vapor deposition (CVD) is based on chemical reactions of atoms during deposition. Accurately, the chemically reacting a volatile compounds react with other gases. The result is forming of a nonvolatile solid that is atomically deposited on substrate. For example, low-pressure CVD (PLCVD), plasma-enhanced CVD (PECVD), thermal CVD (TCVD), plasma assisted CVD (PACVD), laser-enhanced CVD (LECVD) or atomic layer deposition (ALD) are methods which belong to CVD techniques. [15, 23]

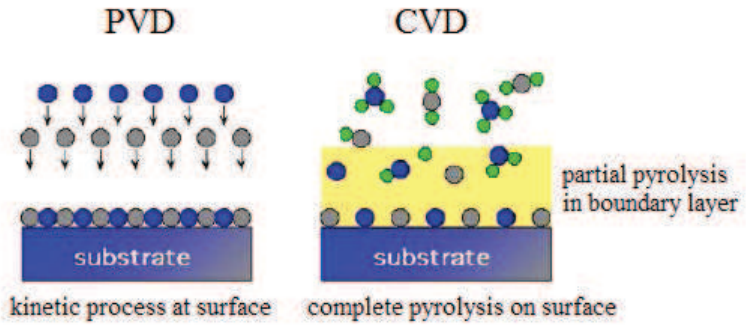

Figure 2.10: *Schematic principles of physical vapor deposition (PVD) and chemical vapor deposition (CVD). At PVD the physical process can occur. At CVD the chemichal reactions to creating a nonvolatile deposited layer are observed.* [15]

2.4.1 Preparation of substrate for deposition techniques

During deposition techniques the layers are deposited onto the substrate or onto the previously deposited layer. Therefore, the procedures for cleaning the substrate

before deposition are very important and neccessary. To obtain very well defined and clear film, we must have suitably prepared substrate.

During deposition processes ultra high vacuum (UHV) must be used. To characterizate of the surface on atomic level is necessary to have stable composition of the surface during deposition process and during characterization of the surface.

It follows, that for atomically clean surface it is necessary to have UHV conditions. First the surface must be cleaned. The process of cleaning of the substrate surface can comprise mechanical polishing, chemical etching, boiling in organic solvents, rinsing in deionized water and a lot of other. Before deposition process there are more common techniques as cleavage, heating, chemical processing and ion sputtering, to clean up sample surface from foreign atoms (Fig. 2.11).

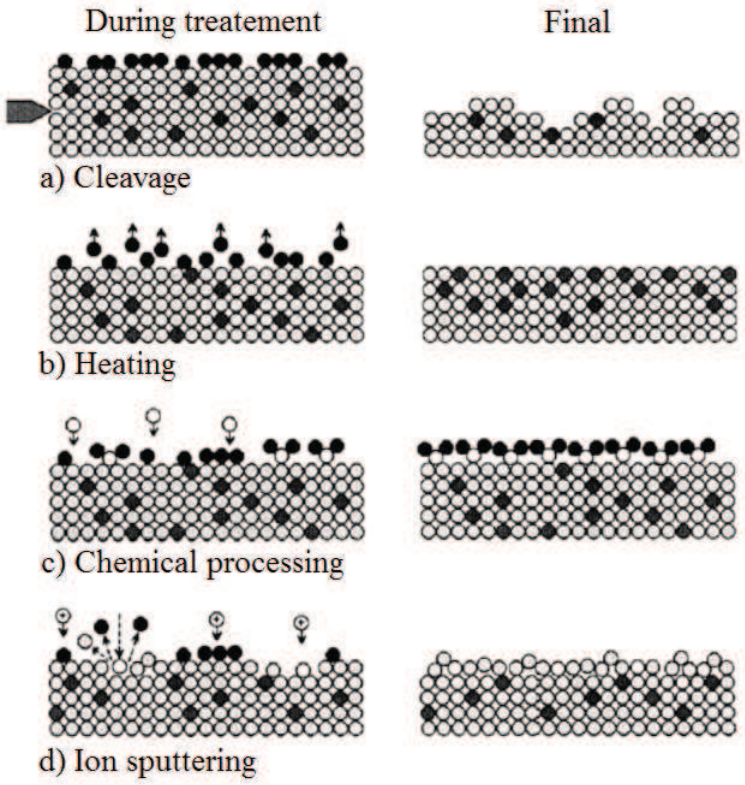

Figure 2.11: *Important techniques for cleaning the surface sample: a) cleavage, b) heating, c) chemical processing and d) ion bombardment. The atoms of the sample are light gray. The black circles denote the surface or bulk contaminants. The reactive gas molecules in c) and impinging ions in d) are illustrated as white circles.* [24]

Cleavage is suitable for fragile materials as oxides, alkali halides, semiconductors as Si and Ge or compound semiconductors, for example GaAs and InP. For this process we have material with notches and by the wedge we cut into the material.

Wedge is controlled mechanically, magnetically or electrically from outside of the chamber. The surface after cleavage is clean, but not flat. For cleavage we must utilize only crystallographic directions of the materials. Cleavage is possible only along certain crystallographinc directions.

For cleaning of the sample surface we can also use heating of the sample in the chamber. Heating can be provided by passing electrical current through the adjacent heater, electron bombardment or laser illumination. Before heating, we must know the melting temperature of the material. The temperature for heating must be lower than melting temperature of the material. [24, 25]

Chemical cleaning of the surface has two steps. The first step, the ex situ chemical treatment, is based on formation of comparatively clean protective layer which can be removed in situ at moderate temperatures. Removing of the protective layer takes place in the vacuum chamber at low pressure. The reactive gas flows to chamber and reacts with impurities on the surface. By this reaction, volatile or not hardly bound compounds are created on the surface, which can be removed from the surface and then from the chamber.

The other possibility to achieve clean surface of the sample is ion sputtering. Accelerated ions, usually noble gas, bomb the surface and sprout atoms from the surface together with impurities. This technique is very effective to clean surface, but surface structure is degraded. Then, annealing is needed to restore surface crystallography and remove embedded and adsorbed atoms of noble gas. [25]

2.5 Theory of the growth of the thin films

The periodic structure of the atoms in volume of the material and mutual force interaction are in steady state with the minimum of energy. The surface can be understood like introducing disorder into the lattice volume. Then, the atoms rearrange to new state with minimum of the energy. This process is called surface reconstruction. The number of atoms on the surface is typically around 10^{15} atoms/cm^2. With the increasing thickness of the layer, the characteristics of the thin films get closer to characteristics of the volumetric materials. [25]

The control of the growth and properties of the thin films is increasing with the improving of the vacuum techniques, surface probes and sensors. Today, level of the

vacuum can reach up to 10^{-10} Pa. The advantage of the ultra high vacuum (UHV) is lower contamination of the surface of prepared thin films. At lower pressure the rate of the growth of thin films can be slowed down, improving quality and providing better control of the growth of thin films. [26]

During the growth of the layer we can observe a few kinds of interaction between atoms from surface of substrate and incident particle (Fig. 2.12). In the first case, elastic scattering occurs, being collisions between the incident particles and the surface. During these collisions the surface is not excited. Other interaction is non elastic scattering. This interaction is collision between the incident particle and particle from the surface, being accompanied by exchange of energy (excitation). The last interaction is a capture of the particle on the surface, followed by its thermal equilibrium with the surface.

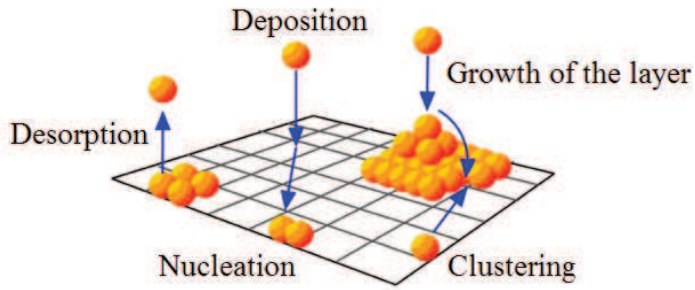

Figure 2.12: *Schematic interaction of particles dynamics on the surface.* [26]

Typical time of the interaction of the incident particle is usually around picoseconds. Distances of particle motion along to the surface are usually in nanometres. If the particle stays longer time on the surface, then we observe other effects, such as attaching of the particle on surface, adsorption, surface diffusion, nucleation and growth of the layers. Further growth manifests itself as coalescence and Ostwald ripening.

When we want to calculate total interaction energy, we have to consider that incident particle interacts with more atoms from the surface, not only with one atom of the sufrace. Total energy is summary from all pairwise interactions between incident particle and atoms from the surface. In this context, we can create graph how energy interaction depends on distance between atoms (Fig. 2.13). Interaction potential is called Lennard-Jones potential. It consists of attractive and repulsive parts. The repulsive part arises due to the overlap of electron orbitals of the incident

particle and electron orbitals of atoms from the surface. The attractive part depends on type of the interaction between particle and surface. According of the interaction type we distinguish few types of bonds and strength of these bonds. Covalent and ionic bond belong to the strong attractive bonds. Van der Waals interaction then belongs between weak bonds. [24, 26]

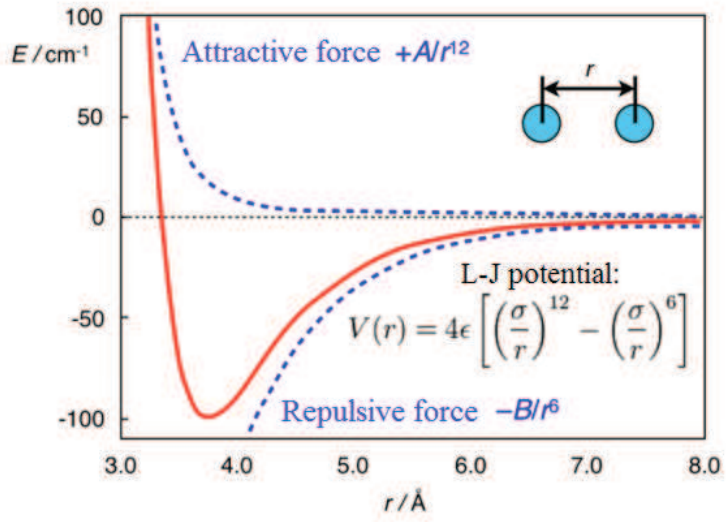

Figure 2.13: *Schematic Lennard-Jones potential between two atoms. Dependence of forces between these two atoms on their mutual distance.* [26]

In other words, this dependence is the sum of two component: the long-range attractive force and the short range repulsive force. Hence, this curve is sometimes called the adsorption potential and corresponds to total potential energy of the condensed atom (Fig. 2.14). In the distance r_m between atom and substrate, the atom has minima of the potential energy V_0. The attractive and repulsive forces are equal at this value of distance between atoms.

2.5.1 Physical adsorption

The atoms captured on the substrate surface correspond to atoms, falling into a potential well of depth V_0 and then they vibrate within it. The energy of bond between atoms for physical adsorption is extremely small. It is usually about a tenth of electron volt. If the atom gets kinetic energy, which is equal to binding energy or higher, the atom will evaporate from the substrate. This energy represents the heat of adsorption of the atom by the substrate.

If the atom stays longer time on the substrate, then atom is physically adsorbed.

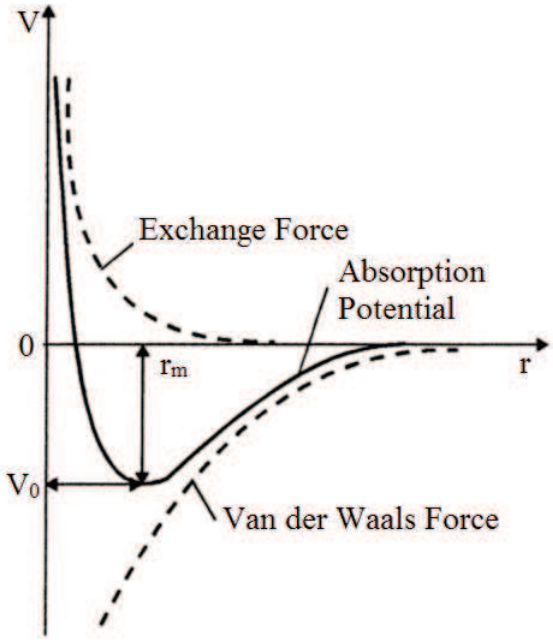

Figure 2.14: *The Potential energy of an atom condensed on to a substrate.* [27]

This process comes almost immediately. During this process there is no exchange of the valence electrons between the atoms from substrate and the absorbed atom. The physical adsorption does not require any activation energy. [27]

After adsorption of the atom on the substrate, there is possibility of migration af the atom to the surface or desorption. However, once the atom is placed in a crystal lattice, it becomes an atom of the surface. Then the atom will be adsorbed on the surface of the substrate, if atom will have sufficient energy. This energy is called also adsorption energy. At low temperatures and energies, most of the incident atoms are adsorbed on the substrate. In case, that energy of atoms is higher than the adsorption energy more than ten times, then more atoms are reflected from the surface.

In this context, we can speak about surface diffusion. Surface diffusion means mass transfer across the surface of the solid. In other words, diffusion is a motion of the particles between individual adsorption sites. It is caused by the thermal energy of the adsorbed atom. This thermal energy increases with the increasing temperature. [24, 26]

The energy of the surface diffusion is usually not constant atwhole surface. It can change locally. Defects and surface steps cause the change of the energy of the surface diffusion. Then diffusion channels and the barriers may be formed. As

diffusion channels can be considered edges or directions of the reconstructed surface. Very important is Ehrlich-Schwoebel barrier (ES barrier) (Fig. 2.15). Barrier is located on the edge of the atomic layer. The atom, which wants to overcome the atomic step and go from the first layer, terrace to the second layer, must expend greater energy than is its diffusion energy. Every terrace, layer increases from the adsorbed atoms on her surface. Large ES barrier leads to motion of the atomic edges, to clustering of the stairs and overall increase in roughness of the surface. By the decrease of the ES barrier, we achieve smooth surface.

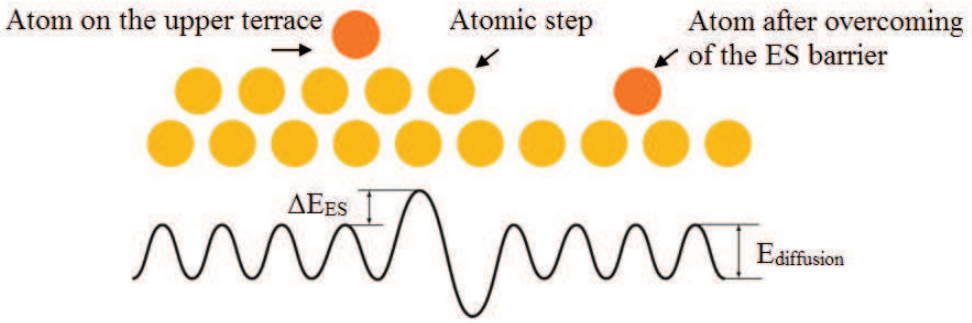

Figure 2.15: *Schematic representation of the ES barrier.* [27]

2.5.2 Chemical adsorption

If chemical affinity between the incident atom and atoms from the surface is observed on the surface, then we cannot speak about physical adsorption. The forces of chemical bonding between the incident atom and atoms from the surface are observed. This interaction is called chemical adsorption or chemisorption. In other words, chemisorption indicates the formation of new chemical bonds between the adsorbate and substrate surface. These chemical forces are characteristic and unique for each substrate and each gas. Chemical adsorption typically occurs at higher temperatures, in the contrast with physical adsorption. Moreover, the chemical adsorption is slower process than physical adsorption. For chemical adsorption the energy of activation is necessary to activate chemical reactions. [28]

The heat for chemical adsorption is higher than for physical adsorption. For physical adsorption the heat is around 20 - 40 kJ/mol. For chemical adsorption the heat of adsorption is about 40 - 400 kJ/mol. In the contrast with physical adsorption, during chemical adsorption surface compound are formed. This process

is irreversible. [29, 30]

2.5.3 Nucleation

Adsorption and desorption are in balance at certain vapor pressure above the substrate. At this saturation vapor pressure, strict adsorption desorption equilibrium is observed. The film can growth on the substrate only in case, when adsorption process is higher than desorption process. This situation occurs at supersaturating of vapor. Namely, the pressure will be higher than the saturation pressure, which is at equilibrium.

Adsorbed atoms can form nuclei. To create stable and energetically favorable nuclei, one condition must be satisfied. This condition is related with the size of nucleus, called critical nucleus. If nucleus has its critical size, critical radius, its state is energetically more efficient than its state at smaller size and the nucleus can growth and attaches other atoms to itself. [25]

In summary, on the surface of the substrate processes, which are shown in the Fig. 2.16 can be observed. The desorption, nucleation, growth of nuclei and step flow can occur simultaneously during preparation of films on the surface substrate. [31]

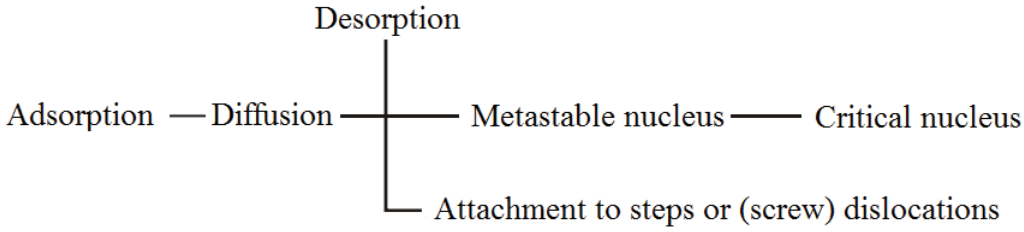

Figure 2.16: *Schema of the possible processes on the surface.* [31]

2.6 Epitaxial growth and growth modes

A lot of studies confirm that exact boundary between the end of nucleation and the onset of nucleus growth does not exist. After exposure of the substrate to the incident vapor, small and highly movable clusters or islands are observed. Then newly established nuclei connect to itself the incident atoms and subcritical clusters. These nuclei growth and the density of islands is increased. Then the islands are joined by the coalescence process. This process decreases the density of islands. The

local denudation of the substrate are observed, where a new nuclei can be created. During deposition the islands are connected to network and they create channels. Subsequently the gaps between channels are filled and resulting film is continuous. This process is usually observed during early stages of deposition and it is typical for first several tens of nanometers. Subsequent growth and formation of the film can occur in three basic growth modes. We distinguish (1) island (Volmer-Weber), (2) layer (Frank-Van der Merwe), and (3) Stranski-Krastanov mode (Fig. 2.17). [24]

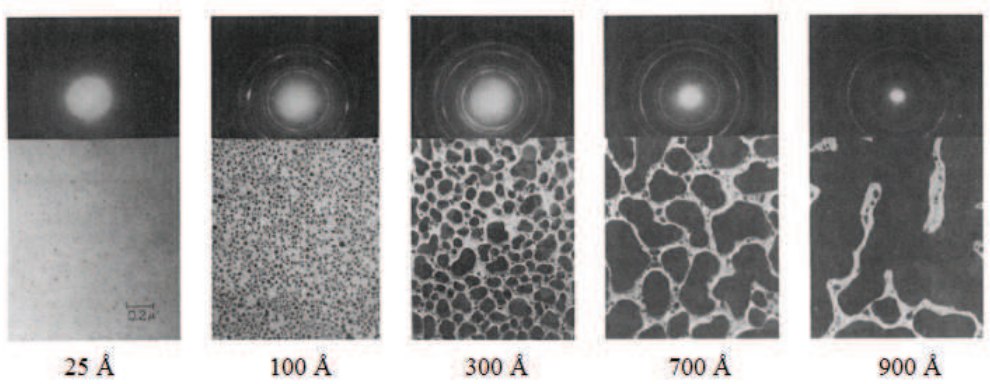

Figure 2.17: *The mechanism of thin film growth. At the first atoms or molecules condense on substrate and create nucleation centers. This process is called nucleation. Then nucleation centers growth and create mobile clusters, islands. The process of merging of islands is denoted coalescence. The merging of islands continue and network with unfilled channels is created. Last step of forming layer is filling of channels.* [15, 24]

The island mode (Volmer-Weber) occurs in case, when atoms or molecules are more strongly bound to each other than to the substrate. The atoms or molecules create on the surface islands. The opposite case is layer by layer growth mode. This mode is called Frank-van der Merwe. In ideal case, new layer growths only in case, that layer below the new layer is continuous, the growth of original layer is completed. At layer growth mode, atoms or molecules are more strongly bound to substrate than to each other. The last growth mode is combination of these two modes. Layers plus islands are observed. At the first, one or more monolayers are created and then islands growth on them. This mode is called Stranski-Krastanov growth mechanism. [15, 32]

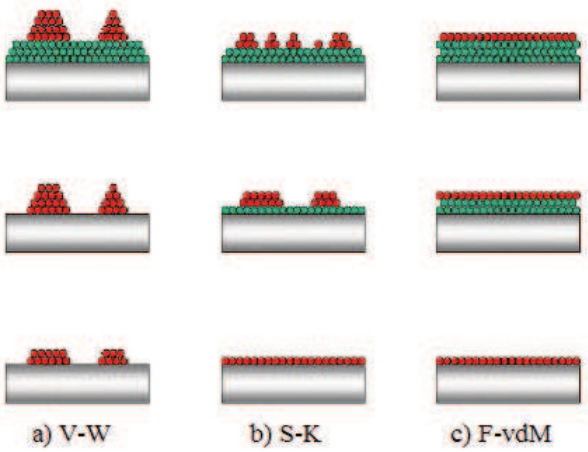

Figure 2.18: *Three basic growth modes. In case a) atoms or molecules have stronger bonds to each other than to substrate. This is called as island (Volmer-Weber) growth mode. The case b) is Stranski-Krastanov growth mode and there is combination of layer and island growth modes. c) Layer (Frank-van der Merwe) growth mode. Atoms are more strongly bonded to substrate than to each other.* [15]

2.7 Epitaxe

The epitaxy is physical process that allows preparation of crystalline thin films. Crystallic thin layer grows on the surface of substrate. The substrate is usually monocrystalline. Crystallic lattice of layer is directly connected to crystallic lattice of substrate. Epitaxial layers can growth from solid, liquid or gaseous substances. These substances are denoted as precursors. Precursors are transported to surface of substrate during deposition process. Surface of substrate have to be atomically smooth and clean. It means, the surface of substrate have to be without any impurities as oxides or adsorbed atoms.

If the epitaxial layer is deposited on substrate with the same composition, the epitaxy is denoted as homoepitaxy. In the opposite case we speak about heteroepitaxy. Deposited layer has different composition than substrate. Lattice parameters of substrate and deposited layer are not same at heteroepitaxy. This difference can cause strain or relax in deposited layer (Fig. 2.19), leading to interfacial defects. [16]

At the first the physical adsorption is observed on a surface. Then on suitable places can occur to chemisorption of individual atoms and to growth of atomic layers and whole structure.

The techniques of epitaxy can be splittted to few groups. Liquid phase epitaxy (LPE), physical vapor deposition (VPD) and molecular beam epitaxy (MBE) be-

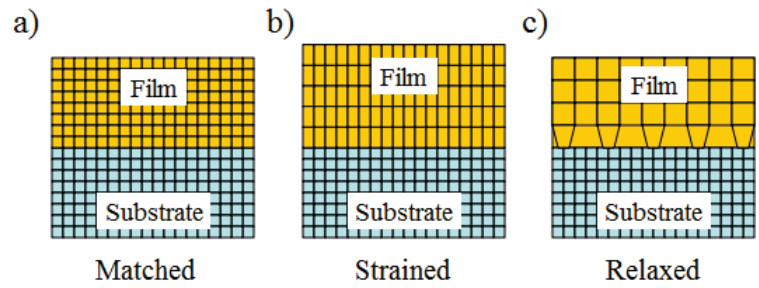

Figure 2.19: *a) Same lattice parameters of the substrate and the film are shown in the picture. This is case of homoepitaxy. Pictures b) and c) illustrate two types of heteroepitaxy with different lattice paramaters: b) strained structure and c) relaxed structure of the film.* [16]

long to epitaxial techniques. [24, 32] We used MBE for preparation of thin films of magnetite and Ni-ferrite. Following chapter is devoted to molecular beam epitaxy.

2.7.1 Molecular Beam Epitaxy

Molecular Beam Epitaxy (MBE) is method designed to growth of high-quality, ultra thin films on substrate. The preparation of thin films proceeds at ultra high vacuum (UHV). The most important parameter of MBE is low rate of deposition. This low rate of deposition enables epitaxial growth of layers. This is cause, why UHV must be used. The amount of impurities in prepared films is associated with time. If film is prepared in short time, it will contain small amount of impurities. However, for MBE and epitaxial growth it is necessary to have low rate of deposition. Films are deposited longer time. Finally, if we want to achieve the same amount of impurities in layer like at „fast preparation“ of the film, higher vacuum (UHV) must be used. [24]

The source materials for MBE are in solid state. Very pure elements are heated at closed Knudsen effusion cells. This material after heating sublimes. If we have prepared substrate for deposition, shutter of effusion cell can be opened. Then atoms flow to substrate. We can also use more efussion cells to preperation thin film of compounds. Material from effusion cell or matarials from more effusion cells condense on substrate (Fig. 2.20). [33]

During preparation it is possible to use some techniques for check of growth of crystallic layer. The Reflection High Energy Electron Diffraction (RHEED) is most common technique using for check of growth during deposition. The MBE

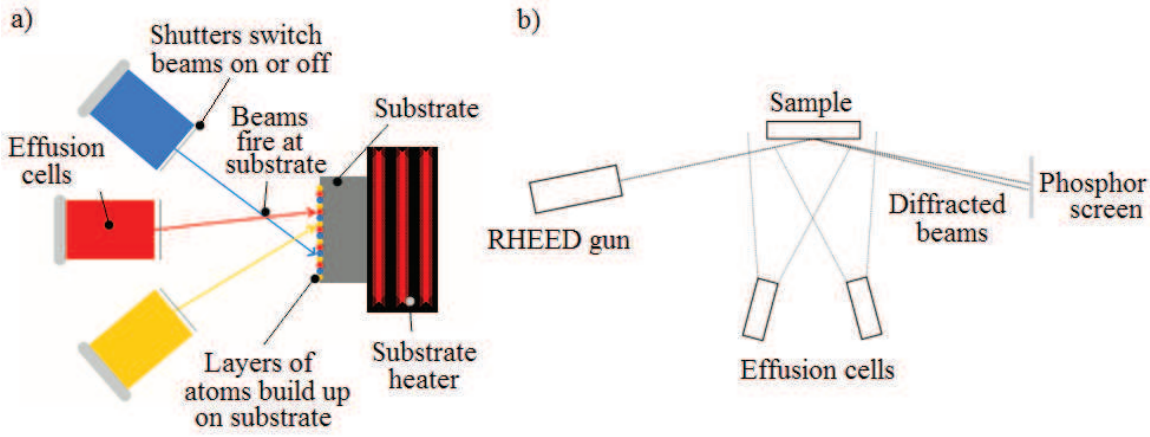

Figure 2.20: *Schematic arrangement of individual parts for MBE equipment. a) The principle of deposition and individual parts of MBE are shown on the picture. b) Simplified diagram of MBE and principle of thin film preparation. The growth of layer is checked by RHEED.* [33, 34]

technique enables to prepare monolayers, multilayers or structures, where electrons are closed at space (quantum dots, quantum wells). The method MBE is usually used for preparation in semiconductor industry for example for semiconductor lasers or light-emitting diodes. [35]

2.8 X-Ray Reflectivity

2.8.1 X-Ray

At the first we will speak about X-ray radiation for better understanding of the techniques like X-ray reflection or X-ray diffraction. X-Ray radiation is electromagnetic waves with very short wavelength. The wavelength is about 10 nm to 1 pm, corresponding energy range is from 120 eV to 120 keV. This wavelength is more than thousand times shorter than wavelength of the visible radiation. With the small wavelength of radiation relates high energy of this radiation. The X-ray beam like electromagnetic wave is defined by the wavelength λ and by frequency ν. The relationship between photon energy and frequency is defined as $E = h\nu = \frac{hc}{\lambda}$, where h is Planck's constant. Frequency increases with increasing energy of radiation. X-ray radiation is used at techniques working with this radiation, due to very small wavelength of X-ray. The wavelength of X-ray is comparable with the distance between atoms in the structure.

The X-ray radiation discovered german physicist Wilhelm Conrad Rotgen at 1895. He discovered this radiation during study of gas discharge. He observed that after impact of radiation on metal anode, the radiation can arise. He performed many attempts to finding and clarification of properties of this radiation. At 1901 he received for his discoveries the first Nobel prize for physic.

Source of the X-ray radiation is usually X-ray tube. This is glass tube with cathode and anode, where vacuum is inside the tube. The vacuum is kept to prevent ionization of the gas and deceleration of the electron beam. The high potential of voltage is maintained between electrodes, providing accelerating of electrons. The voltage range is usually from a few dozens volts to hundreds kilovolts. The electrons are emitted from the cathode. The cathode is formed by a tungsten filament that is heated. The electrons then fly out from this filament and they are directed to one point on the anode. Path of electrons is controlled by the Wehnelt's cylinder. Larger part of the kinetic energy of electrons is converted to heat (98 %) during the impact. The rest of energy (2 %) is converted on energy of the X-ray photons. The X-ray radiation emerges from the X-ray tube through the berrylium windows. The anode must be intensively cooled and intensity of the X-ray radiation depends on the number of electrons which impact on the anode. The intensity is regulated by the change of current, which is used for heating of the filament of cathode. [36]

To increase of radiation intensity, the X-ray tube with a rotating anode can be used. The main requirements on the X-ray tube are the maximum of the intensity radiation, still constant intensity of the radiation, small dimensions and uniform brightness of the outbreak. [36]

Two kinds of radiation can stand out from the anode . The first is bremsstrahlung radiation and the second is characteristic radiation. The bremsstrahlung radiation has continuous spectrum of wavelengths. Fast moving electrons fall on the anode, where they are braked. Their kinetic energy is converted to the energy of the photons of electromagnetic radiation. Spectrum contains radiation of all wavelengths, due to this the spectrum is continuous. The course of spectrum of bremsstrahlung radiation is not linear. This radiation forms background that must be deducted from the measurement of the characteristic radiation. [37]

For characteristic radiation is typical, that the incident electron can knock or-

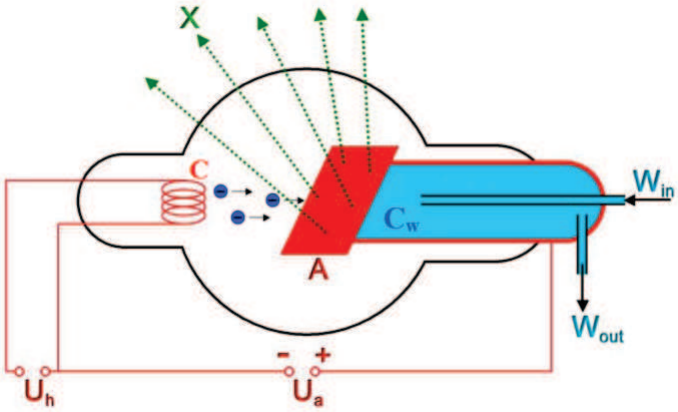

Figure 2.21: *Schematic picture of X-ray tube. X-rays are denoted as X, cathode is C, anode is A, U_h is cathode-heater voltage and U_a is anode voltage. The letter C indicates water cooler, where the water flows through the cooler from input (W_{in}) to ouput (W_{out}).* [37]

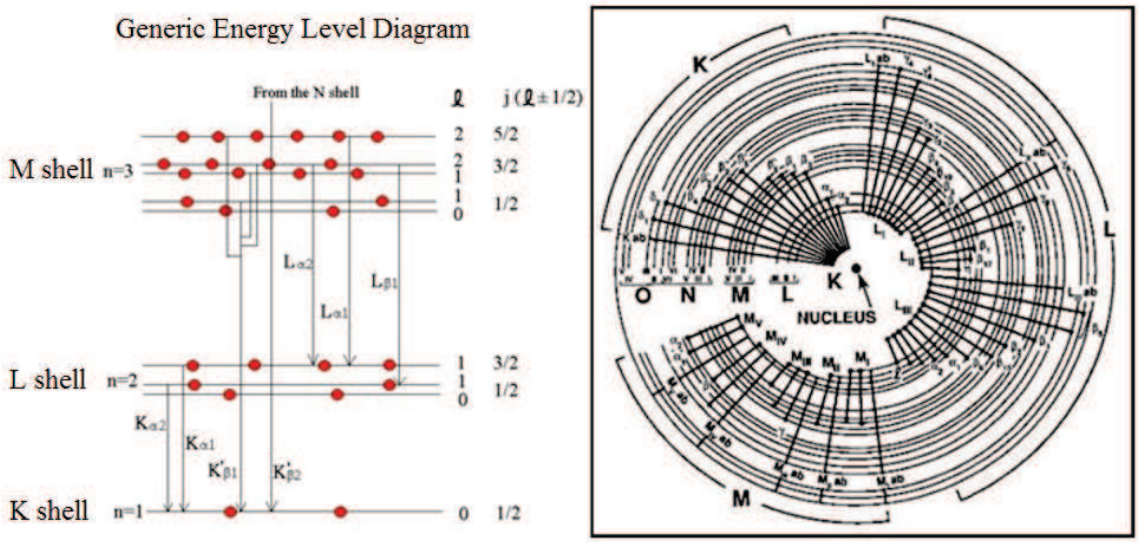

Figure 2.22: *Diagrams of energetic levels of the atom with possible transitions of electrons are illustrated in pictures. To every transition of electron corresponds certain value of the energy. Energetic levels are marked by the alphabets K, L, M, N and O. Transitions of electrons from K and L energetic levels to lower energetic levels are most common.* [36]

bital electron out of inner electron shell of metal atom. The ejected electron is called secondary electron. The vacancy, hole is created on its position. This hole is immediately occupied by another electron from a higher energy levels. This process is is accompanied by emission of radiation with energy that equals to the difference of energy levels. This is characteristic radiation that is typical for every element. Therefore, the characteristic lines appears in the spectrum of radiation . The generated spectral lines depend on material of the target (anode).

Furthermore, Auger electrons can be detected. The release of electron from the inner energy level of the atom is caused by the incident electron. Another electron from higher energy level transits onto its position while the energy is emitted. This emitted energy can be used for ejection else electron from the atom. This electron is then called Auger electron.

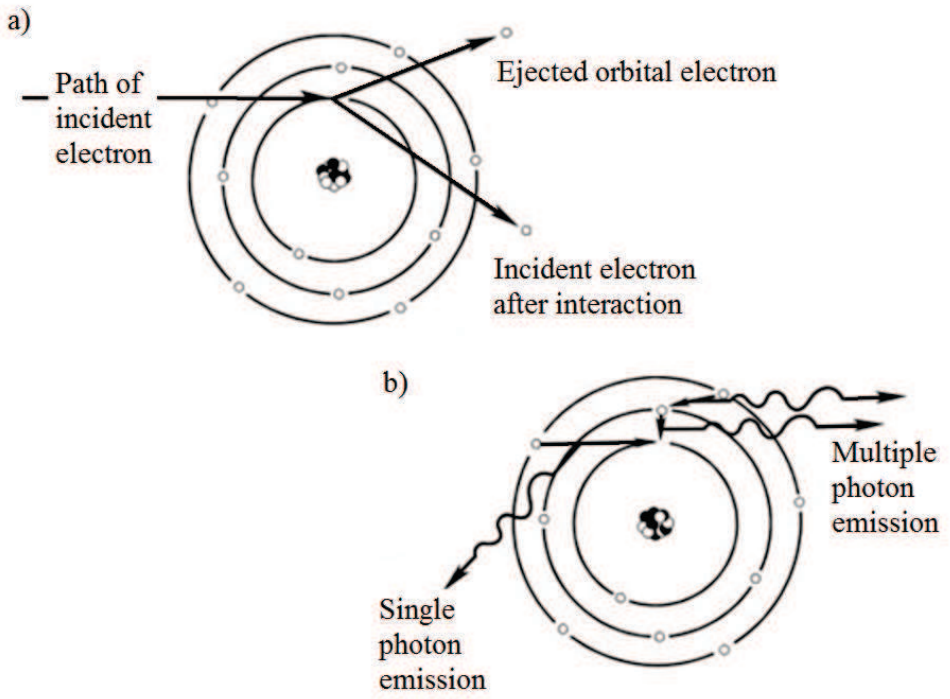

Figure 2.23: *The principle of emission of characteristic X-ray radiation. a) The ejection of orbital electron is shown in the picture. The ejected electron is called secondary electron. b) Emission of characteristic photons. After ejection of electron, the hole is created on its position. Subsequently, the hole is filled by another electron from higher energy level and transition of the electron is accompanied by emission of energy. The value of this energy equals the difference between these two energetic levels. This energy of electron transition is characteristic for every atom. This process repeats. After transition of the electron to the hole, other hole is created on its position which can be filled by another electron.* [36]

2.8.2 X-Ray Reflectivity

We can find a number of techniques which use X-ray radiation. Namely, X-ray Fluorescence Spectroscopy (XRF), radionuclide XRF, X-Ray Diffraction Spectroscopy (XRD), Energy-Dispersive X-ray Spectroscopy (EDS), Wavelength Dispersive X-ray Spectroscopy (WDS) or X-ray Reflection Spectroscopy (XRR) are techniques which are based on utilizing of X-rays. Generally, these techniques belong to X-ray Spectroscopic techniques. In this work we deal with XRR technique that was used for our measurement. [38]

X-ray Reflectivity (XRR) or also X-ray Reflectometry is non-contact and non-destructive technique. This technique is used for determine of thickness of thin films or multilayers, surface density gradients, layer density or surface and interface roughness. The thickness of the film can be determined with very high precision. This technique is used for thickness determination between 2-200 nm with the precesion about 1-3 Å. [39]

X-ray Reflectometry uses the total reflection of X-rays from the sample surface that occurs at very low angles. The principle of the XRR method is detection of intensity of reflected X-ray beam at grazing angles. The monochromatic X-ray with wavelength λ falls on the sample under the angle θ. Intensity of reflected X-rays is detected at the angle 2θ. This reflected beam is recorded by detector. In the picture the specular reflection with condition $\omega = 2\theta/2$ is shown. The mode of operation is therefore $\theta/2\theta$ mode. The critical angle is for a lot of materials less than $0.3\,^\circ$. For determination of density of material is important to know critical angle. At every angle that is below the critical angle the beams are reflected. Above this angle the reflections from the different interfaces interfere with each other. This interference leads to formation of interference fringes. The period of the interference fringes and decrease of the intensity are related to thickness and roughness of layer. The typical range for measurements is between $0\,^\circ$ and $5\,^\circ$ in θ. [36, 41]

2.9 X-Ray Photonelectron spectroscopy

X-ray Photoelectron Spectroscopy (XPS) or we can also say Electron Spectroscopy for Chemical Analysis (ESCA) is used very frequently to characterize of

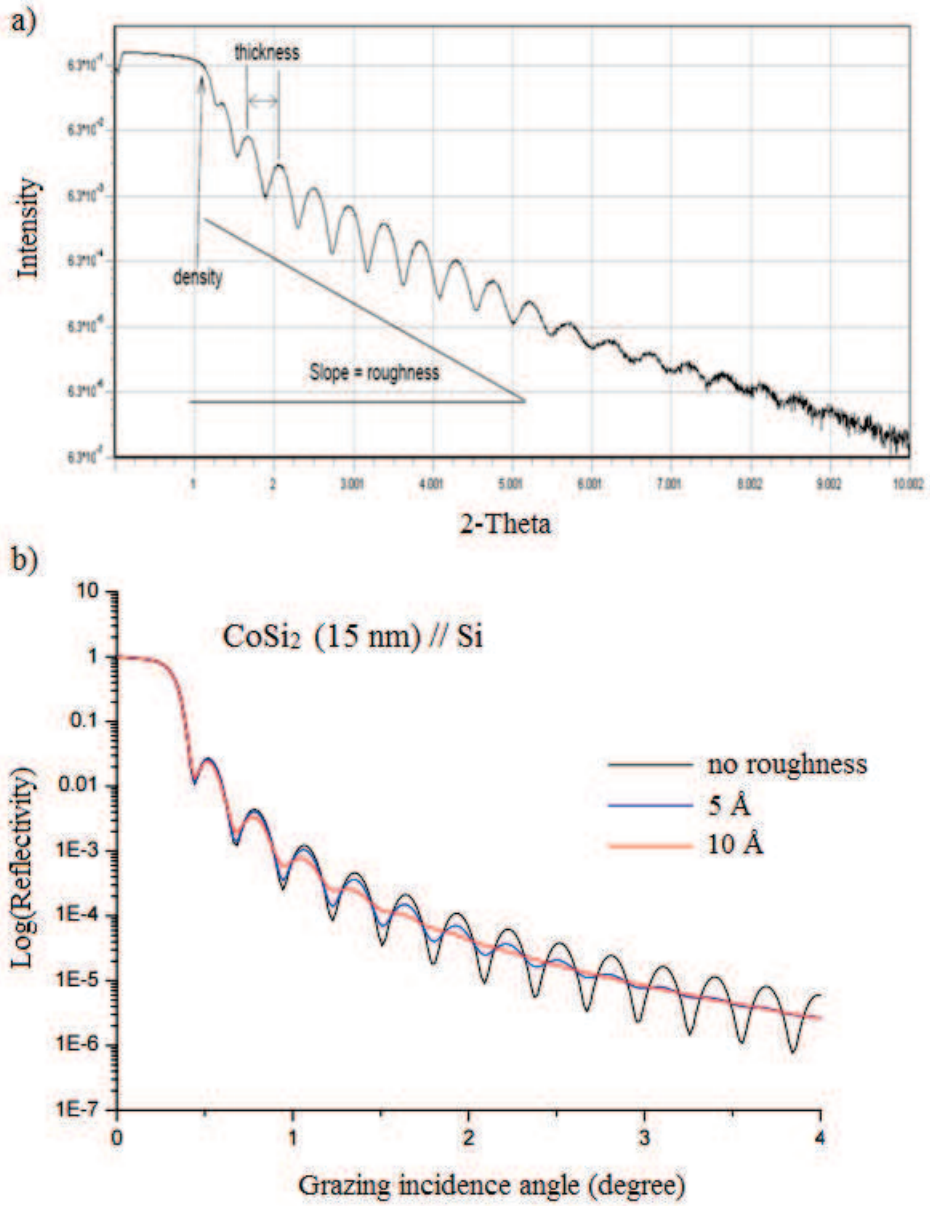

Figure 2.24: *Graphs resulting from the measurement of $CoSi_2$ layer on Si substrate. a) We can see how the thickness, density and roughness of the sample can be determined from this dependence of intensity on angle 2θ. b) Dependence of logarithmic reflectivity on grazing incidence angle. Three different curves correspond to three different surface roughnesses.* [40]

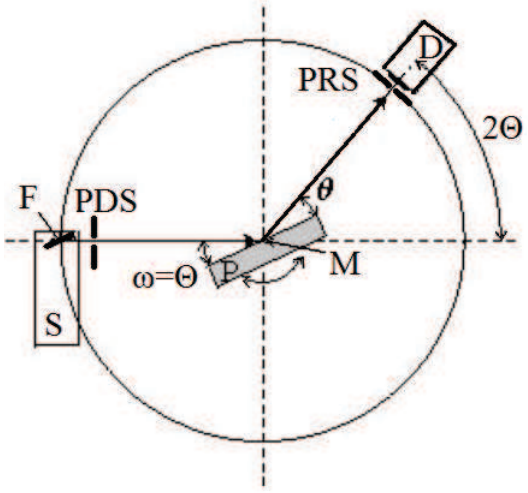

Figure 2.25: *The condition of incident angle $\omega = (2\theta)/2 = \theta$ is fulfilled. The incident angle equals the outgoing angle. The incident angle θ is angle between the beam from source and plane of the sample surface. The detector D rotates at twice speed than sample P. The intensity of reflected beam is detected at the angle 2θ. The sample and detector rotate about the same axis that is at point M. This axis is perpendicular to this picture. The rotation axis lies on the sample surface. The abbreviation PRS means programmable receiving slit and PDS is programmable divergence slit. The beam from source S is focused in the point F to the sample. This focusing point F and detector lie on the same circle.* [42]

thin films and other samples. These names are used for one and same technique. Only one difference in detection is distinguished. The ESCA method detects energy of electrons, whereas the XPS detects wavelength and intensity of X-ray radiation. This detected X-ray radiation is associated with transitions of electrons in atom. This technique is valuable for study of surfaces of materials and very thin layers. The composition of material can be determined. Namely, we can determine all elements which are contained in material and find out informations about bonds between single atoms. This method gives quantitative informations of composition and enables to determine thickness of very thin films. Obtaining of the informations about geometric structure of solid surface is possible. Namely, informations about angles, lengths of bonds or distances between atomic planes can be determined for example by the X-ray Photoelectron Diffraction (XPD) that expands utilize of the XPS method.

During measurement the sample is placed in chamber with UHV. The low-energy monochromatic X-rays irradiate the sample surface. The X-rays excite electrons of atoms from the sample surface. Namely, the incident X-rays knock electrons out

from inner shells of the atom. It occurs when their binding energy is lower than the X-ray energy. The electron is then emitted from atom and electron is called photoelectron. The energy of photoemitted core electron is a function of its binding energy that is characteristic for every element. For XPS the energies of emitted photoelectrons are used as primary data. Further, when core electron is ejected, the hole is created on his position. The outer electron fills this hole and the energy of transition is given by emission of an Auger electron or emission of a characteristic X-ray radiation. Analysis of Auger electrons can be also used in XPS to obtain more informations about sample.

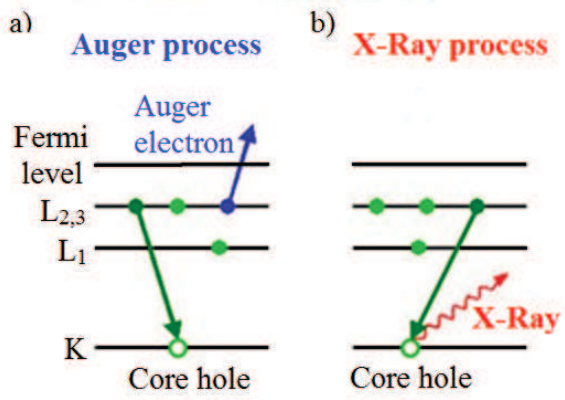

Figure 2.26: *a) Principle of Auger process is illustrated, where the released energy by the transition of electron from higher energy level to lower energy level is used to ejection of Auger electron. b) X-ray process is shown in the picture. After ejecting of core electron, the electron from higher energy level fills the hole. The energy of transition is emitted as X-ray.* [42]

Auger electron was mentioned in the previous chapter. This time, we can expand informations about this type of electrons (Fig. 2.26). The electron from inner energy level of atom can be released. The hole (vacancy) is created on its position. This hole is filled by the electron from the higher energy level and energy of this transition is emitted. This emitted energy can be reused for ejecting of other electron. It happens in case, if the kinetic energy of electron transition is higher than excitation energy of the electron that is neccesary to releasing of the electron. Auger electron is ejected in this case. Energy of Auger electron is not high. This energy equals difference of kinetic energy of the transition and excitation energy of electron. The energy value of Auger electron is usually in range from few hundred to few thousand electronvolts. Production of Auger electrons decreases with increasing atomic number of atom. [42, 43]

The emitted electrons (photoelectrons) and Auger electrons are detected by an electron energy analyzer. Velocity of entering electrons to the detector is important for evaluation their energies. We have to mention that XPS is surface sensitive technique. Only electrons which are near surface can escape with sufficient energy from the surface and then be detected. Nevertheless, these photoelectrons have not high energy because of inelastic collisions within sample. The emitted photoelectrons from the deep of the surface usually more than 20 Å cannot be detected by the detector. These electrons do not have enough of energy for detecting. The spectrum is obtained from detected electrons. Every peak is characteristic for certain element. The knowledge of the area under peak in spectrum is important for obtaining of sample composition. This area corresponds to relative amount of the element in sample. [42]

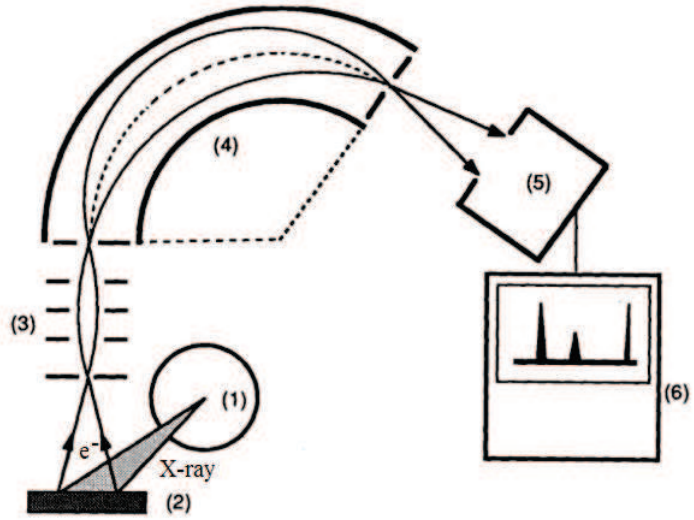

Figure 2.27: *Schematic instrumentation XPS technique. (1) X-ray source, (2) sample, (3) electron optics, (4) electron energy analyzer, (5) detector, (6) electronic controls and output signal.* [44]

Equipment for XPS consists from X-ray source, energy analyzer and detector of photoelectrons. Source of X-ray is usually equipped by two anodes from Mg and Al. If these anodes are irradiated by electrons with energy from 10 to 15 keV, then the lines Kα are intensively emitted with energies 1486.6 eV (Al) and 1253.6 eV (Mg). Energy analyzers work as energy filters with electrostatic field that dismiss electrons only with certain energy. Hemispherical analyzers are largely used. Their resolution is very high and sufficient. All equipment is placed in UHV. For right function of this equipment the pressure lower than 10^{-5} Pa must be used. [43]

2.10 Low-Energy Electron Diffraction

At the first, we can look on idea, why electrons can be used for characterization of the structure of material. When we calculate wavelength of X-ray radiation with energy 5000 eV, we get the wavelength equals 2.5 Å(Equation (1)). This wavelength is very short and comparable with distance of atoms in structure. A lot of techniques as XRD or XRR are based on utilization of X-rays with high energy. The wavelength increases with decreasing energy. In the equation (1) h is Planck's constant and c is the speed of light in vacuum. [45]

$$E = \frac{hc}{\lambda} \tag{1}$$

$$h = 6.626\times10^{-34}\,\text{J.s}$$
$$c = 2.997\times10^{8}\,\text{m/s}$$
$$1\,eV = 1.602\times10^{-19}\,\text{J.s}$$

$$\lambda = \tfrac{hc}{E} = (6.626\times10^{-34}\cdot 2.997\times10^{8})/(5000\cdot 1.602\times10^{-19})$$
$$\lambda = 2.482\times10^{-10}\,\text{m} \doteq 2.5\,\text{Å}$$

Now we can use de Broglie's formula and electrons with energy equals 20 eV. The following de Broglie's formula (Equation (2)) can be used for electron with charge e, where electron is accelerating by the voltage U. In the formula (2) p is momentum, m is weight and v stands speed. For energy 20 eV the corresponding wavelength is 2.7 Å. The wavelength of electron is comparable with the wavelength of X-rays. It follows, that electrons can be used for study of structure. Electrons in energy range from 20 to 200 eV can be diffracted by the atomic lattice.

$$\lambda = \frac{h}{p} = \frac{h}{mv} \tag{2}$$

$$p = mv$$
$$E = eU$$
$$v = \sqrt{\tfrac{2eU}{m_e}}\; m_e = 9.109\times10^{-31}\,\text{kg}$$

$$\lambda = \tfrac{h}{p} = \tfrac{h}{mv} = \tfrac{h}{\sqrt{2eUm_e}}$$
$$\lambda = \tfrac{h}{\sqrt{2Em_e}} = \tfrac{6.626\times10^{-34}}{\sqrt{2}}\cdot 20\cdot 1.602\times10^{-19}\cdot 9.109\times10^{-31} = 2.744\times10^{-10}\,\text{m} \doteq 2.7\,\text{Å}$$

The LEED is based on wave properties of particles. To every particle with weight m and speed v therefore corresponds wavelength λ. When the wavelength is comparable with distances between atoms, then after impact of electron beam on the surface, diffraction pattern is created. This pattern gives to us information about surface structure. Diffraction of electrons occurs at process elastic scattering of electrons. Only elastic scattered electrons fulfill condition of diffraction. Electrons does not lost their energy after collision. These electrons are scattered, but not isotropically. Namely, they are not scattered equally to every directions. Some directions are more prefered. Structure of material determines which of directions is prioritized. By this manner, we get informations about structure of surface. These informations are contained in diffraction pattern that is shown in reciprocal space. [45]

The LEED uses electrons with low energy in range from 20 to 500 eV. We distinguish a few modifications of this method. We can register whole diffraction pattern, measure angle dependencies by movement of detector, tilt sample during measurement or change energy of electrons. The measurement takes place in chamber with UHV. The equipments of LEED contains mainly electron gun, goniometer and detector of electrons. From the results of measurement, informations about symmetry of elementary cell, about structure and its disorders can be obtained. Specifying of disorders requires high measurement accuracy. [46]

2.11 Atomic Force Microscopy

Atomic Force Microscopy is based on forces which act between atoms. One advantage of this techniques is fact, that we do not need a conductive sample.

Two types of microscopes according to their setup are distinguished. According of type of microscope, the sample or the gauging probe is shifted during measurement. The gauging probe is shoulder with a tip that is attached to the base.

For our measurement was used microscope, where the sample is shifted during measurement. The movement is realized with help of piezocrystal (piezoelectric material). When the piezocrystal is exposed to change of the voltage, it causes change of crystal size.

Before scanning of surface the reflected beam from the upper part of shoulder

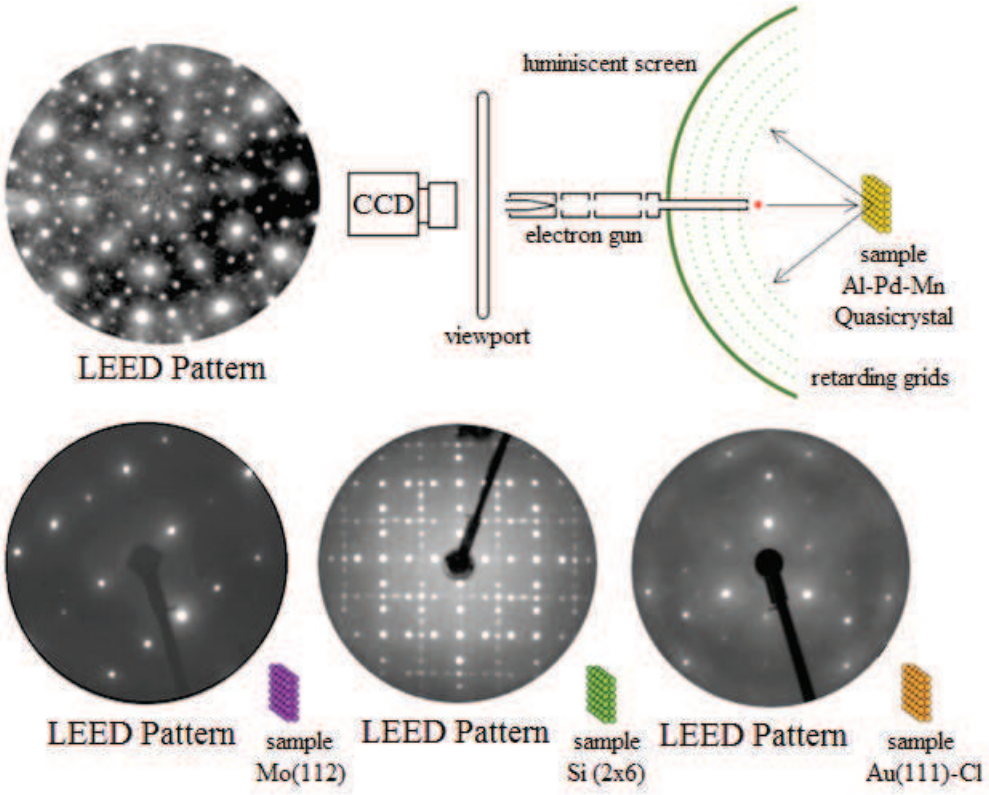

Figure 2.28: *The schematic principle and individual parts of LEED equipment are illustrated in the picture. Furthermore, the LEED patterns of Al-Pd-Mn quasicrystal, Mo(112), Si(2x6) and Au(111)-Cl samples are shown predominantly in the lower part of the figure.* [46]

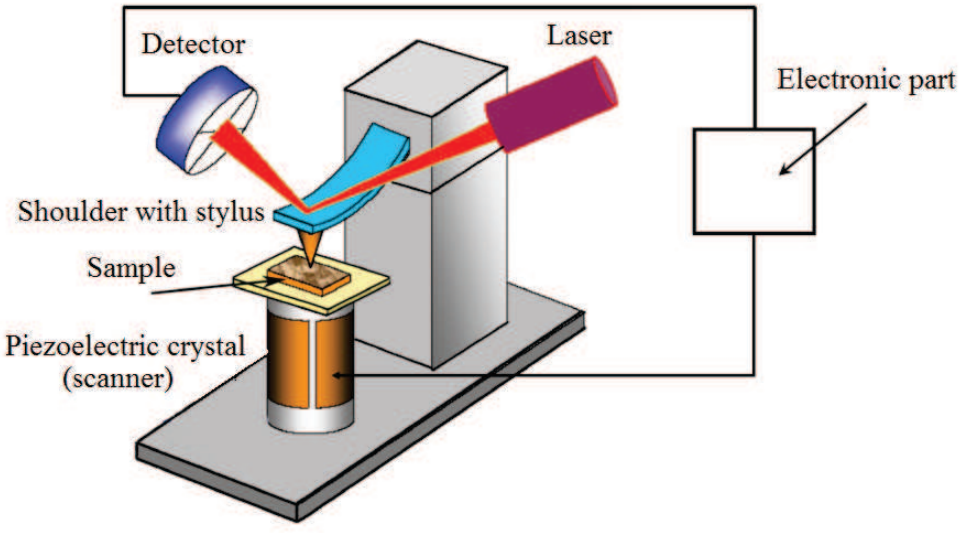

Figure 2.29: *The construction and basic parts of microscope with piezocrystal that is placed below sample are shown in the picture. The movement of sample is realized with piezocrystal. The changing forces cause bending of shoulder during measurement. This bending of shoulder causes laser displacement from the center of detector. The laser displacements are detected as changes of voltage in detector. These changes of voltage are evaluated.* [47]

must hit the middle of detector. Then the shoulder with tip lands on sample and the shoulder is bent due to force action that is between the tip and sample. This flexion is detected by laser that is deflected out of the middle of detector. During movement of the tip over sample surface the different forces act between atoms of tip and sample. These different forces take effect in degree of incurvation of shoulder. The incurvation is then evaluated and shown in final picture. Then, informations about sample surface are obtained.

According to the choice of mode of measurement, the underlying principle of measurement is a little different. In contact mode, we distinguish measurement with constant height or constant force. At mode keeping constant height, the base is kept still in same height and incurvation of shoulder is monitored. In contrast, at the mode keeping still constant force, constant incurvation of shoulder is maintained. To keeping of same incurvation during scanning of surface the sample is shifted. Namely, the height of the sample is changing during measurement. To maintaining of still same force between tip and sample, negative feedback must be used.

At noncontact and semicontact mode the shoulder vibrates with certain amplitude. At this mode the negative feedback must be used. [47]

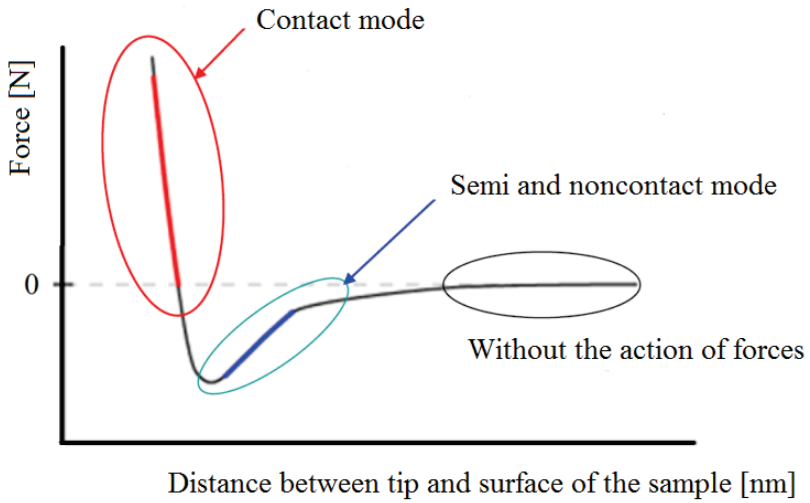

Figure 2.30: *Force actuation between two atoms in dependence on their distance. The repulsive forces are observed in contact mode. The attractive forces are observed in noncontact. In semicontact mode a both repulsive and attractive forces act during measurement. [46]*

In summary we can work with three basic modes of AFM. These are contact, noncontact or semicontact mode.

In general, contact mode uses mutual repulsive forces between atoms. In this mode, tip is in direct contact with sample. We can measure with constant height of base or with constant distance between tip and surface of the sample. The tip is pushed to sample and it leads to the bending of shoulder. The bending of shoulder is detected by laser and this can be used for evaluating the surface of the sample. The distance between the tip and the sample surface is smaller than few tenths of a nanometers. In this mode the tip can be damaged or contaminated during measurement. To prevent a damage of the tip or to minimalize damage, the shoulder with small constant of stiffness must be used.

Semicontact mode works on the same principle as noncontact mode. The shoulder oscillates at resonant frequency with certain amplitude. After approaching of the probe on the sample surface, the amplitude of shoulder decreases to a previously set value. Usually, it is half of the amplitude that is at resonant frequency. [46, 48] During scanning the surface the amplitude is kept at the still same value. For this purpose is used feedback. The control of the amplitude is possible due to movement of the piezocrystal below sample. The changes in the amplitude of vibrating shoulder are detected during approximation and procrastination between surface and tip.

The accuracy of the measurement depends on the parameters of the feedback and during all measurement the corresponding error signal can be monitored. On perfectly smooth surfaces the error signal would be zero. In semicontact mode attractive and repulsive interactions act between atoms.

Noncontact mode uses attractive forces between atoms. The shoulder with tip for noncontact and semicontact mode must be more stiff (higher constant of stiffness) than for contact mode. This is to prevent of interception of the shoulder with tip on the sample surface. [49]

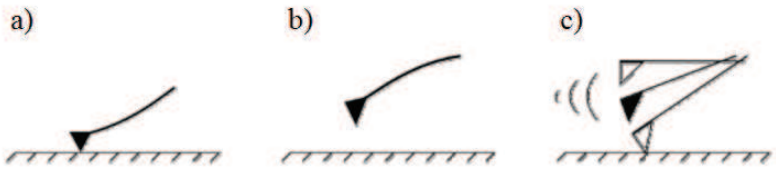

Figure 2.31: *a) Contact mode - action of repulsive forces, b) noncontact mode - action of attractive forces, c) semicontact mode - alternating action of repulsive and attractive forces.* [46]

2.12 Vibration Sample Magnetrometry

The method Vibrating Sample Magnetometer (VSM) is based on Faraday's Law of Induction. The law says that changing magnetic field produces an electric field. If we have oscillating magnetic sample in magnetic filed, then the alternating voltage is generated in coil. This voltage is measured. The values of voltages provide information about the changing magnetic field. This voltage is directly associated with magnetic moment of the sample. By this technique we can obtain hysteresis loops of materials. We can measure magnetization of samples, coercive field and lot of others. Generally, we can say that magnetic properties of magnetic materials can be measured by the VSM technique. Magnetic properties of materials can be measured as a function of temperature, intensity of external magnetic field and time. [50, 51]

Before we will speak about the principle of measurement, we can mention shortly distribution of magnetic materials and their characteristics. Magnetic materials and mainly their behavior in magnetic filed is closely related with their intrinsic angular momentum or spin of its electrons. According to their reactions on the applied external field we can split magnetic materials on diamagnetic, paramagnetic, ferromagnetic or antiferromagnetic materials. Diamagnetic materials weaken the external magnetic field. [52] They have a negative susceptibility, so $\chi < 0$. The relative permeability of these materials is lower than one ($\mu_r < 1$). The susceptibility of diamagnetic materials is not function of temperature T and intensity of magnetic field H. These materials have fully filled their electron peels by electrons. For example, rare gases, copper (Cu), silver (Ag), gold (Au), water and some others are diamagnetic materials. Paramagnetic materials weakly amplify the external magnetic field. They have a positive susceptibility, so $\chi > 0$ and their permeability is higher than one ($\mu_r < 1$). Their susceptibility is not function of intensity of external magnetic field H. Materials as oxygen O_2, alcali metals or air are paramagnetic.

Ferromagnetic materials are interesting group. These materials have susceptibility much more higher than zero ($\chi >> 0$). Their relatively permeability is higher than one ($\mu_r >> 1$). The susceptibility is function of temperature T, intensity of magnetic field H and history of the sample. Susceptibility of ferromagnetic materials is larger than susceptibility of paramagnetic materials. Ferromagnetic materials

multifold amplify the external magnetic field. They have non-zero magnetic moment at zero magnetic field. [53]

In ferromagnetic materials we can observe some areas where the single magnetic moments are rotated in one and same direction. These areas are called as magnetic domains. After inserting ferromagnetic material to an external magnetic field, the magnetic domains of the material are rotated to same direction as applied magnetic field. By this process we can create the dependence of the magnetization of the sample on external magnetic field. This dependence is called as hysteresis loop. The dependencies of the magnetization of paramagnetic and diamagnetic materials on external magnetic field are linear. [54]

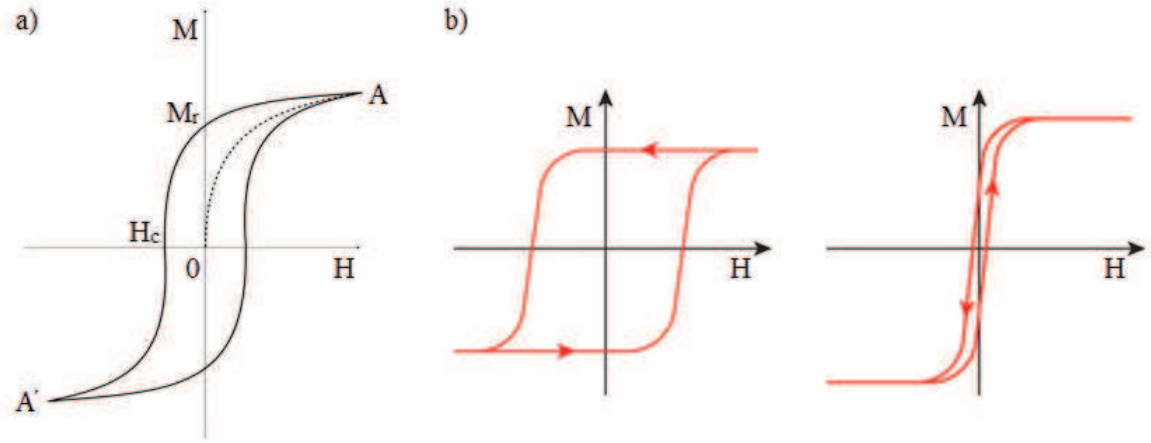

Figure 2.32: *a) Hysteresis loop of ferromagnetic material. It is dependence od magnetization of the sample on intensity of external magnetic field. Points A and A' are centrally symmetric. Dotted curve is curve of primary magnetization. Remanent magnetization is marked as M_r and coercive magnetic field is marked as H_c. b) On the left side is shown the hysteresis loop of magnetic hard material. On the right side is shown the hysteresis loop of magnetic soft material.* [53]

The hysteresis loops provide some properties of magnetic materials. The value of remanent magnetization M_r gives information about value of the magnetization of the sample at zero external magnetic field. The value of the coercive magnetic field H_c is also important. On the basis of the value of coercive magnetic field H_c we can divide magnetic materials on magnetic hard and magnetic soft materials. The magnetic soft materials have narrow hysteresis loop. The value of coercive magnetic field is usually about $H_c \approx 10^2$. These materials are used as transformers. The magnetic hard materials have wide hysteresis loop and higher value of coercive

magnetic field. The value of coercive magnetic field of these materials is about $H_c \approx 10^4$. Demagnetization of hard magnetic materials is harder than demagnetization of soft magnetic materials. Permanent magnets are made from magnetic hard materials. Demagnetization can occurs by the application of high temperature or alternating field. Temperature suitable for demagnetization have to be higher than Curie's temperature T_C. After application the temperature which is higher than Curie's temperature, the arrangement of magnetic moments will be random. The opposite case can be state of material at temperature 0 K. Directions of all magnetic moments at 0 K are same. The magnetization M_0 of the sample is the largest at 0K. This process can be observed on dependence of spontaneous magnetization of sample on temperature (Fig. 2.33).

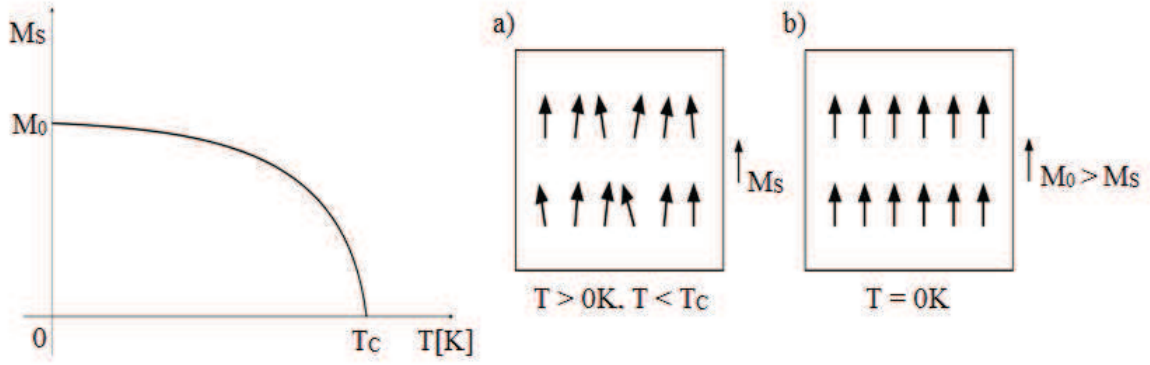

Figure 2.33: *On the left side the dependence of the spontaneous magnetization M_S on temperature T is shown. The magnetization M_0 at temperature 0 K is the largest. Magnetization is the smallest at Curie's temperature T_C. On the right side, a) magnetic moments are shown at temperature higher than 0K and lower than T_C, b) magnetic moments at 0 K.* [54]

We can go back to VSM and start speak about the principle of measurement. At the first, sample is placed to constant and homogenous magnetic field. Magnetic sample is magnetized by the magnetic field. It means that magnetic field will act on magnetic domains in the sample or directly on magnetic spins. The inserted sample to magnetic sample vibrates with small amplitude. The magnetic moment of the sample creates own magnetic stray field around sample. When the sample vibrates the magnetic stray field is changing. These changes are detected by the pick-up coils, because the voltage is induced to these coils. According with this, the induction current is then amplified and electronically processed.

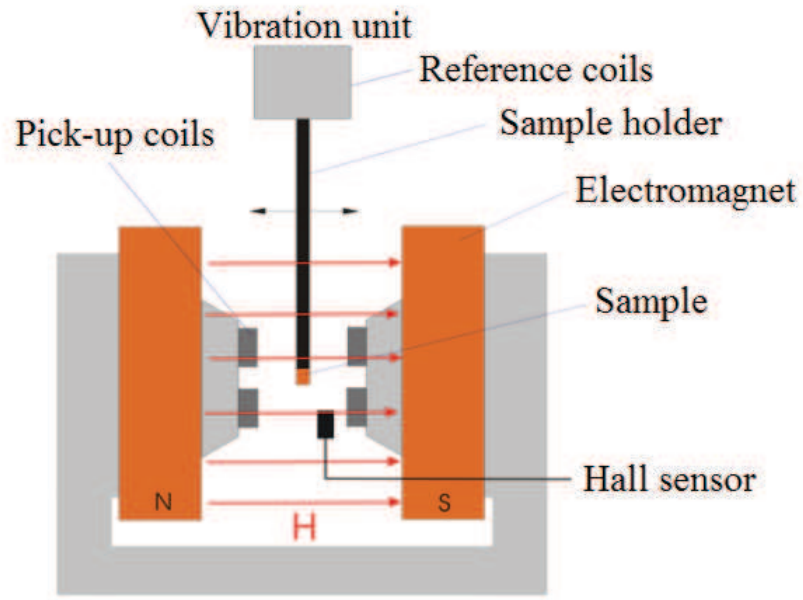

Figure 2.34: *The individual parts of VSM device are electromagnet that is cooled by water, power supply, coils for reference measurement and pick-up coils, Hall probe. For detecting and processing of signal there are components as amplifier, lock in amplifier for elimination of noise, meter and computer interface.* [55]

2.13 Ellipsometric Spectroscopy

Ellipsometry is an optical measuring technique which evaluate the reflected beam of the light from the sample surface. The core of this technique is the measurement of the change of polarization of the light after reflection from the sample. The name of this technique is derived from the fact that polarized light is generally elliptic after reflection. Ellipsometry measurements are mostly expressed with help of the angles ψ and Δ. Angle ψ represents the ratio of the amplitudes of reflected s- and p-polarized light and Δ is the phase difference between s- and p- polarized waves. In spectroscopic ellipsometry these values are measured in dependence on wavelength. [56]

The measurement performed in the enlarged visible range of radiation which from near infrared to near ultraviolet area of radiation.

The utilization of spectroscopic ellipsometry is wide. Using this technique we can characterize the growth of thin films, etching or thermal oxidation. Spectroscopic ellipsometry enables to characterize not only thin films, but large amount of others samples and materials. It enables us to determine their optical constants like their refractive index or determine sample thickness. However, this method has

also limitations. One of them is the roughness of the investigated surface. The second limitation is based on the fact that we must measure under oblique angles. When light is reflected from an unequal surface reflected light will be scattered. We then detect light with lower intensity than light before reflection. If the value of inhomogeneity of the surface higher than 30 % in comparison with the value of used wavelength the measurement error grows rapidly.

The angle of incidence is chosen so that the sensitivity of measuring is greatest. For semiconductors the typical angle of incidence lies between 70 ° to 80 °. At normal incidence is not possible to perform ellipsometric measurements, because then we cannot distinguish s- and p- polarization. The only exception of this is the characterization of planar optical anisotropy. In this case the ellipsometric measurement is often performed at normal incidence with rotating sample. [57, 58]

One of the striking features of ellipsometry is high precision of measurement and sensitivity to thickness of layers which can be up around values 10 nm. Moreover, measuring is relatively easy, fast and it belongs to the nondestructive methods. The principle of the ellipsometric measurement comprises the observation of changes in polarization of the light after incidence on the surface sample. Measuring usually take place under multiple angles of incidence in the range from 0 ° to 90 °. In reflected light we can observe changes between the *s*- and *p*- polarizated wave. The difference between the *s*- and *p*- polarized wave creates an ellipse, thus the resulting light is elliptical. In the figure 2.35 the basic components of ellipsometer are shown.

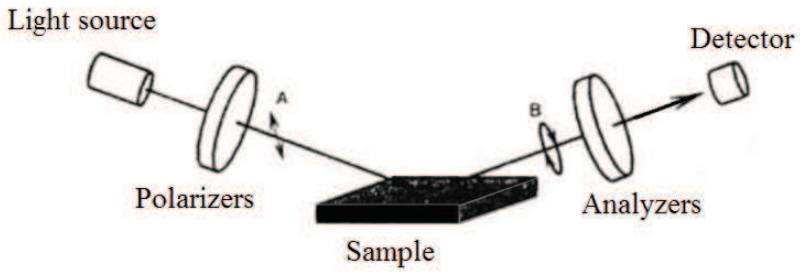

Figure 2.35: *Schematic arrangement of ellipsometer.* [56]

2.14 Magneto-optical Spectroscopy

One of the most important optical methods to studying ferromagnetic and ferrimagnetic materials is a technique which is based on magneto-optical Kerr effect (MOKE). This method works using the reflection of linearly polarized light from the sample surface. During the measurement the sample is embedded to a magnetic field. The change of polarization occurs during the reflection. The initial linear polarized light becomes elliptical. Furthermore, the intensity of the reflected beam is reduces and major semi axis is rotated in compare with the original direction. The angle of rotation is angle of the Kerr rotation. The Kerr rotation angle, as well as ellipticity, is dependent on size and orientation of magnetization vector of material.

First time this phenomenon was observed by Michael Faraday. The action of magnetic field on glass sample rotated the plane of polarization of the passing radiation. He examined also reflected light from the surface of metallic materials which were embedded in the magnetic field. But he did not manage to describe this effect, because of large surface inequalities. [59, 60]

A few decades years later in 1875, John Kerr observed and described this effect. It means the rotation of plane of polarized light during reflection from the surface of polished rods.

We distinguished three geometric arrangement of this method in dependence on direction of the sample magnetization. It can be polar, transverse or longitudinal arrangement. They are distinguished according to the fact, how the direction of the sample magnetization is orientated towards incidence plane of the radiation and towards surface plane of the sample.

At polar arrangement the vector of the sample magnetization is perpendicular to plane of the sample. The transverse effect occurs, when the vector of the magnetization is parallel with the plane of the sample and also the vector of the magnetization is perpendicular to the plane of the incidence. The last longitudinal effect can observed, if the vector of the magnetization is parallel with the plane of the sample and at the same time is parallel to the incidence plane. All these arrangement are shown in the Fig. 2.36.

The principle of this method is shown in the Fig. 2.38. Linearly polarized light falls on the sample, i.e., *s*-polarized light falls on the sample and after the reflection

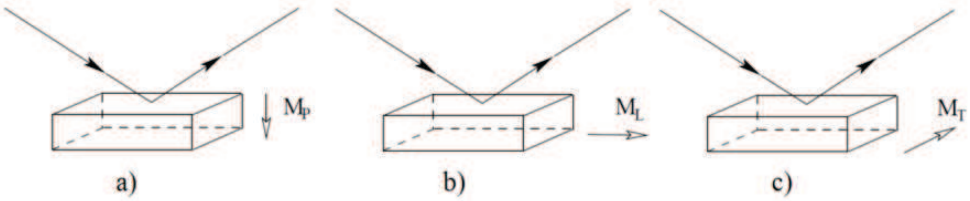

Figure 2.36: *a) Polar, b) longitudinal, c) transverse arrangement.* [59]

besides s-polarized light also p-polarized light appears.

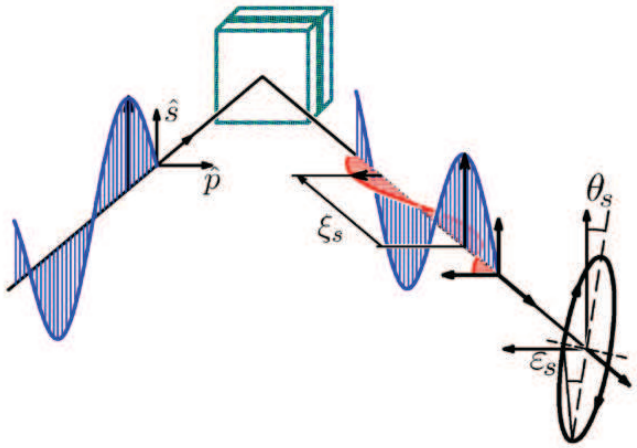

Figure 2.37: *Schematic principle of the method.* [60]

This effect is caused by the reflection of light from optically anisotropic material. After insertion of the isotropic sample to a magnetic field the sample starts to be optically anisotropic. Due to this, the Kerr rotation can be observed. Kerr rotation angle is designated as θ_s. Ellipticity is identified as ε_s (Fig. 2.38). A both of these values are measured in dependent on energy.

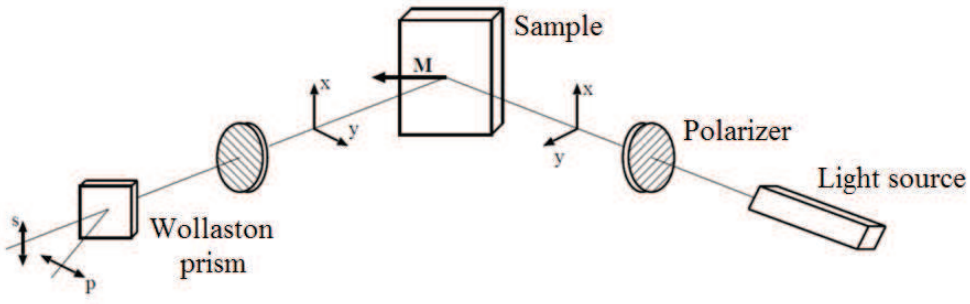

Figure 2.38: *Schematic arrangement of the method MOKE.* [61]

3 Experimental part

3.1 Equipment for preparation and characterization

The epitaxial thin layers of magnetite Fe_3O_4 and nickel-ferrite $NiFe_2O_4$ on MgO(001) substrate were prepared. Namely, the thin layers were prepared at University in Osnabrück in working group that is led by Prof. Dr. Joachim Wollschläger. At this laboratory in Osnabrück, reactive MBE was used for preparation of samples and subsequently the samples were characterized by XPS and LEED. Magnetic properties of the samples were measured there by VSM. The equipments for preparation of thin films and their characterization is shown in the figure 3.1.

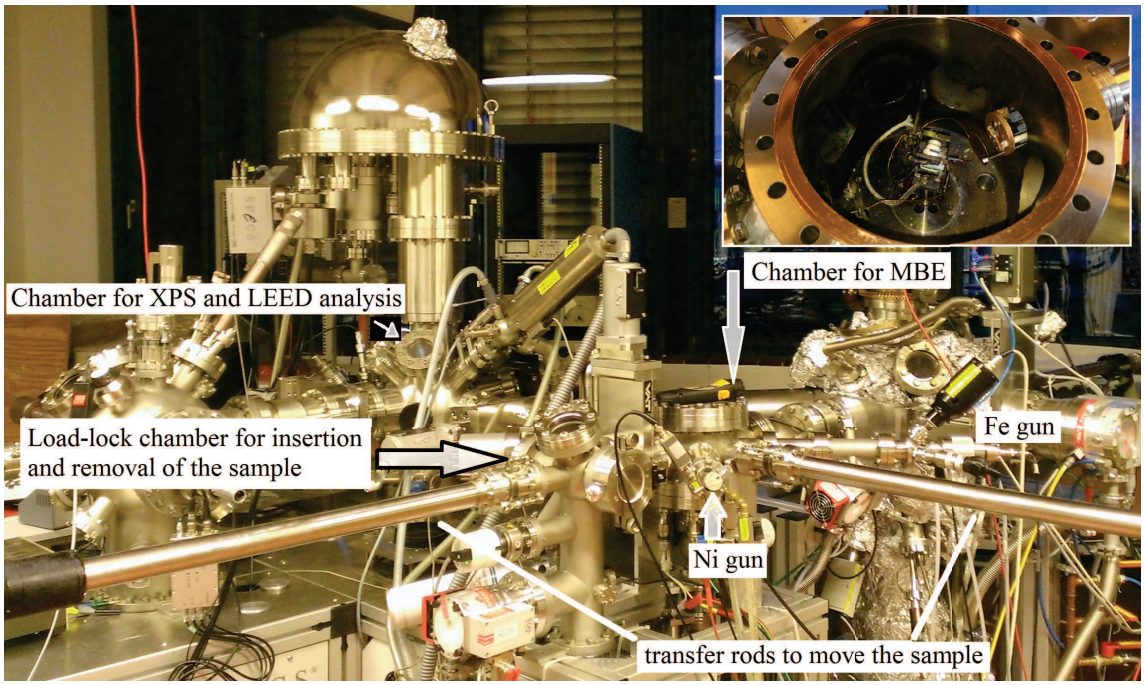

Figure 3.1: *Equipments for MBE, XPS and LEED.*

Before every deposition process the UHV must be in the chamber to avoid contamination of sample by particles of materials. Then substrate must be placed to holder (Fig. 3.3). Prepared holder with substrate can be inserted to load-lock chamber that is closed from the deposition chamber to keeping UHV in the deposition chamber. After creating vacuum in load-lock chamber, the holder can be moved to deposition chamber, where is placed to holder (Fig. 3.2).

The loop, coil is placed around this holder, that is used for heating up of substrate placed in the holder. Thermostat is placed near substrate to check the sub-

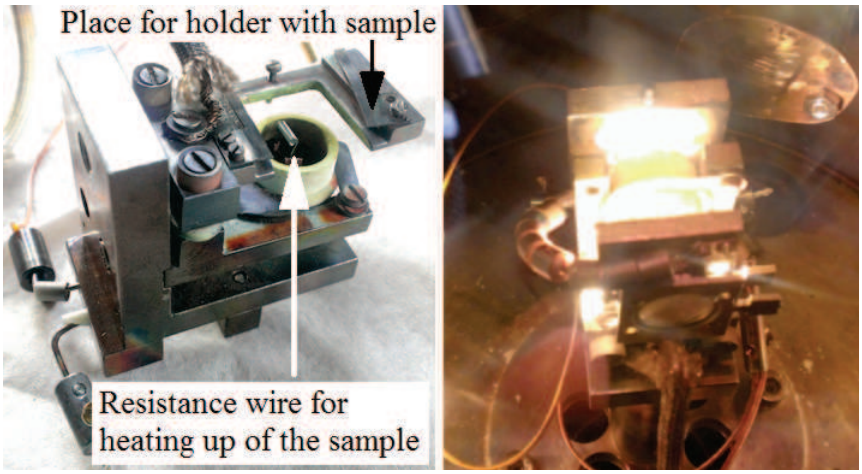

Figure 3.2: *The holder from MBE chamber, where the holder with substrate can be placed is shown in the right side. The process of heating of the substrate is shown in the left side.*

strate temperature.

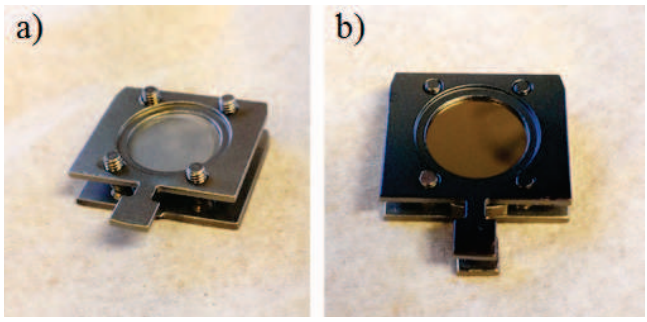

Figure 3.3: *a) Clear substrate in holder and b) substrate with deposited layer (prepared sample) are shown in these pictures.*

Before the deposition process, the substrate must be clean. The substrate was heated at 400 °C for 1 hour in deposition chamber. After cooling of substrate, the substrate was moved by transfer chamber to chamber designed for XPS and LEED measurement. By these techniques we can determine if the substrate is really clean. The substrate can be contaminated by carbon from enviroment, because the substrate was on the air before of its inserting to load-lock chamber. Equipments for XPS and LEED techniques are shown in the picture 3.4. Inside chamber the holder with substrate is placed and prepared for XPS analysis.

If the substrate is clean, the substrate is again transported to deposition chamber, where required layer can be deposited on this substrate. Further, prepared sample (the substrate with deposited layer) is transferred back into the chamber for XPS and LEED analysis. Immediately after deposition, both analyses are performed

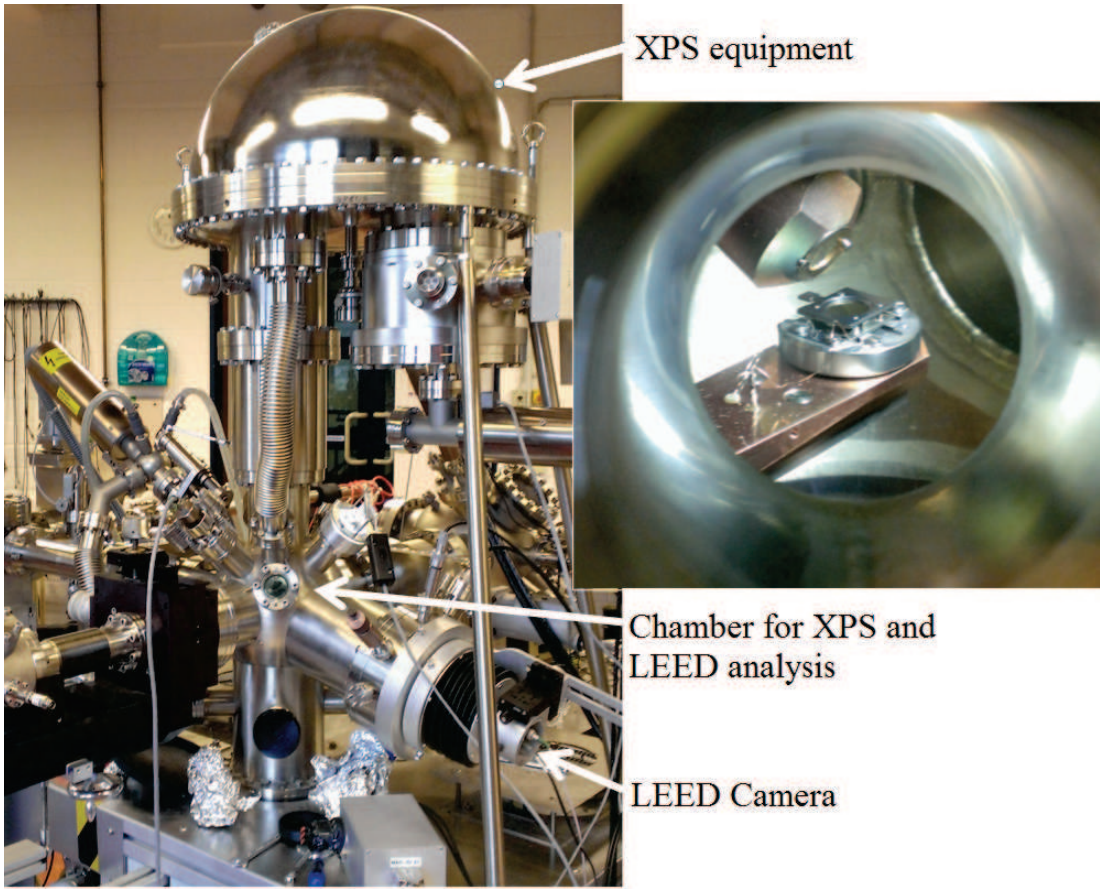

Figure 3.4: *Equipments for XPS and LEED. In chamber the sampler in holder is placed and prepared for XPS measurement.*

to characterize of prepared layer.

If something inside deposition chamber is broken, the chamber must be opened. The sources of guns can be consumed or some parts inside guns or inside deposition chamber can be damaged, For example, the resistance wire to heat up of sample can be broken. Fig. 3.5 shows, how the Ni gun looks like inside.

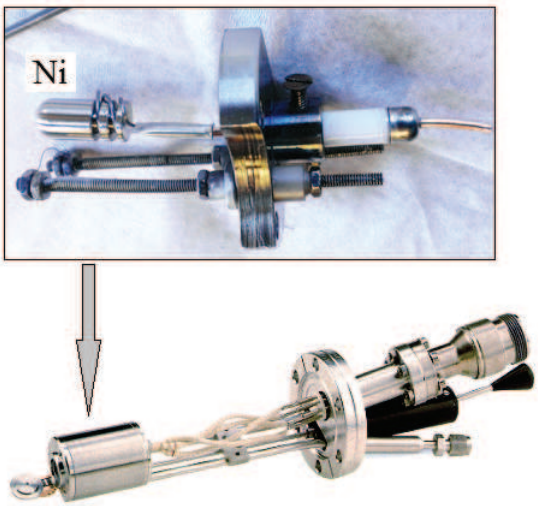

Figure 3.5: *Efussion Knudsen cell and inner part of the Ni gun.* [62]

3.2 Preparation of samples

We prepared two sets of samples. The first set contains magnetite layers deposited on MgO(001) substrate. The second set contains layers of Ni-ferrites on MgO(001) substrate.

The first set contains epitaxial thin layers of magnetite Fe_3O_4 on MgO(001) which were prepared at different pressures of oxygen. Substrate MgO is ideal for epitaxy of Fe_3O_4 due to their close lattice match. In general, MgO substrate is also ideal for other cubic spinels. Both MgO and Fe_3O_4 show cubic symmetry and they are based on fcc oxygen sublattice. Namely, MgO has rocksalt structure with lattice parameter $a_0 = 4.212\,\text{Å}$. Magnetite has inverse spinel structure with lattice paramater $a_0 = 8.396\,\text{Å}$ that is twice larger than the lattice parameter of MgO. Further, the lattice mismatch is only 0.33 %.

Every sample from the first set was prepared at different oxygen pressure (Table 3). In this set the emission of iron source was 35 mA, flux 5 μm, the current in filament to heating the iron source was 2.7 A and voltage 1.3 kV. Temperature of

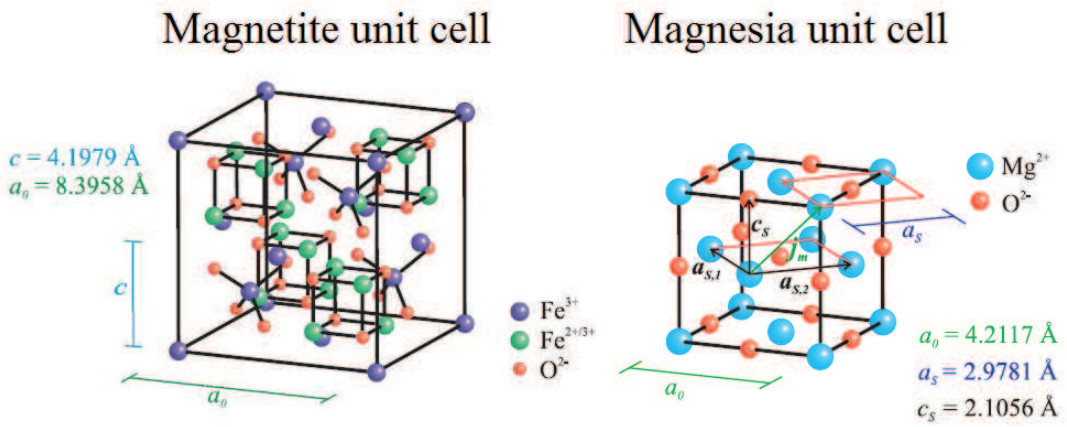

Figure 3.6: *Magnetite unit cell and magnesia unit cell is shown in the picture.* [3]

Number of sample	Pressure of oxygen (mbar)	Pressure of oxygen (Pa)	Pressure of oxygen (mPa)
Sample 1	1×10^{-4}	1×10^{-2}	10
Sample 2	5×10^{-5}	5×10^{-3}	5
Sample 3	1×10^{-5}	1×10^{-3}	1
Sample 4	5×10^{-6}	5×10^{-4}	0.5
Sample 5	1×10^{-6}	1×10^{-4}	0.1

Table 2: *The first set of magnetite thin layers Fe_3O_4 on MgO(001) substrate.*

sample was 250 °C during deposition and time of deposition was 16 minutes. Namely, the shutter of iron gun was opened for 16 minutes and then it was closed.

Preparation of the second set was little different in compare with the first set. Thin layers of Ni-ferrite on MgO(001) substrate were prepared. Two sources (efussion Knudsen cells) had to be used for deposition of Ni-ferrite layers. The Ni emission was same at preparation of every sample from the second set, but the emission of Fe was changed (Table 3). Time of deposition was not same for every sample in this set. The temperature of sample was again 250 °C. The current in the filament that is used for heating of nickel rod was 3 A and voltage was 1.3 kV. For every process the emission of Ni was 26 mA. The current in the filament using for heating of Fe gun was 2.7 A and voltage was 1.3 kV. The pressure of oxygen was 5×10^{-6} mbar.

Number of sample	Fe flux (nA)	Fe emission (mA)	Time of deposition (min)
Sample 1	500	23.5	90
Sample 2	300	21.5	125
Sample 3	5000	34.4	22

Table 3: *The second set of Ni-ferrite thin layers $NiFe_2O_4$ on MgO(001) substrate.*

3.3 Results from used techniques

3.3.1 Atomic Force Microscopy

The measurements were performed at the Atomic Force Microscopy NEXT from NT-MDT company. This technology enables to measure AFM and also STM. The microscope is relatively easily manageable. The high resolution optical microscope is embedded in the AFM. We used AFM measurement at semicontact mode with negative feedback.

Figure 3.7: *The Atomic Force Microscope NEXT from NT-MDT company.* [1]

The golden silicon probes (NSG 30) were used for scanning of the sample surface. Namely, the reflective side of probe was made from gold. The tip curvature radius was 10 nm and height of the tip was specified by manufacturer from 14 to 16 μm. The resonant frequency was 240 - 440 kHz and force constant was in the range 22 - 100 N/m.

From the resulting picture, the surface of the sample is characterized and the value of roughness RMS (root mean square) is identified. Each sample was measured by AFM, only with exception of sample 2 from the first set of magnetite layers

Number of sample	RMS (nm)
Sample 1	3
Sample 3	0.802
Sample 4	0.339
Sample 5	1.908

Table 4: *The values of RMS from the surface area 5×5 μm. The first set of magnetite thin layers on MgO(001) substrate.*

Number of sample	RMS (nm)
Sample 1	5.790
Sample 2	2.880
Sample 3	0.129

Table 5: *The values of RMS from the surface area 5×5 μm. The second set of Ni-ferrite thin layers on MgO(001) substrate.*

deposited on MgO. Figures from the areas 25×25 μm and 5×5 μm of sample surfaces were obtained and the results are shown in pictures from the Fig. 3.9 to the Fig. 3.15. The values of RMS are subtracted from area 5×5 μm and reported in Tab. 4 and Tab. 5.

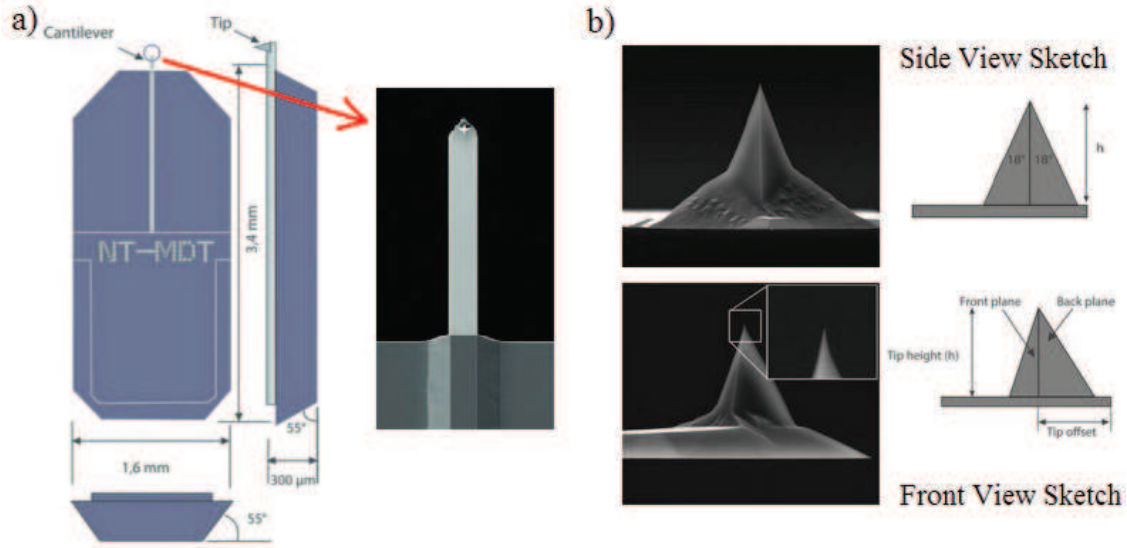

Figure 3.8: *a) Schematic sketch of the golden silicon probe (NSG 30) and the zoomed image of the rectangular cantilever with the tip. b) The side and front view sketch of the tip.* [2]

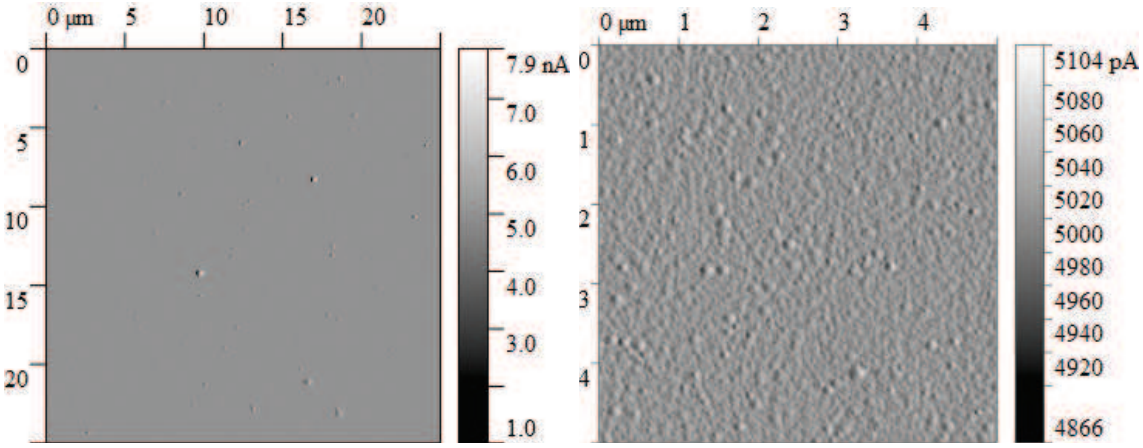

Figure 3.9: *Sample 1 from the first set of magnetite samples.*

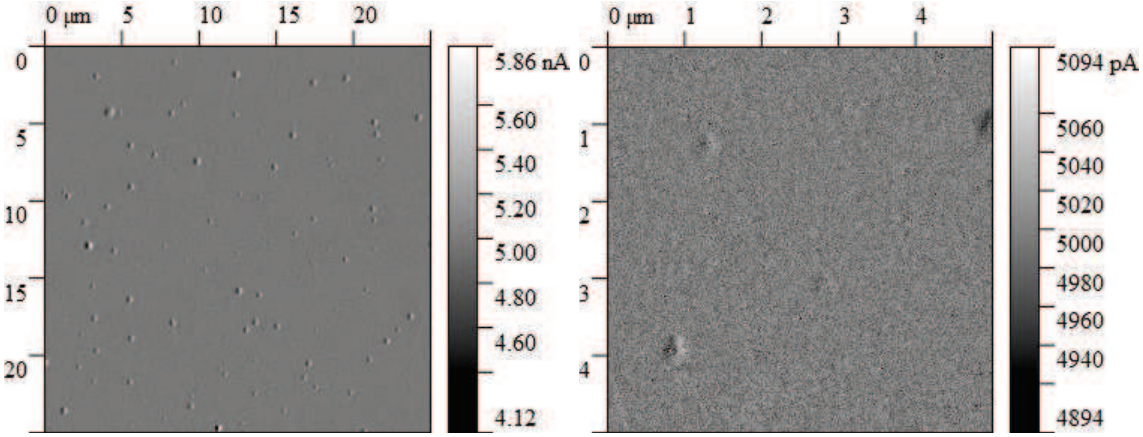

Figure 3.10: *Sample 3 from the first set of magnetite samples.*

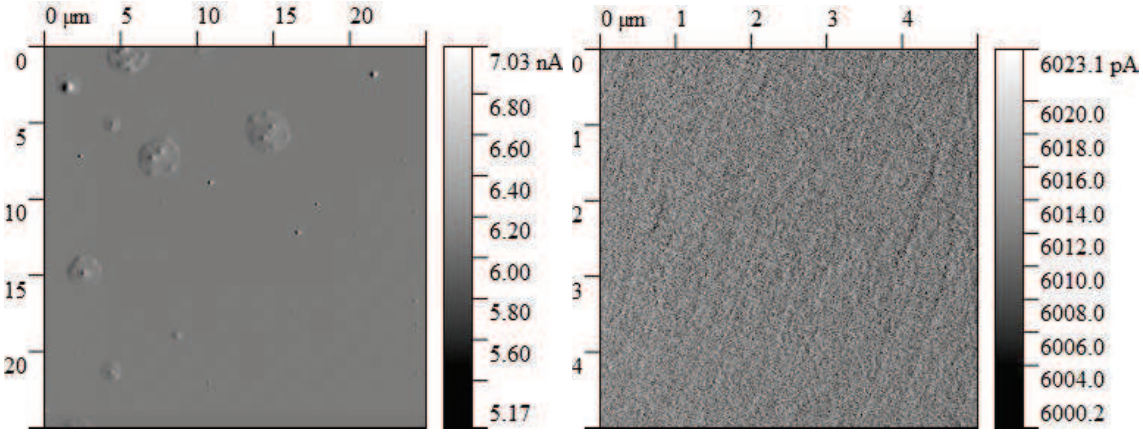

Figure 3.11: *Sample 4 from the first set of magnetite samples.*

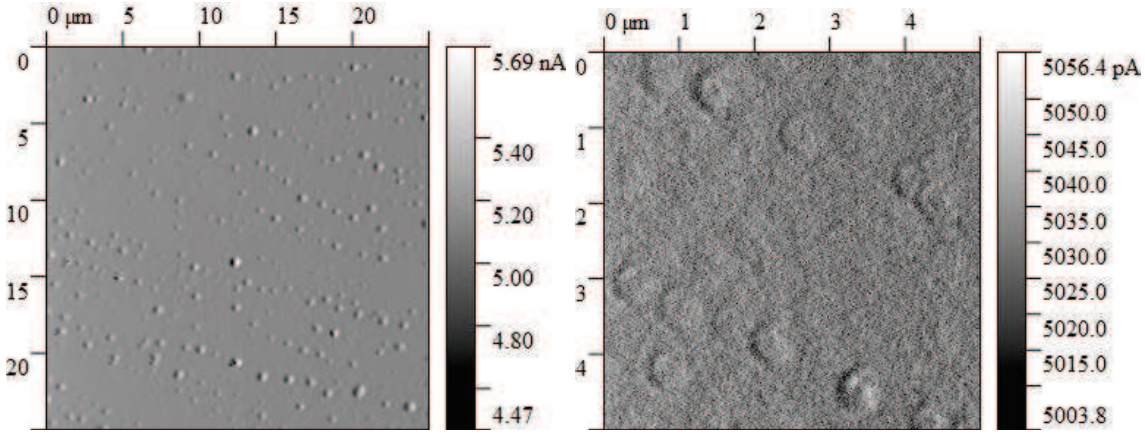

Figure 3.12: *Sample 5 from the first set of magnetite samples.*

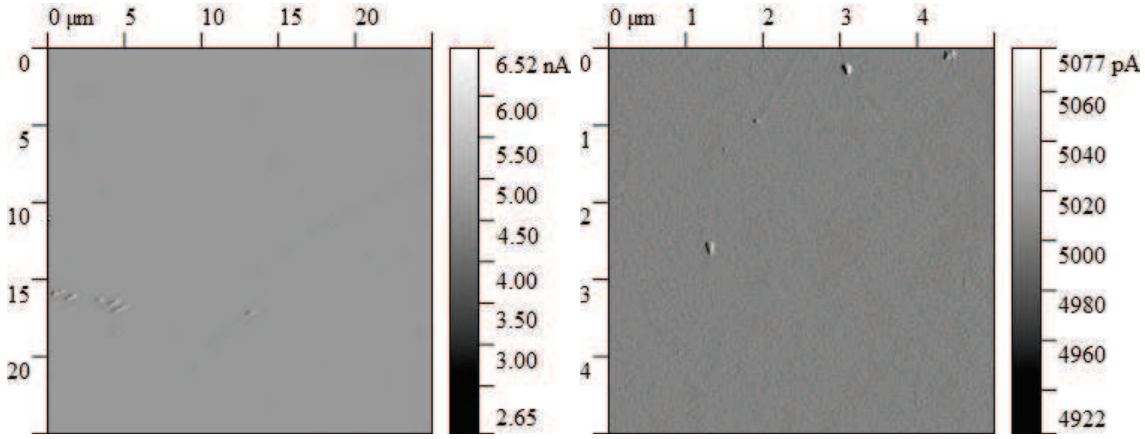

Figure 3.13: *Sample 1 from the second set of Ni-ferrite samples.*

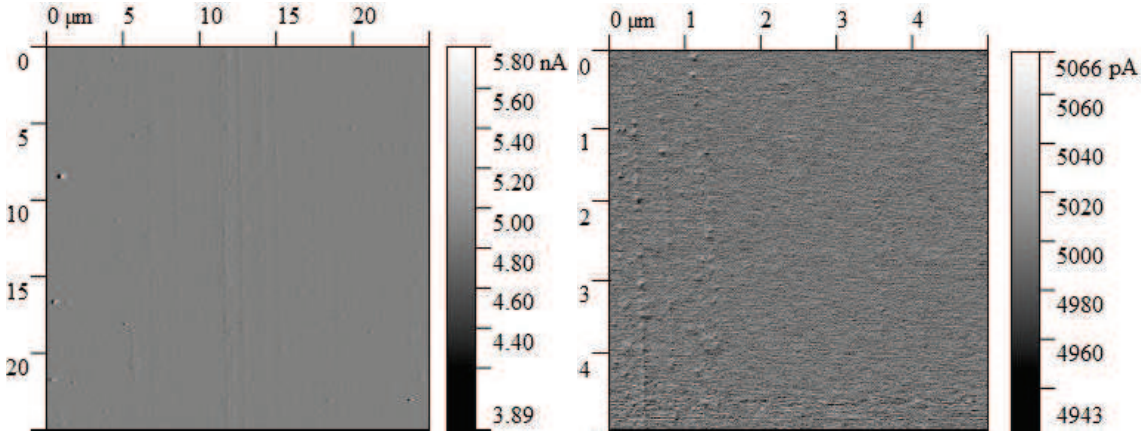

Figure 3.14: *Sample 2 from the second set of Ni-ferrite samples.*

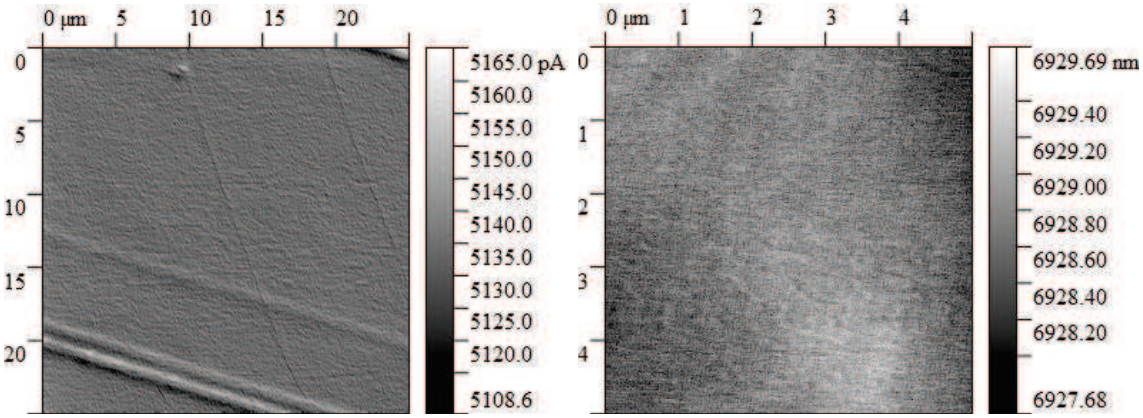

Figure 3.15: *Sample 3 from the second set of Ni-ferrite samples.*

Density (g/cm^3)	Delta $\times 10^{-4}$	Beta $\times 10^{-6}$	Delta/Beta
MgO	1.152	0.123	93.801
Fe_3O_4	1.529	1.399	10.934
$NiFe_2O_4$	1.569	1.039	15.101

Table 6: *The densities of MgO, Fe_3O_4, $NiFe_2O_4$ and corresponding constants delta and beta.* [63]

3.3.2 X-Ray Reflection

The XRR data were obtained by the diffractometer for XRR X'Pert Pro MPD of Philips. The binding energy was 8048 eV. Measured data are shown in pictures from the Fig. 3.16 to Fig. 3.23. In these pictures the dependence of intensity on wavevector q is created. In Tab. 6 are listed every values which are necesary at processing of measured data. The resulting model that is in pictures denoted *sim* provides information about deposited layers. The thicknesses and roughnesses for each sample were obtained (Tab.6). Moreover, each resulting model provided us information about corresponding prepared sample. Each sample consists of the substrate MgO(001) and from two layers on the top. The first layer denotes corresponding deposited layer and the second layer that is usually very thin can denote impurities on the top of deposited layer. The values of thicknesses of both layers and resulting roughnesses of samples are listed in Tab. 7 and Tab. 8. Further, these values were used to process of ellipsometric data.

AFM and XRR data provided us information about roughnesses and thicknesses

Sample name	Thickness of the first layer (nm)	Thickness of the second layer (nm)	Roughness (nm)
Sample 1	63.81	0.86	2.6
Sample 2	50.0	0.46	2.5
Sample 3	50.4	5.96	2.49
Sample 4	56.5	1.60	2.5
Sample 5	65.9	0.74	2.5

Table 7: *Measured and calculated XRR data of the first set of magnetite thin layers on MgO(001) substrate.*

Sample name	Thickness of the first layer (nm)	Thickness of the second layer (nm)	Roughness (nm)
Sample 1	54.6	0.44	0.8
Sample 2	48.3	0.10	0.1
Sample 3	100.4	3.17	1.8

Table 8: *Measured and calculated XRR data of the second set of Ni-ferrite thin layers on MgO(001) substrate.*

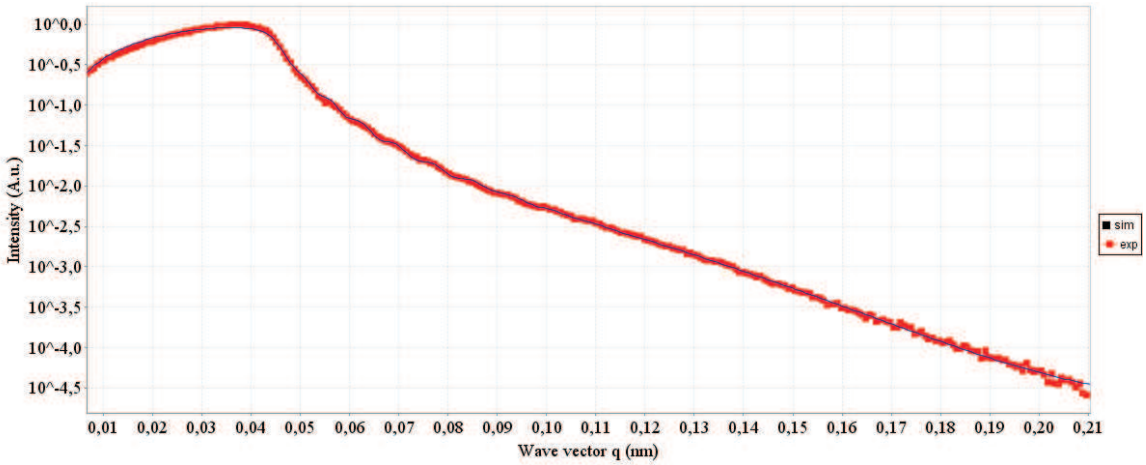

Figure 3.16: *Sample 1 from the first set of magnetite thin layers.*

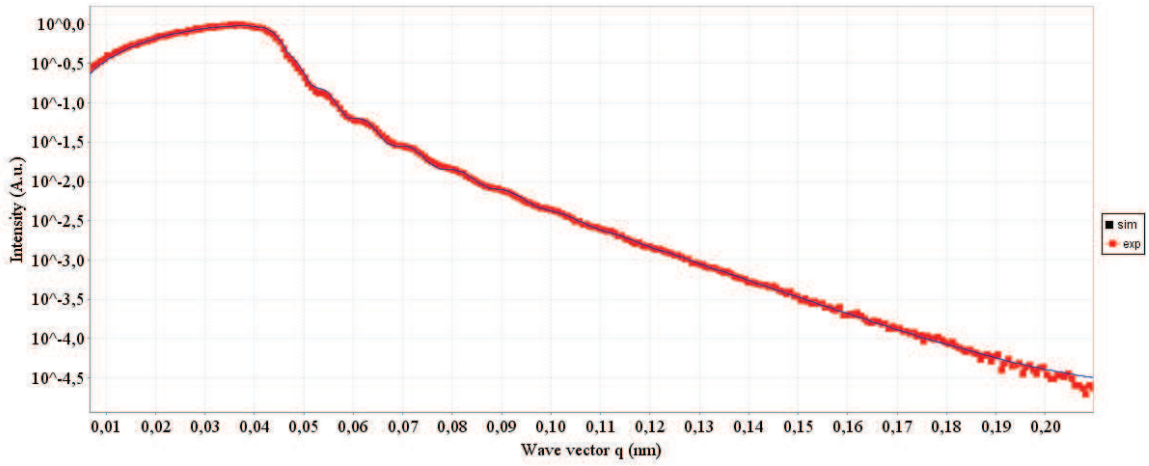

Figure 3.17: *Sample 2 from the first set of magnetite thin layers.*

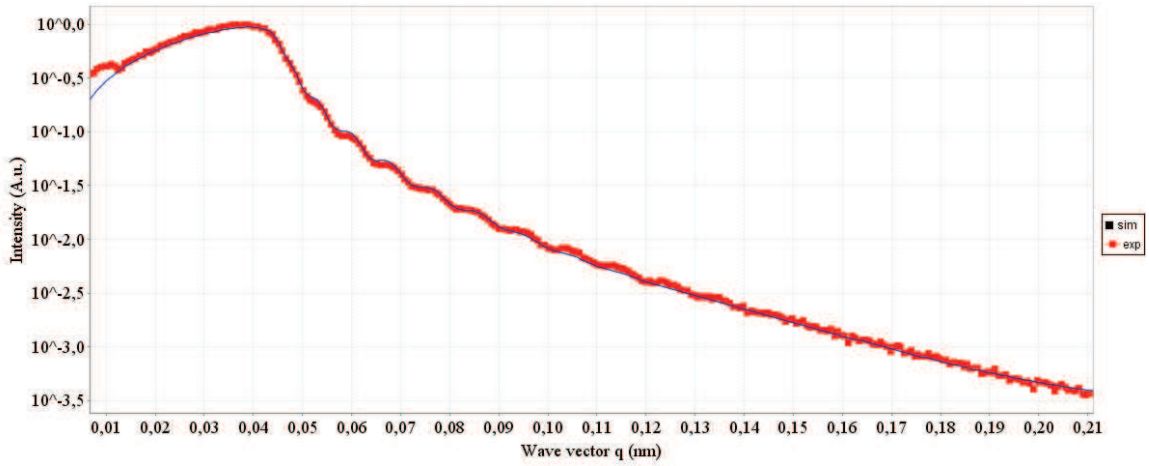

Figure 3.18: *Sample 3 from the first set of magnetite thin layers.*

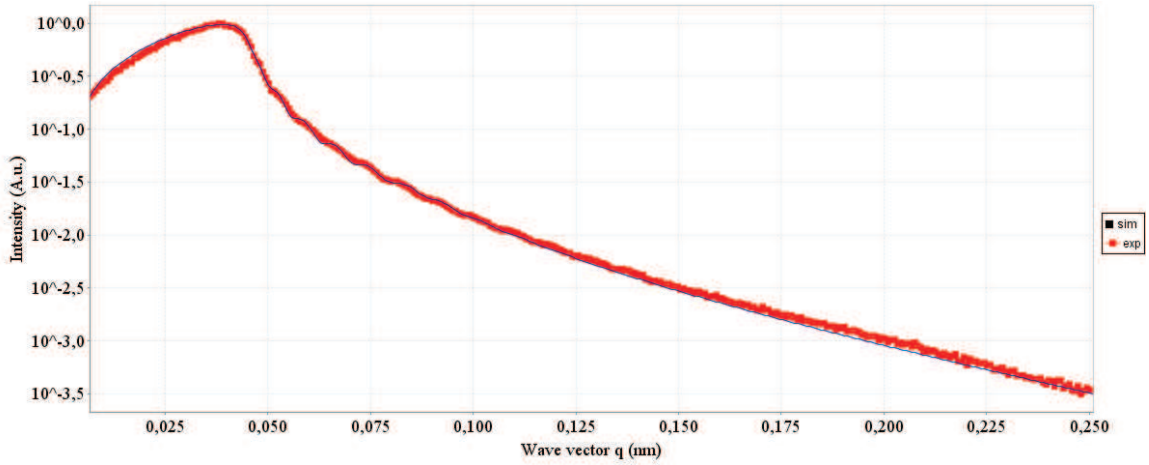

Figure 3.19: *Sample 4 from the first set of magnetite thin layers.*

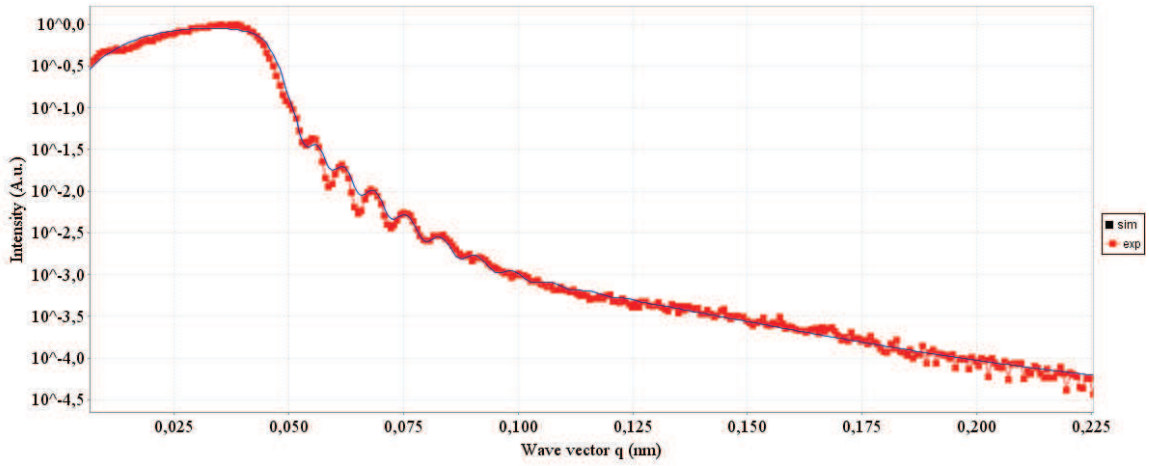

Figure 3.20: *Sample 5 from the first set of magnetite thin layers.*

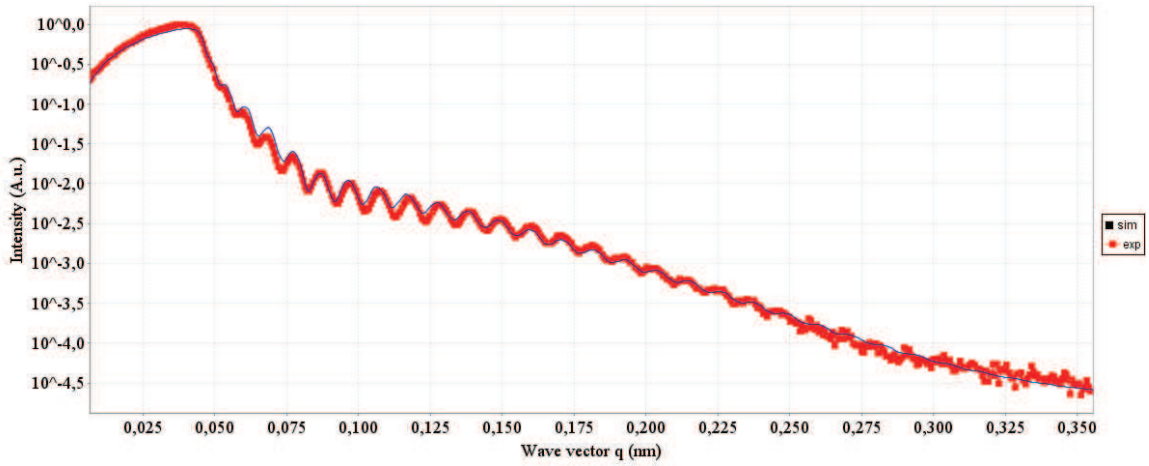

Figure 3.21: *Sample 1 from the second set of Ni-ferrite thin layers.*

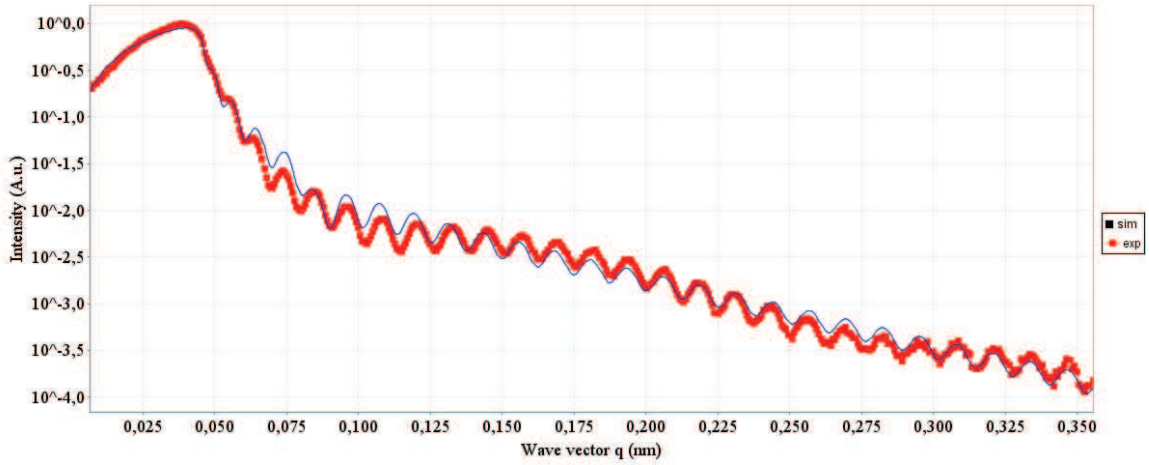

Figure 3.22: *Sample 2 from the second set of Ni-ferrite thin layers.*

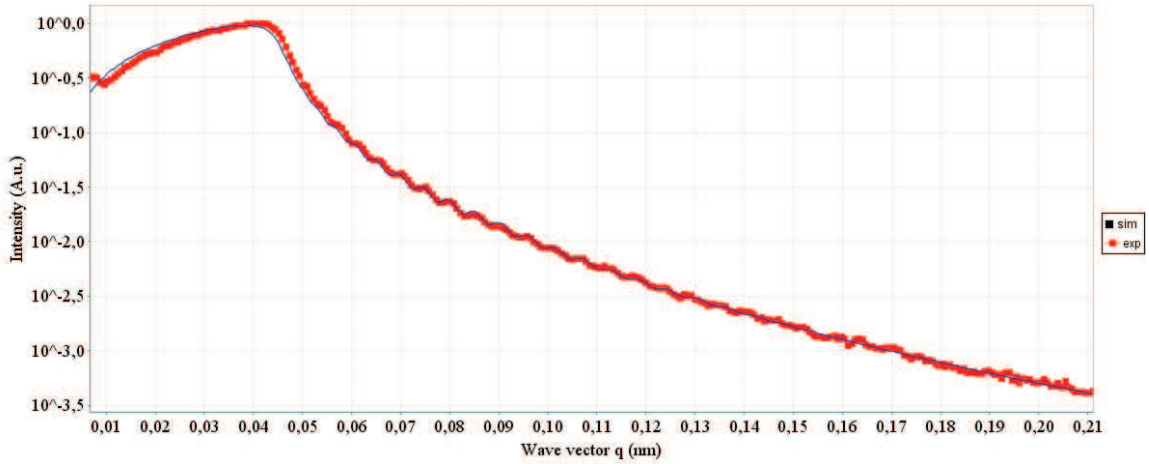

Figure 3.23: *Sample 3 from the second set of Ni-ferrite thin layers.*

of prepared samples. Comparing the roughnesses obtained using AFM and roughnesses obtained using XRR only small differencies at these values are observed. All values of roughnesses are very small, usually around 2.5 nm or lower. One exception is value of roughness 5.8 nm that was obtained using AFM of Ni-ferrite sample 1 (the second set). The highest thickness of impurities corresponds to magnetite sample 3 (the first set).

3.3.3 Low-Energy Electron Diffraction

LEED uses electrons with low energy. Namely, our prepared thin layers were measured in range from 100 eV to 300 eV. For every sample the serie of diffraction patterns was obtained. Then the pattern that the best characterizes the structure was choosen. The diffraction pattern provides information about surface structure in reciprocal space. The diffraction pattern of pure MgO shows (1×1) structure (Fig.3.24). The structure $(\sqrt{2} \times \sqrt{2})$R45° is typical for magnetite and materials with spinel structure.

In figures 3.25, 3.26 and 3.27 the samples of magnetite layers on MgO(001) substrate are shown. In these diffraction patterns the $\sqrt{2} \times \sqrt{2})$R45° structure that is typical for magnetite is observed.

In figures 3.28 and 3.29 the samples of Ni-ferrite layers on MgO(001) substrate are shown. The first diffraction pattern of sample 1 illustrates (1×1) structure and very weak $(\sqrt{2} \times \sqrt{2})$R45° structure. The diffraction pattern of sample 2 shows clear (1×1) structure. From this result we can conclude that oxide of iron with

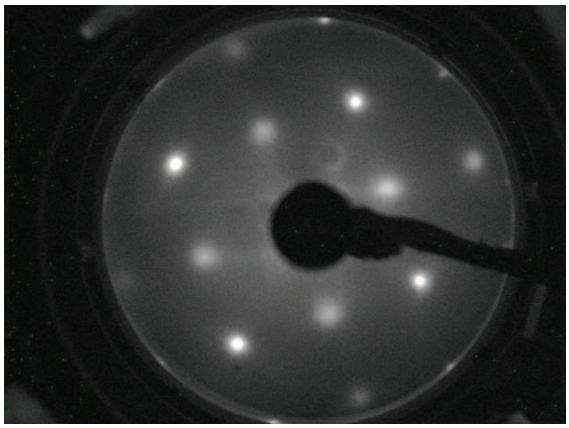

Figure 3.24: *The diffraction pattern of MgO(001) substrate that shows (1×1) structure.*

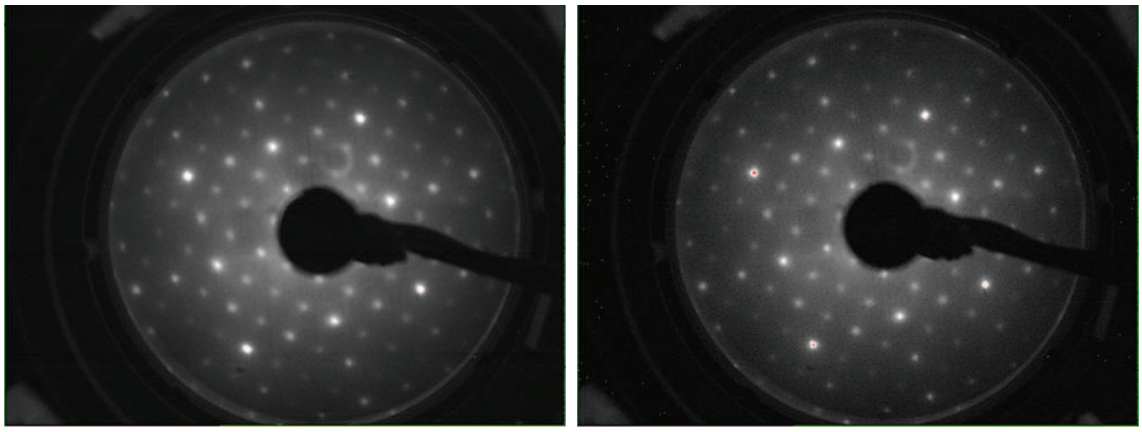

Figure 3.25: *The diffraction patterns of magnetite layers on MgO substrate from the first set. (left side) Sample 1, prepared at 10 mPa (1.10^{-4} mbar) of oxygen pressure, measured at 155eV, shows($\sqrt{2}\times\sqrt{2}$)R45° structure. (right side) Sample 2, prepared at 5 mPa (5.10^{-5} mbar), measured at 155 eV shows ($\sqrt{2}\times\sqrt{2}$)R45° structure.*

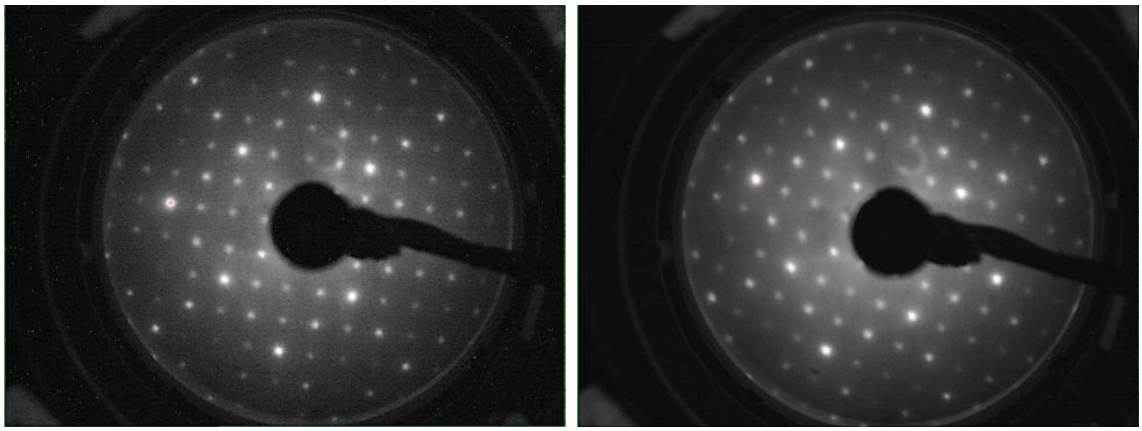

Figure 3.26: *The diffraction patterns of magnetite layers on MgO substrate from the first set. (left side) Sample 3, prepared at 1 mPa (1.10^{-5} mbar) of oxygen pressure, measured at 155eV, shows ($\sqrt{2}\times\sqrt{2}$)R45° structure. (right side) Sample 4, prepared at 0.5 mPa (5.10^{-6} mbar), measured at 155 eV, shows ($\sqrt{2}\times\sqrt{2}$)R45° structure.*

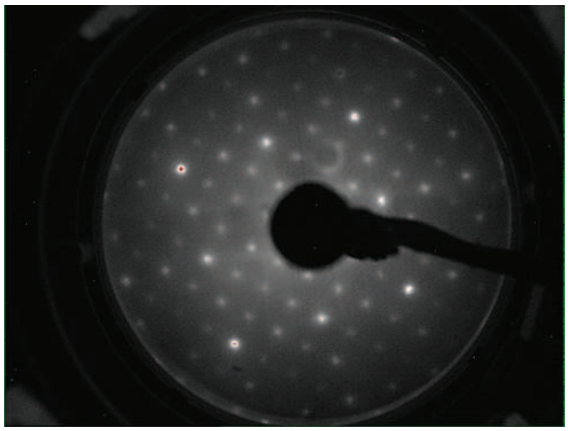

Figure 3.27: *The diffraction pattern of magnetite layer on MgO substrate from the first set. Sample 5, prepared at 0.1 mPa (1.10^{-6} mbar) of oxygen pressure, measured at 155eV, shows ($\sqrt{2} \times \sqrt{2}$)R45° structure.*

spinel structure was not deposited on substrate. Last sample 3 from the second set illustrates again (1×1) structure and weak ($\sqrt{2} \times \sqrt{2}$)R45° structure.

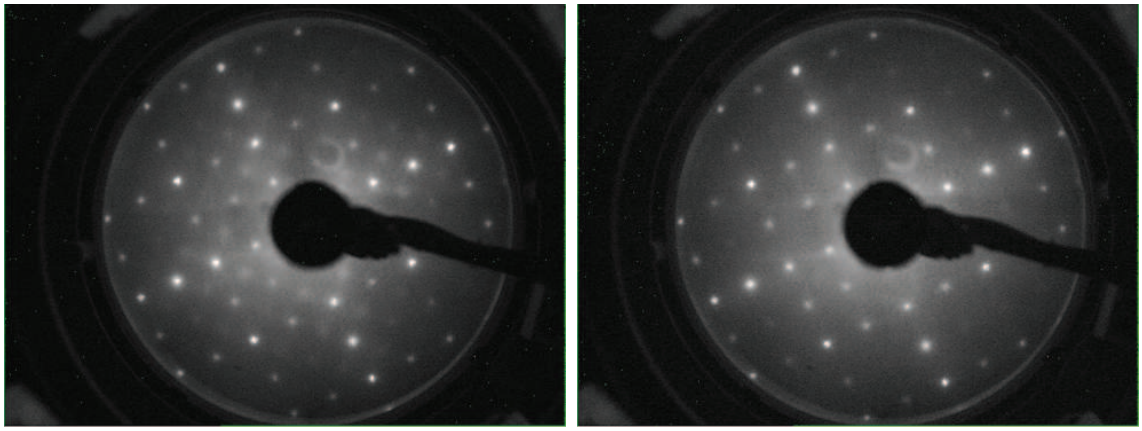

Figure 3.28: *The diffraction patterns of Ni-ferrite layers on MgO substrate from the second set. (left side) Sample 1, prepared at 500 nA of Fe flux and Fe emission equals 23.5 mA, measured at 155eV, shows (1×1) structure and very weakly ($\sqrt{2}\times\sqrt{2}$)R45° structure. (right side) Sample 2, prepared at 300 nA of Fe flux and Fe emission equals 21.5 mA, measured at 155 eV, shows (1×1) structure.*

3.3.4 Vibration Sample Magnetrometry

The model 7407 of Vibrating Sample Magnetometer of company Lake Shore Cryotronics was used for measurement. This model provides magnetic field up to 3.1 T and possibility to measure in temperature range from -4.2 K to 1.273 K. The measured data of our samples were obtained at temperature 305 K. The measurement was performed in range of angles from 0 to 360 ° with step 4 ° at

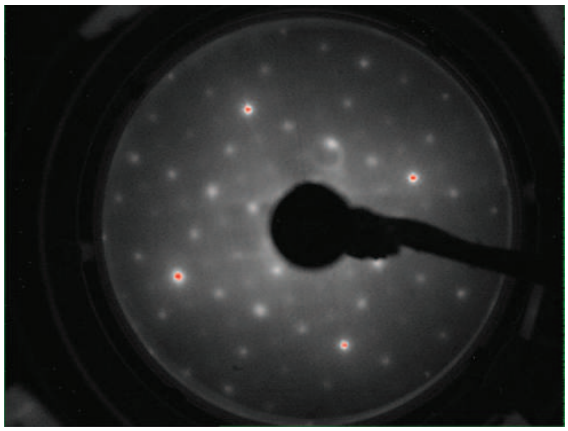

Figure 3.29: *The diffraction patterns of Ni-ferrite layers on MgO substrate from the second set. Sample 3, prepared at 5000 nA of Fe flux and Fe emission equals 34.4 mA, measured at 155eV, (1×1) structure and weak* $(\sqrt{2} \times \sqrt{2})R45°$ *structure.*

the first set of magnetite samples and with step 2 ° at the second set of Ni-ferrite samples. The first measurement was performed for angle 0 ° and for this angle the dependence of magnetic moment of the sample on magnetic field was obtained. This dependence was obtained for each fourth degrees for magnetite samples and for each second degrees for Ni-ferrite samples. Further, the depencies of coercive field, remanent filed and magnetization of samples on magnetic field were obtained. At the first set, the applied magnetic field was 2000 Gauss in the start and subsequently went down to value -2000 Gauss during measurement at certain angle and then the magnetic filed went again back to 2000 Gauss. This course of measurement was performed for every fouth degrees in the range of angles 0 to 360 °. The principle was performed at second set of Ni-ferrite samples, one difference was at value of applied magnetic field that was 20 000 Gauss.

Dependence of saturation magnetization on oxygen pressure during preparation of magnetite layers is shown in the Fig. 3.30. The dashed black line denotes theoretical value $4\,\mu_B$/f.u. $= 630\,\mathrm{mT} = 501\,\mathrm{emu/cm^3}$. [64]

Note that integer value of saturation magnetization in units μ_B/f.u. is due to half-metallic behavior of Fe_3O_4. Similar values where also observed in bulk Fe_3O_4 crystals. [65]

The saturation magnetization determined for our films is lower that this theoretical value, ranging from 385 mT to 514 mT. Surprisingly, the dependence has minimum saturation magnetization for the lowest saturation magnetization is for oxygen pressure 5 mPa. It suggest, there are several phenomena influencing satura-

tion magnetization. One effect might be, that some Fe atoms are in paramagnetic state, reducing outgoing magnetization. Another phenomena might be, that ferrimagnetic spin alignment is disordered and more Fe atoms become FM ordered. This effect was observed in [64], where saturation magnetization of Fe_3O_4 was increased due to presence of interface in 5 nm-thin-films of Fe_3O_4, due to uncompensated spins in ferrimagnetic Fe_3O_4.

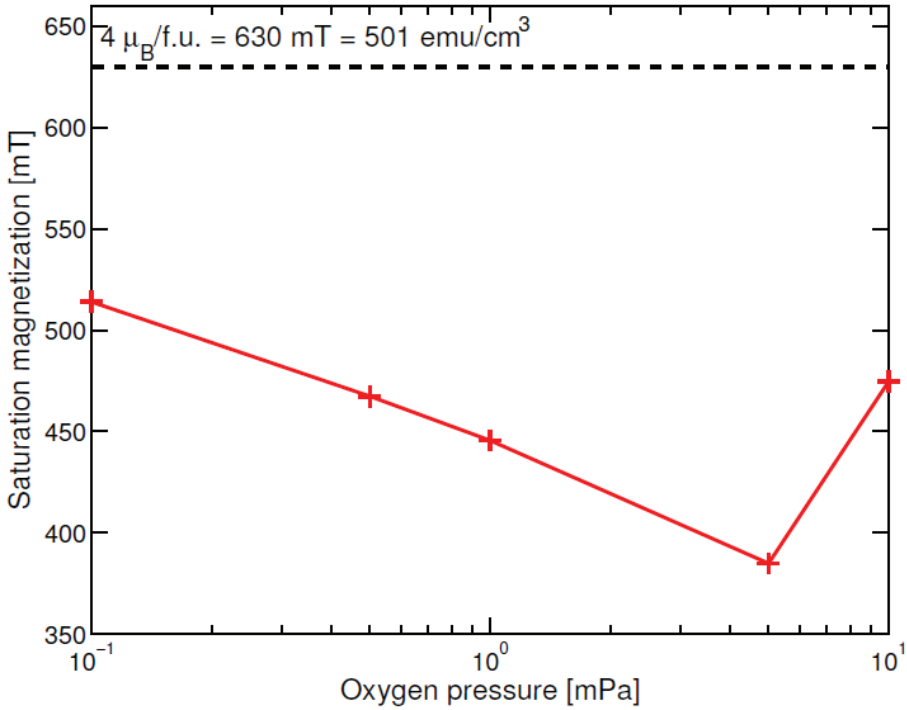

Figure 3.30: *Dependence of saturation magnetization on oxygen pressure during preparation of magnetite samples.*

The dependence of saturation magnetization on Fe flux of Ni-ferrite samples is shown in Fig. 3.31. The largest saturation magnetization was obtained from sample prepared with the smallest Fe flux 300 nA, being 1.02 T (810 emu/cm^3). The remaining two samples, prepared at flux 500 nA a 5000 nA provided similar values, being 154 mT and 140 mT (111 emu/cm^3 and 123 emu/cm^3), respectively. Large variation of saturation magentization in $NiFe_2O_4$ is rather surprising, but we dot have a clear understanding about origin of this feature.

Remanence data are shown in Fig. 3.32 and Fig. 3.33 for magnetite samples. The remanence is shown on two plots. First one is polar plot for all films. Second one is dependence of remanence on oxygen pressure. Value of remanence is nearly 0.9 and nearly constant, reflecting square loops and week 4-fold anisotropy of the

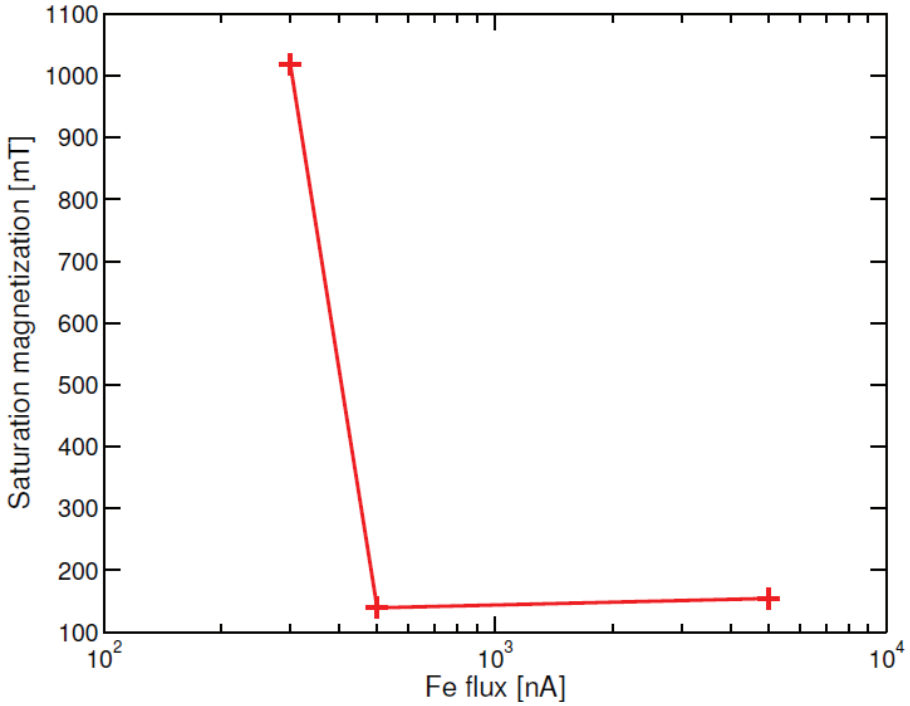

Figure 3.31: *Dependence of saturation magnetization on Fe flux during preparation of Ni-ferrite samples.*

magnetite.

Similar behavior as in saturation magnetization can be observed in remanence for Ni-ferrite samples (Fig. 3.34, Fig. 3.35). Namely, there is large remanence (about 80%) for $NiFe_2O_4$ prepared at flux 300 nA, whereas the remanence drops to 20%–30% for remaining two samples. It reflects a nice square-loop behaviour for sample prepared at 300 nA, and hard-axis-behaviour-like loop for remaining two samples. Also notice, clear 4-fold behaviour is observed only for sample prepared at 5000 nA, probably reflecting very small four-fold magnetic anisotropy for remaining samples. This is in agreement with previous studies on ferrites, demonstrating small spin-orbit coupling and quenched orbital magnetic moment in those compounds.

The coercivity of the loops is shown in Fig. 3.36, Fig. 3.37 and Fig. 3.38 for magnetite samples. Several ways of visualization of coercivity are used. First and second figure shows dependence of coercivity on sample orientation for all samples, shown both in cartesian and polar figure. Last figure shows coercivity as a function of oxygen pressure. In all those visualization, exception sample is one prepared at pressure 0.1 mPa. It suggest, that for this preparation pressure, the sample is low quality from magnetic point of view, with many faults inside the structure, blocking

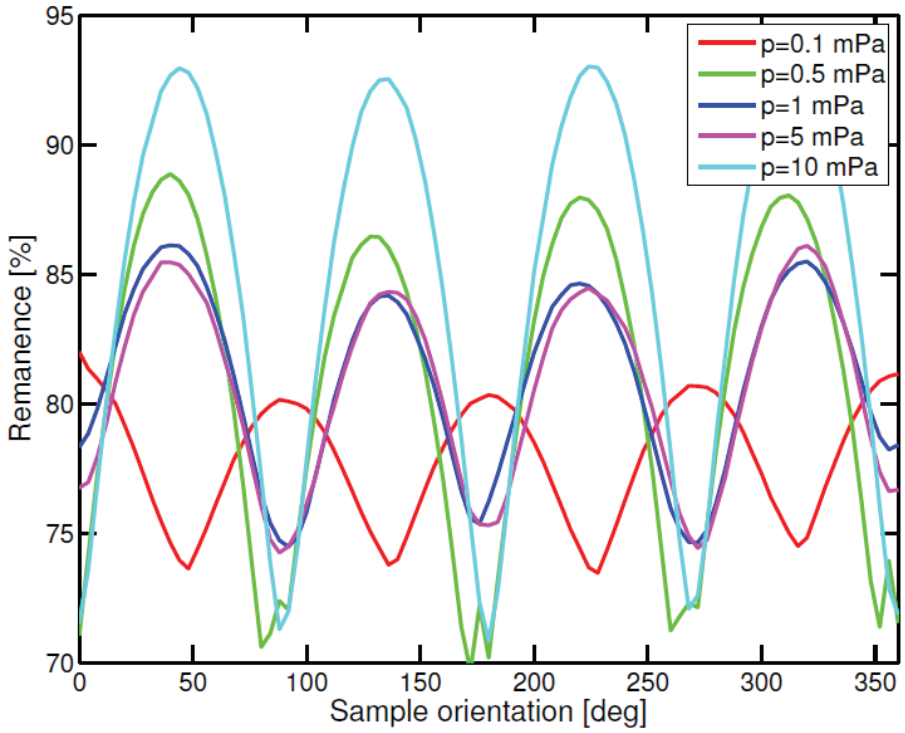

Figure 3.32: *The dependence of remanence on orientation of sample for magnetite set of samples.*

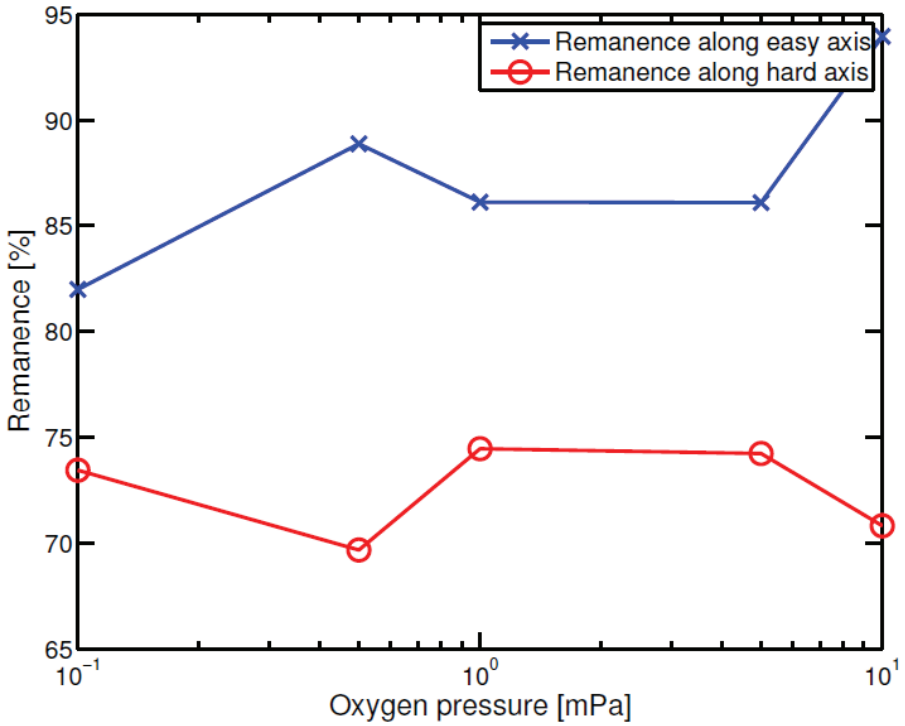

Figure 3.33: *The dependence of remanence on oxygen pressure of magnetite samples.*

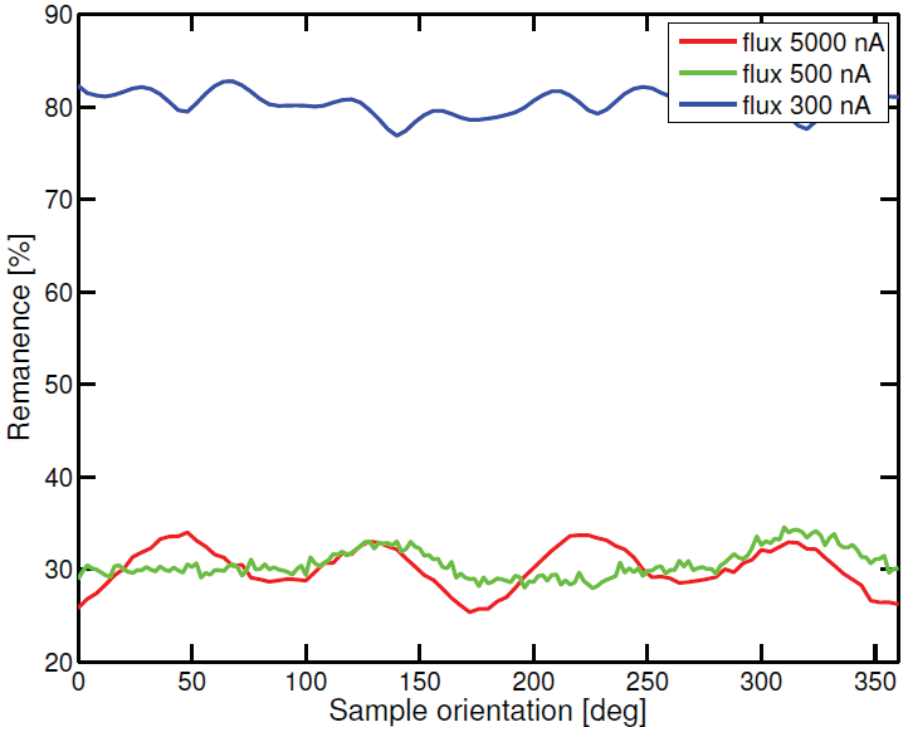

Figure 3.34: *The dependence of remanence on orientation of sample for Ni-ferrite set of samples.*

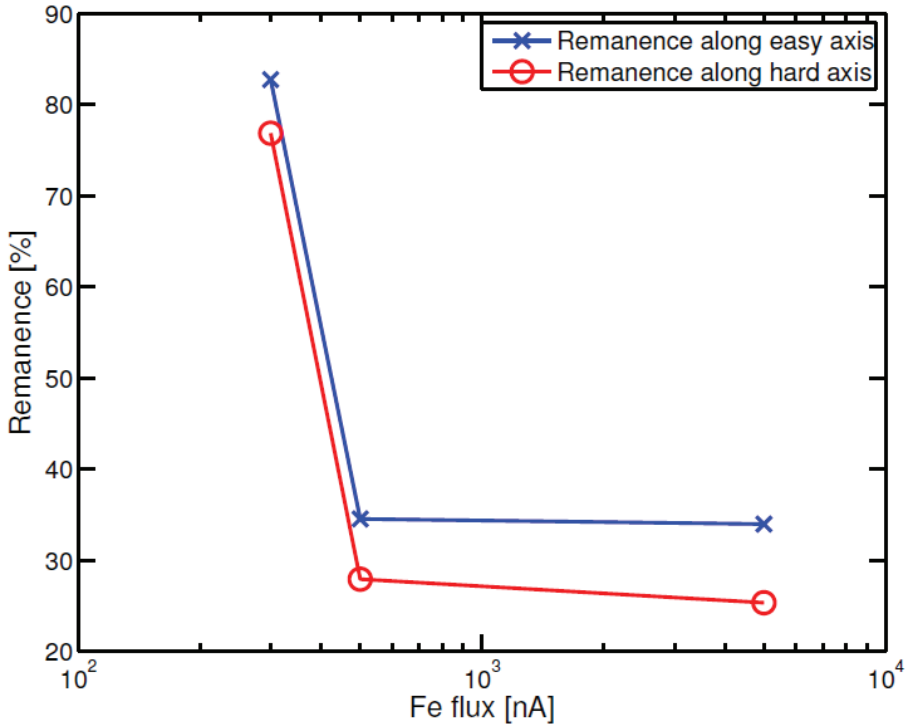

Figure 3.35: *The dependence of remanence on Fe flux of Ni-ferrite samples.*

propagation of domain walls through the layer, hence increasing the coercivity. Also notice that the sample has easy magnetization axis is along (100) MgO axis, whereas in case of other samples, magnetization easy axis is along (110) MgO axis.

Finally, note, that small sharp peaks in hard axis directions measured originated from blocking of magnetic reversal by mutual blocking of magnetic domain propagating in different directions. [66]

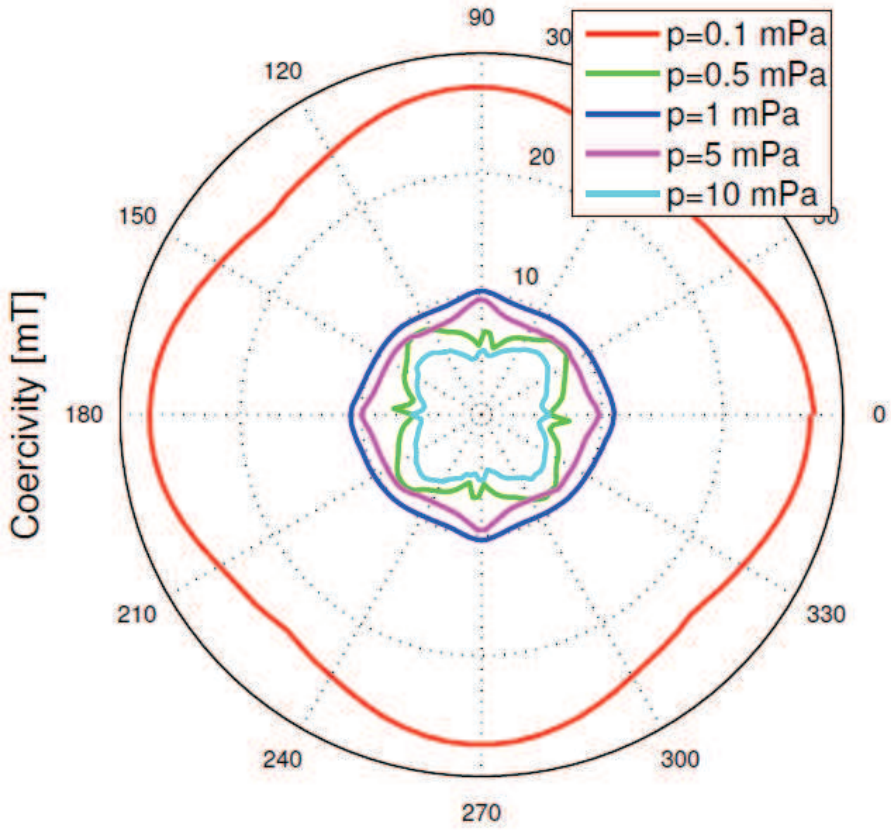

Figure 3.36: *The dependence of coercivity on sample orientation in degrees for magnetite samples.*

The largest coercivity is found for sample from the second Ni-ferrite set, that was prepared at Fe flux 5000 nA, being about 60 mT (Fig. 3.39, Fig. 3.40 and Fig. 3.41). It suggest that at this high speed of film growth, the film contains more defects, blocking propagation of domain walls and hence increasing coercivity. On the other hand samples prepared at flux 300 and 500 nA have much smaller coercivity, being about 12 mT. It suggests that due to slow growth of the film the film is much more smooth and containing less defect, preventing blocking of domain wall propagations.

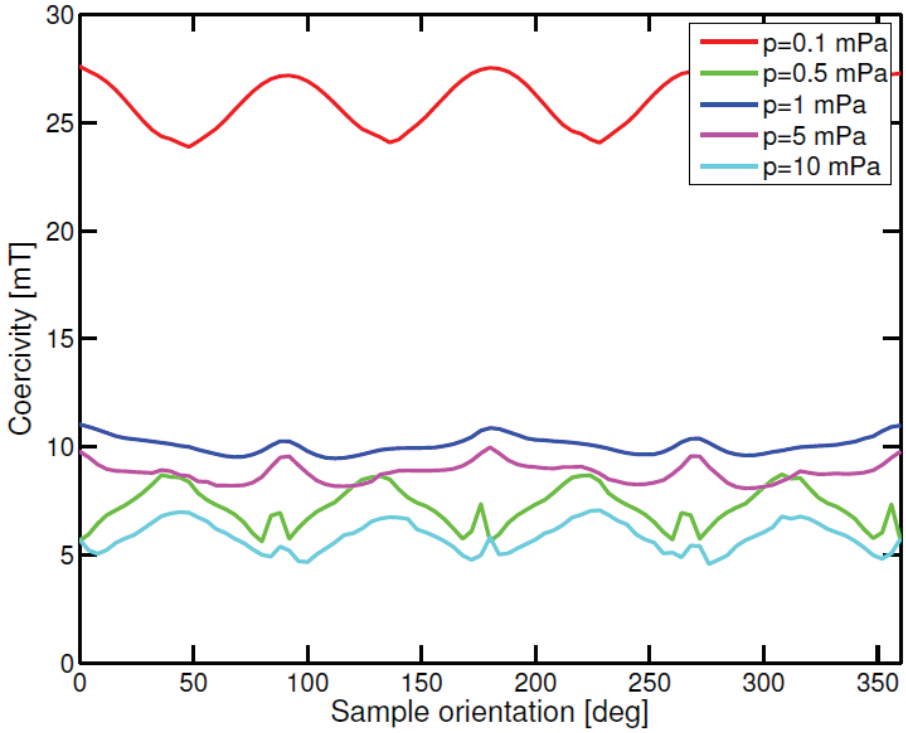

Figure 3.37: *The polar dependence of coercitivity on sample orientation in degrees of magnetite samples.*

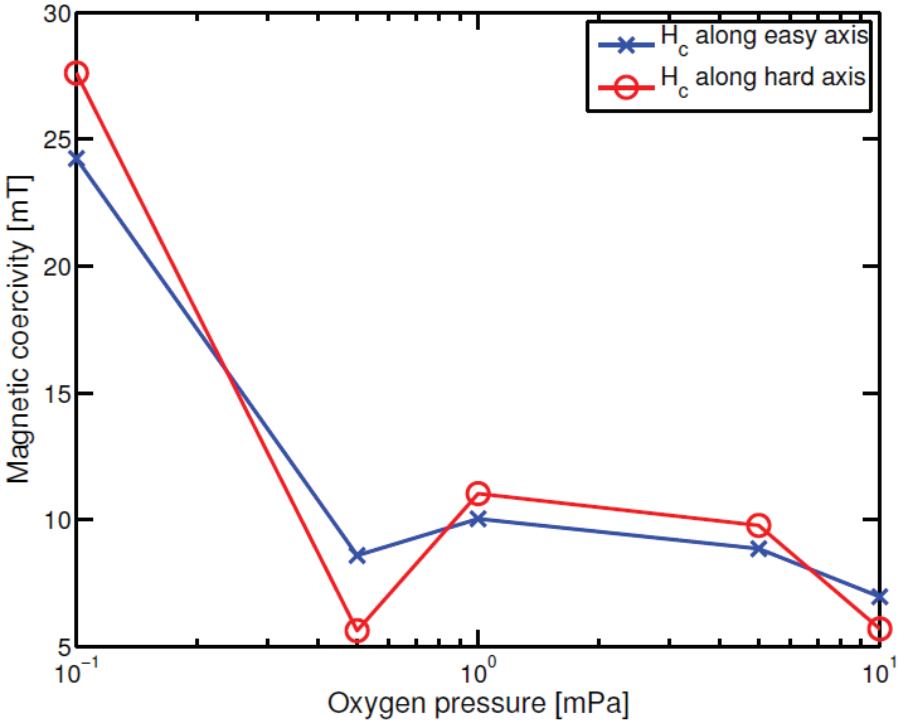

Figure 3.38: *The dependence of coercitivity on oxygen pressure of magnetite samples.*

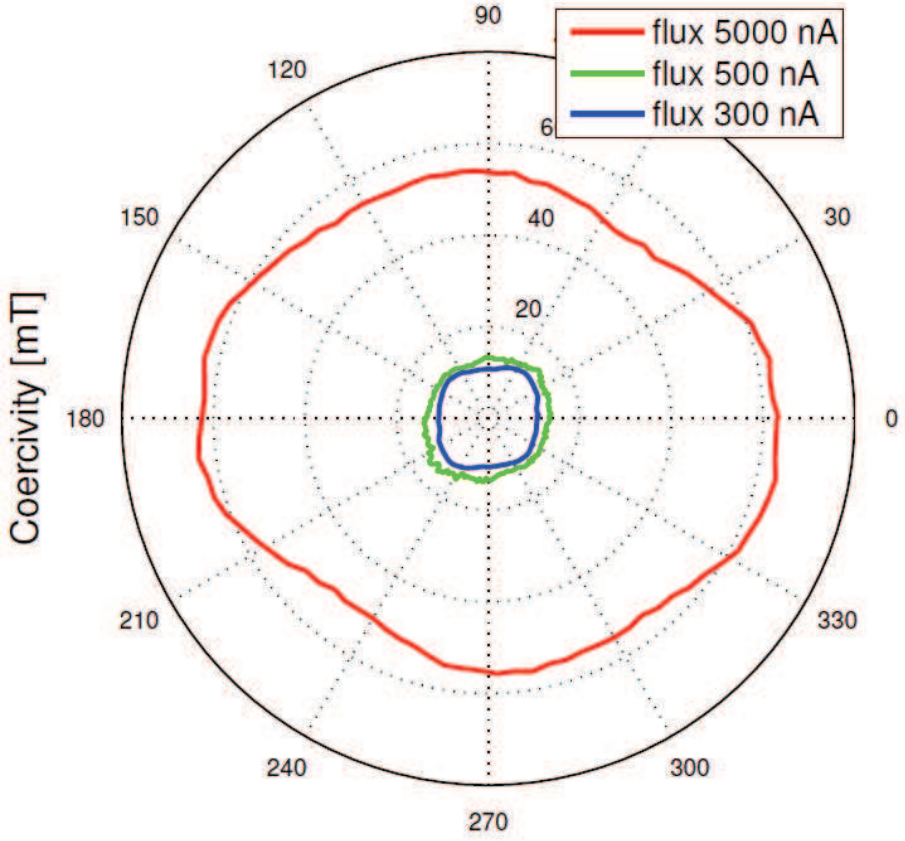

Figure 3.39: *The dependence of coercivity on sample orientation in degrees for Ni-ferrite samples.*

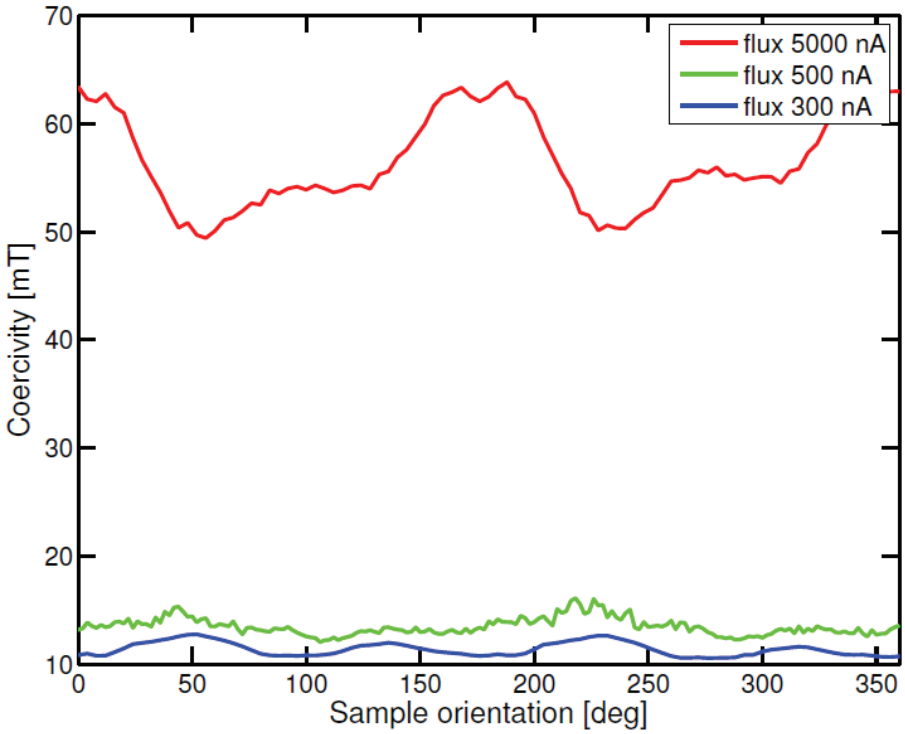

Figure 3.40: *The polar dependence of coercitivity on sample orientation in degrees of Ni-ferrite samples.*

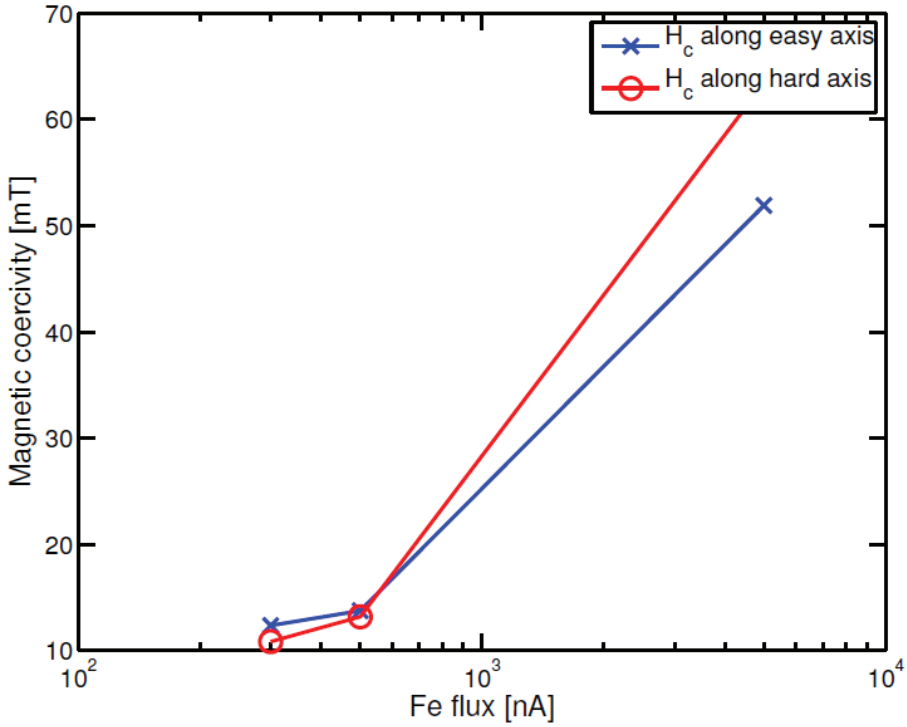

Figure 3.41: *The dependence of coercitivity on Fe flux of Ni-ferrite samples.*

3.3.5 Ellipsometric Spectroscopy

The ellipsometer RC2 from J.A.Woollam Company was used for our measurements (Fig. 3.42). The ellipsometer measures from the ultra-violet to the near infrared range and collects over 1000 wavelengths in this range.

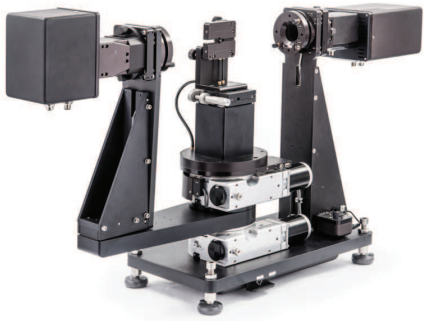

Figure 3.42: *a) The ellipsometer RC2 from J.A.Woollam Company* [56]

Every sample was measured at several angles in range from 40 to 70° with step 5°. The pseudodielectric functions were obtained for every angle in dependence on energy. These data were compiled and the model was created. The function B-spline was used to processing of measured data. The XRR data provide thicknesses and

roughnesses of samples. Knowledge of these values is required for processing of samples by the function B-spline. Figure 3.43 illustrates dependence of pseudodielectric functions *e1* and *e2* on energy for sample 4 (0.5 mPa of oxygen pressure) from the first set of magnetite layers. The model that was created by the function B-spline is also shown in Fig. 3.43.

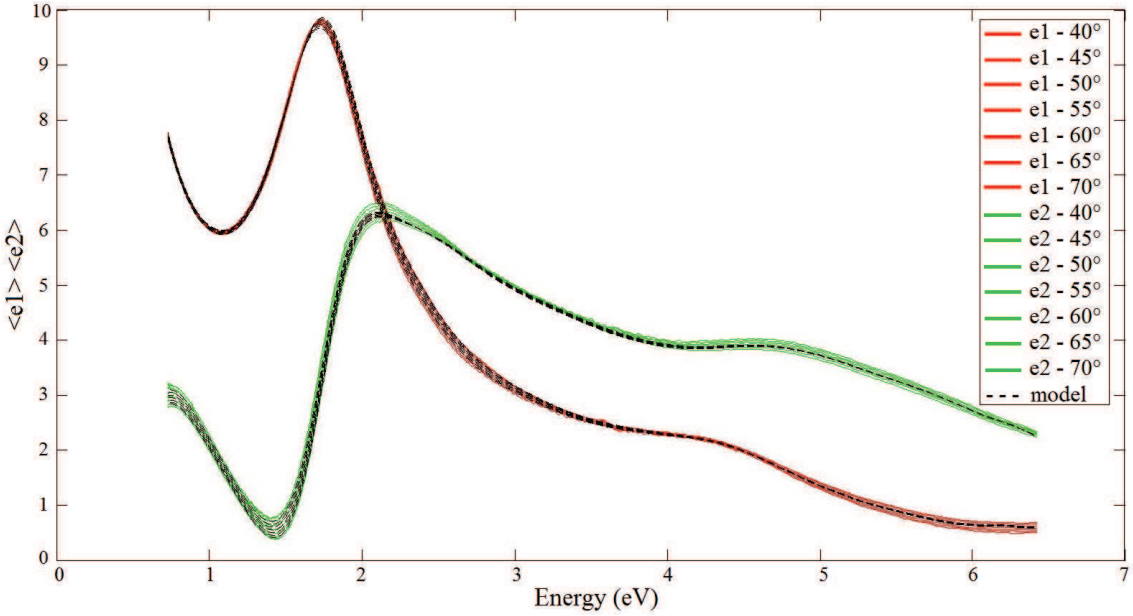

Figure 3.43: *The dependence of pseudodielectric functions e1 and e2 on energy and model providing dielectric function of sample 4 from the first set of magnetite samples.*

The model provides information about optical constants of sample. The resulting dielectric function in dependence on energy is shown in the Fig. 3.44. This dependence provides information about sample 4 with deposited magnetite layers on MgO substrate. Imaginary part of dielectric function *e2* is associated with absorption of material.

The principle of processing of measured data is shown only for sample 4, because the principle is same for each sample. Namely, another samples were also evaluated by the function B-spline, where the knowledges of thicknesses and roughness of samples were used. Dielectric functions in dependence on energy were obtained. The resulting dielectric functions of magnetite samples are shown in the Fig. 3.45. The Drude's contribution is estimated for each curve of magnetite samples around the value of energy 0.5 eV, where the samples are conductive. Another peaks are observed in the Fig. 3.45 around values 2.2 eV and 4.9 eV. These samples have

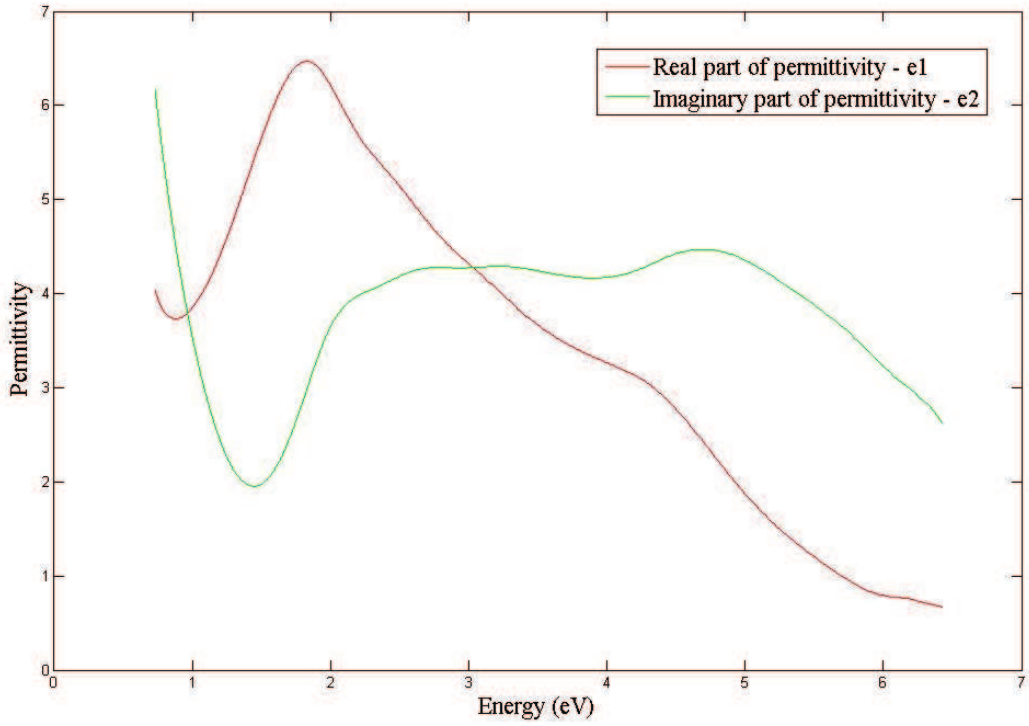

Figure 3.44: *The dependence of resulting dielectric function on energy for sample 4 from the first set of samples.*

similar course of curves, mainly around value of energy 1.5 eV. The largest decline of imaginary part of permittivity at energy 1.5 eV occurs for samples 1 and 2 which were prepared at higher pressures of oxygen (10 mPa and 5 mPa) than other samples.

The sample 5 has different course of dependence permittivity on energy comparing with other samples. This sample was prepared at the lowest pressure of oxygen, 0.1 mPa. The Drude's term is estimated again at value of energy 0.5 eV and other peaks are observed at 2 eV, 3.2 eV and 4.9 eV. Moreover, the peak at energy value 3.2 eV is observed at sample 1 (10 mPa).

The dependencies of resulting dielectric functions on energy for Ni-ferrite samples are illustrated in the Fig. 3.46. The curves are very similar and significant differences are not seen in their course. In the curves three peaks are observed. The first peak is estimated around the value of energy 0.5 eV. The other peaks are observed at energy value 3.9 eV and 5.5 eV. This behavior of imaginary part of permittivity is related with absorption of material. Moreover, peak at energy value 2.8 eV is observed in the blue curve in the Fig. 3.46 that denotes dependence

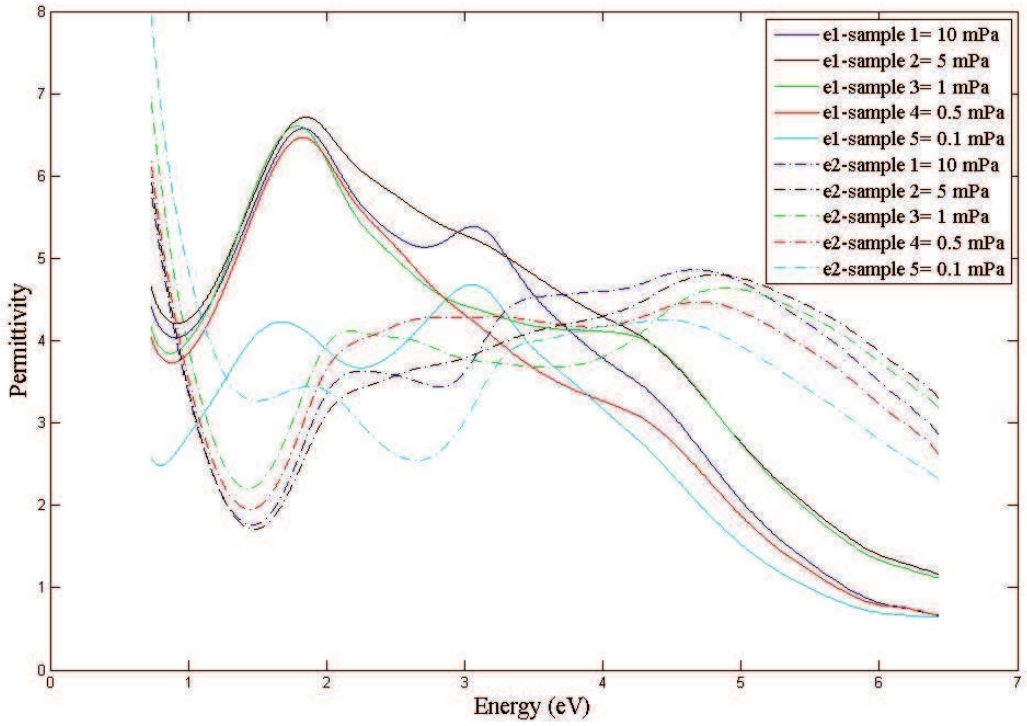

Figure 3.45: *The dependence of resulting dielectric functions on energy for magnetite samples.*

permittivity on energy of sample 1 from the second set of Ni-ferrite samples.

3.3.6 Magneto-optical Spectroscopy

The linear MOKE was measured for samples 1, 3, 4 and 5 from the first magnetite set and for each sample from the second set of Ni-ferrite samples. The dependencies of Kerr rotation and Kerr ellipticity on energy were measured. Subsequently, the material constant K was calculated for each measured sample. The real part of material constant K and imaginary part of material constant K were plotted in dependencies on energy which are drawn in Fig. 3.51, Fig. 3.52, Fig. 3.53 and Fig. 3.54.

At first, the dependencies of Kerr rotation and Kerr ellipticity on energy are drawn. Fig. 3.47 shows the dependence of Kerr rotation on energy for magnetite layers on MgO from the first set of samples. The curves are very similar, only sample 5 (0.1 mPa) is little different. The peaks around energy value 1.25 eV and 4 eV are observed on the curves. The first peak of sample 5 is little shifted to right

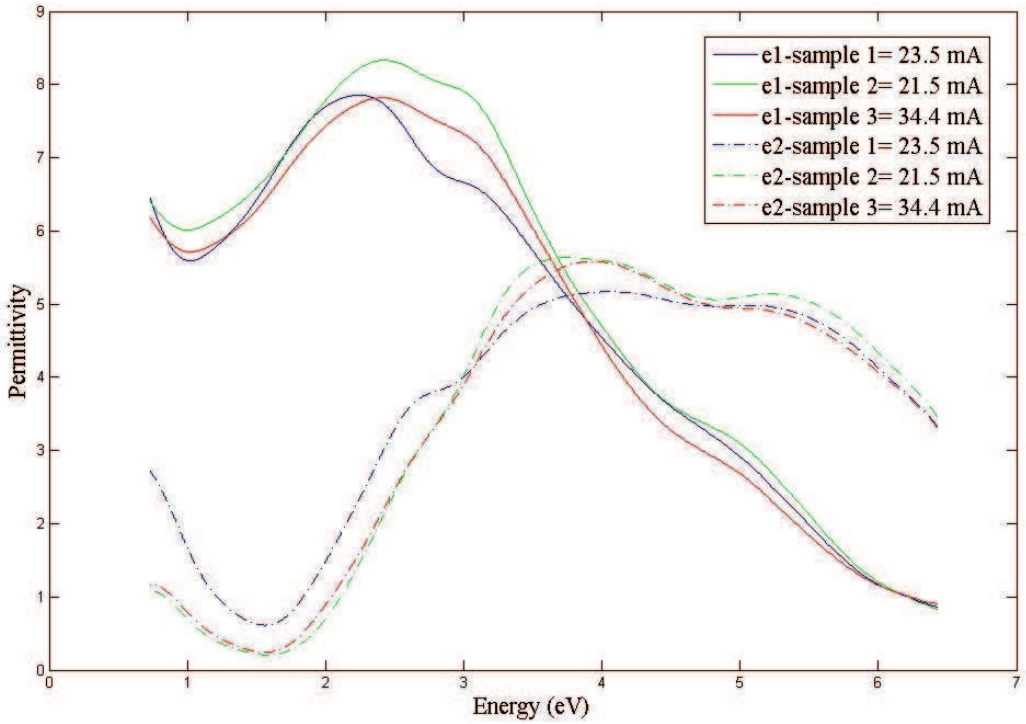

Figure 3.46: *The dependence of resulting dielectric functions on energy for Ni-ferrite samples. The value of Fe emission 23.5 mA corresponds to value of Fe flux 500 nA (sample 1), the value of Fe emission 21.5 mA corresponds to value of Fe flux 300 nA (sample 2) and the value of Fe emission 34.4 mA corresponds to value of Fe flux 5000 nA (sample 3).*

side comparing with other samples. This sample exhibits the highest value of Kerr rotation by compared to other samples from the first set of magnetite samples.

The same behaviour of curves is observed at Fig. 3.48, where the dependence of Kerr ellipticity on energy is shown for samples with deposited magnetite layer. The samples 1, 3 and 4 are again very similar and sample 5 is little different. The highest value of Kerr ellipticity is observed on the curve of sample 5 (the lowest pressure of oxygen). The first peak is observed at energy value about 1.5 eV for each sample with the exception of the sample 5 that is again shifted to right side. The second peak is seen at energy value 4.75 eV for each listed sample.

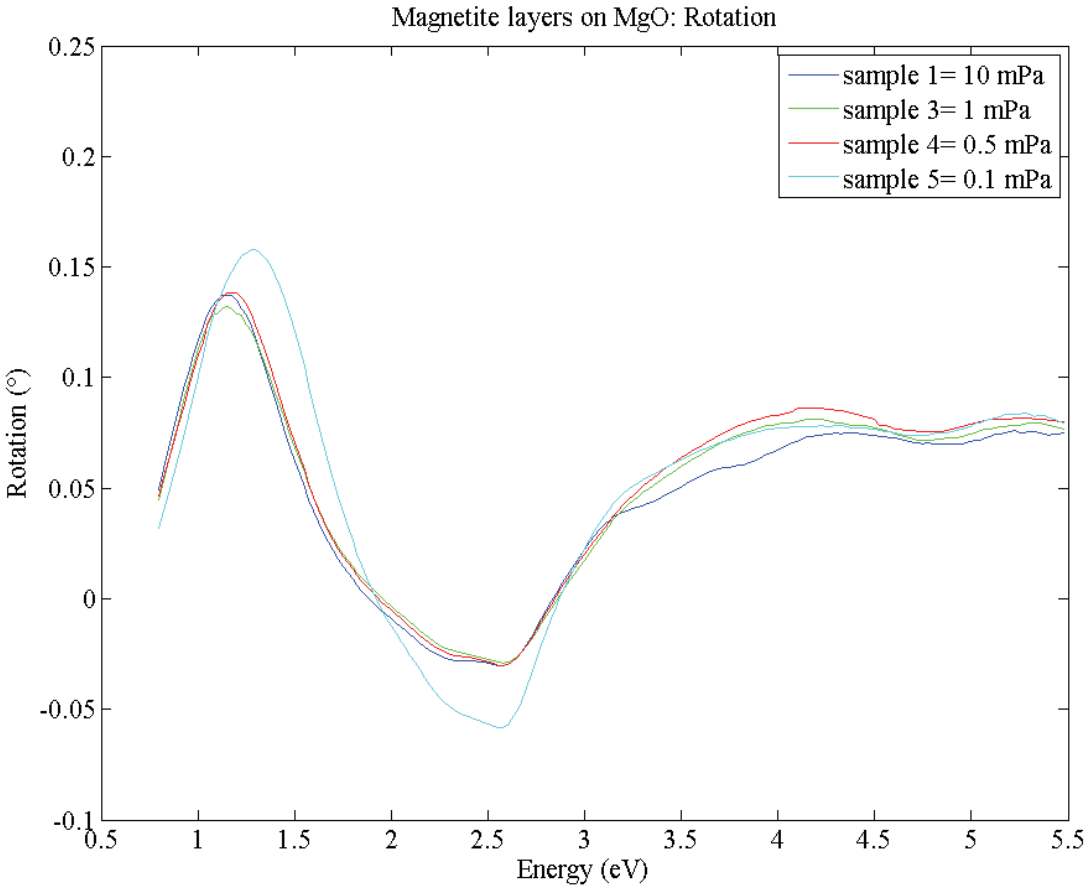

Figure 3.47: *Kerr rotation of magnetite layers on MgO substrate from the first set of samples.*

The Kerr rotation of samples from the second set is shown in the Fig. 3.49. Comparing of the values of Kerr rotation of Ni-ferrite samples with the values of Kerr rotation of magnetite samples, the values of Kerr rotation of Ni-ferrite samples are lower. One exception is sample 1 from the second set, where its value of Kerr

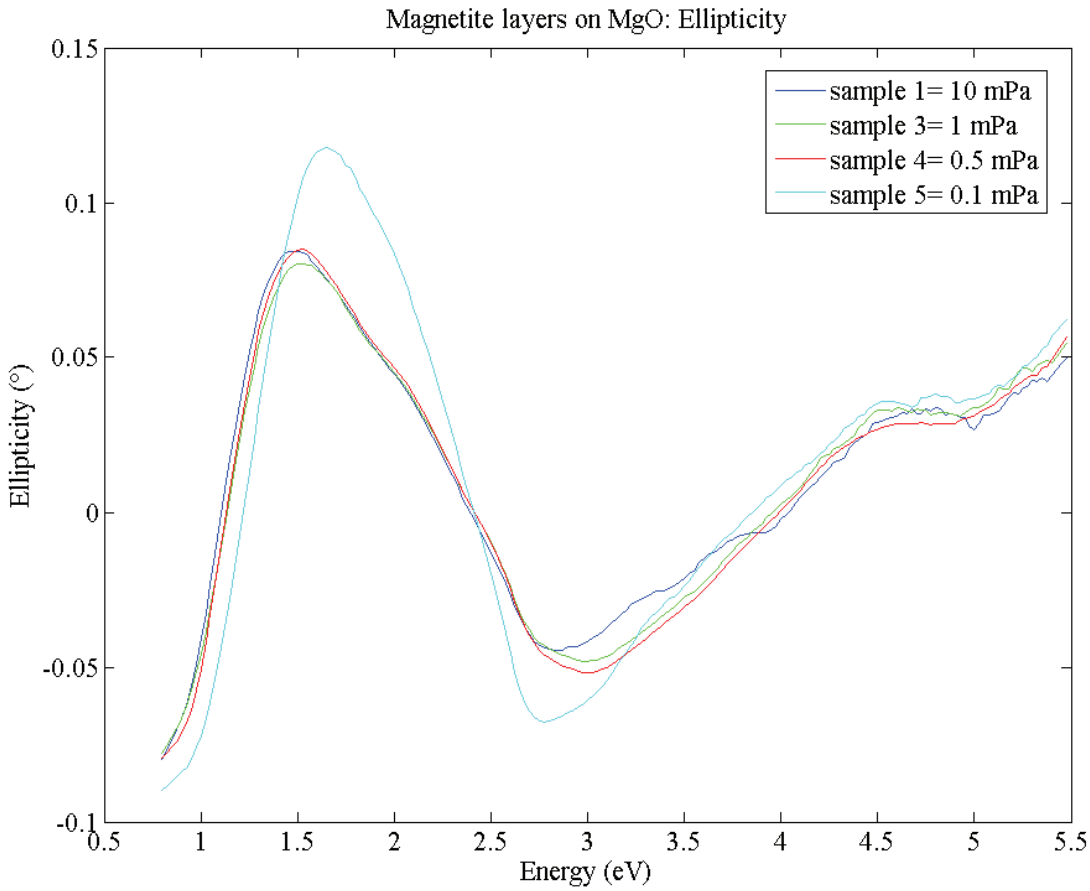

Figure 3.48: *Kerr ellipticity of magnetite layers on MgO substrate from the first set of samples.*

rotation is comparable to values of Kerr rotation of samples from the first set. In the Fig. 3.49 peaks around 1 eV, 2.4 eV, 2.8 eV and 4.5 eV are observed. In the Fig. 3.50 the dependence of Kerr ellipticity on energy is illustrated. The curves of listed samples have peaks around 1.2 eV, 3 eV and 4.8 eV. The highest value of Kerr ellipticity is in the Fig. 3.50 observed on the curve of sample 1 (blue curve). Kerr ellipticity is associated with absorption of materials.

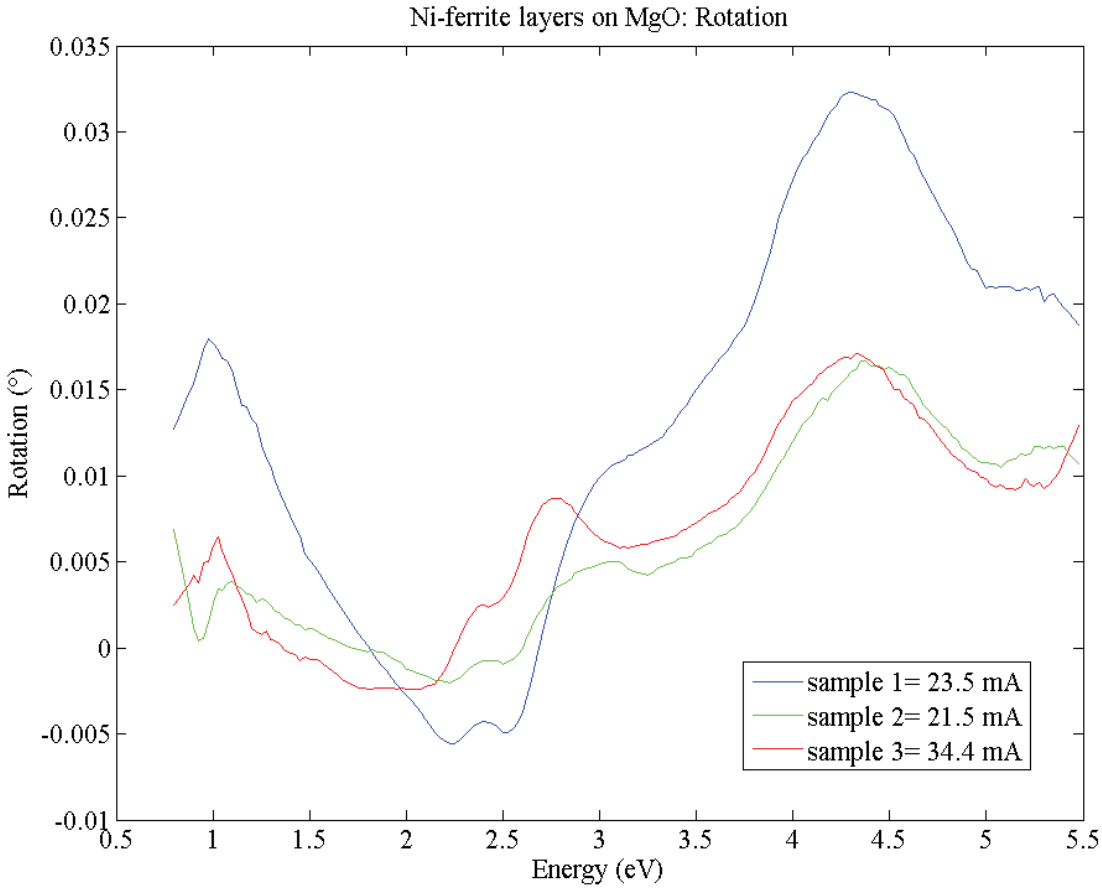

Figure 3.49: *Kerr rotation of Ni-ferrite layers on MgO substrate from the second set of samples.*

The dependencies of real part of material constant K and imaginary part of material constant K are plotted in Fig. 3.51, Fig. 3.52, Fig. 3.53 and Fig. 3.54.

In the first set of magnetite samples the curves of real part of material constant K and the curves of imaginary part of material constant K are very similar for sample 1, 3 and 4. Sample 5 exhibits little different course of curve. In the Fig. 3.51 peaks around energy values 0.5 eV, 3.5 eV and 5.2 eV are observed. One exception is for sample 5, where the first peak is shifted to energy value 1.2 eV.

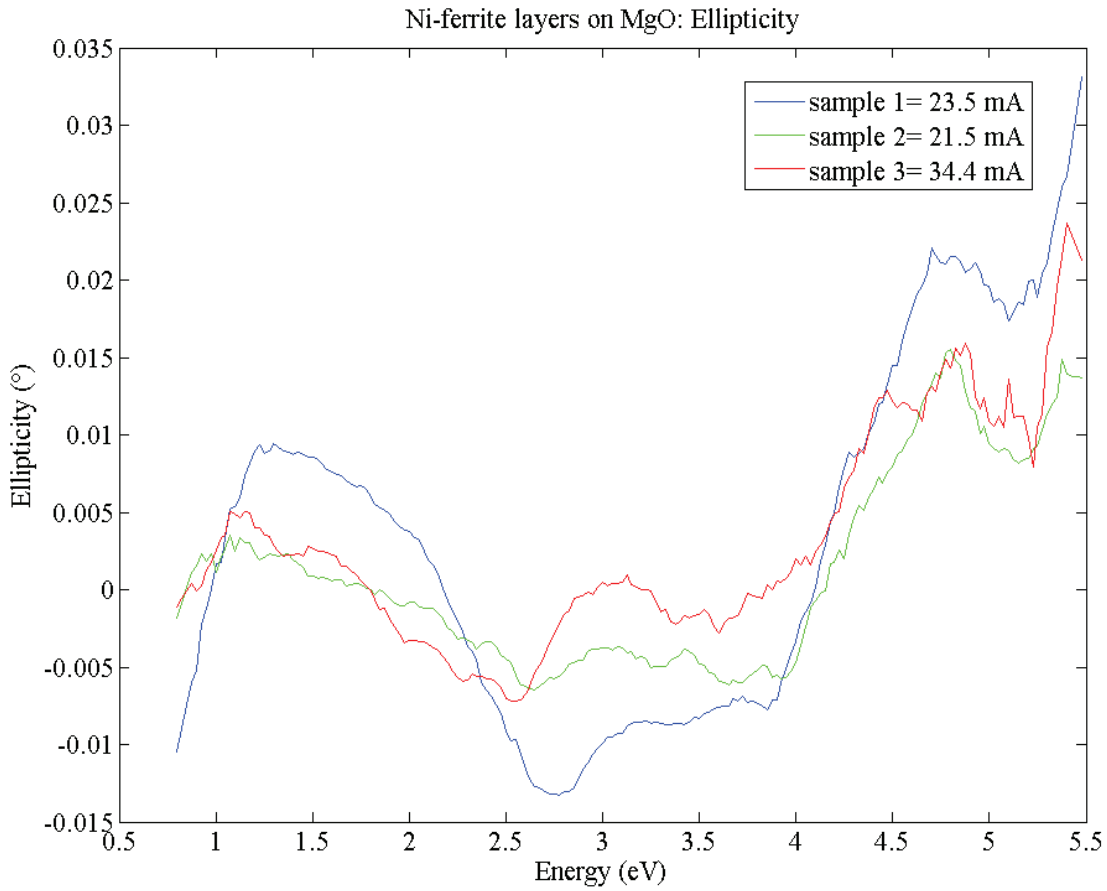

Figure 3.50: *Kerr ellipticity of Ni-ferrite layers on MgO substrate from the second set of samples.*

In the Fig. 3.52 peaks around energy values 1.1 eV, 2 eV and 4.7 eV are drawn. Only two peaks are observed for sample 5 at values 1.6 eV and 4.7 eV.

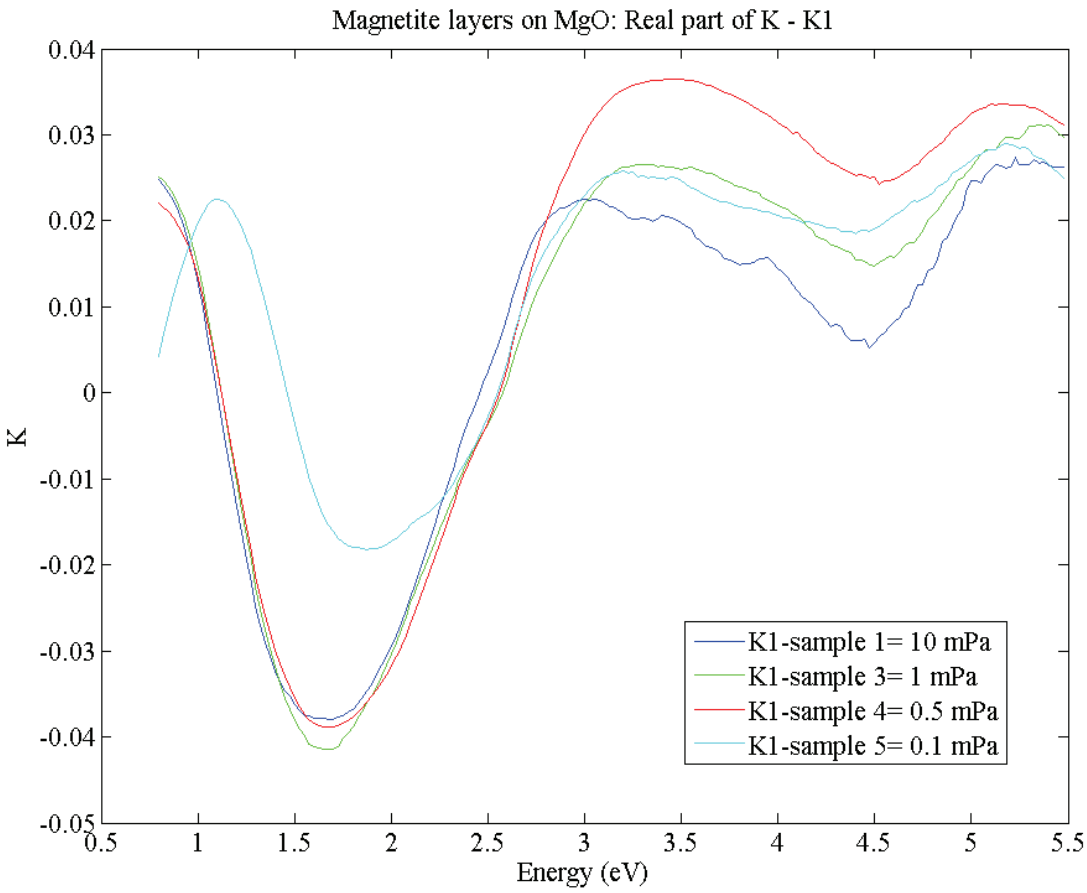

Figure 3.51: *The dependence of real part of material constant K on energy for the first magnetite set of samples.*

In the second set of Ni-ferrite samples, the Fig. 3.53 corresponds to dependence of real part of material constant K on energy. We must mention that the real part of material constant K is associated with absorption of material. In the Fig. 3.53 the values of real part of material constant K are very low. The peaks at 2.6 eV, 3.8 eV and 5.2 eV are observed.

Fig. 3.54 corresponds to dependence of imaginary part of material constant K on energy with peaks around 3 eV and 4.5 eV.

Small value of MOKE and material constant K suggests that there is a reduction of spin-orbit splitting in Ni-ferrites. Note that found K is about one order smaller compared to PMOKE of 3d-metals, corresponding to small spin-orbit splitting in $NiFe_2O_4$, which we attribute to small orbital angular momentum of both Ni and Fe

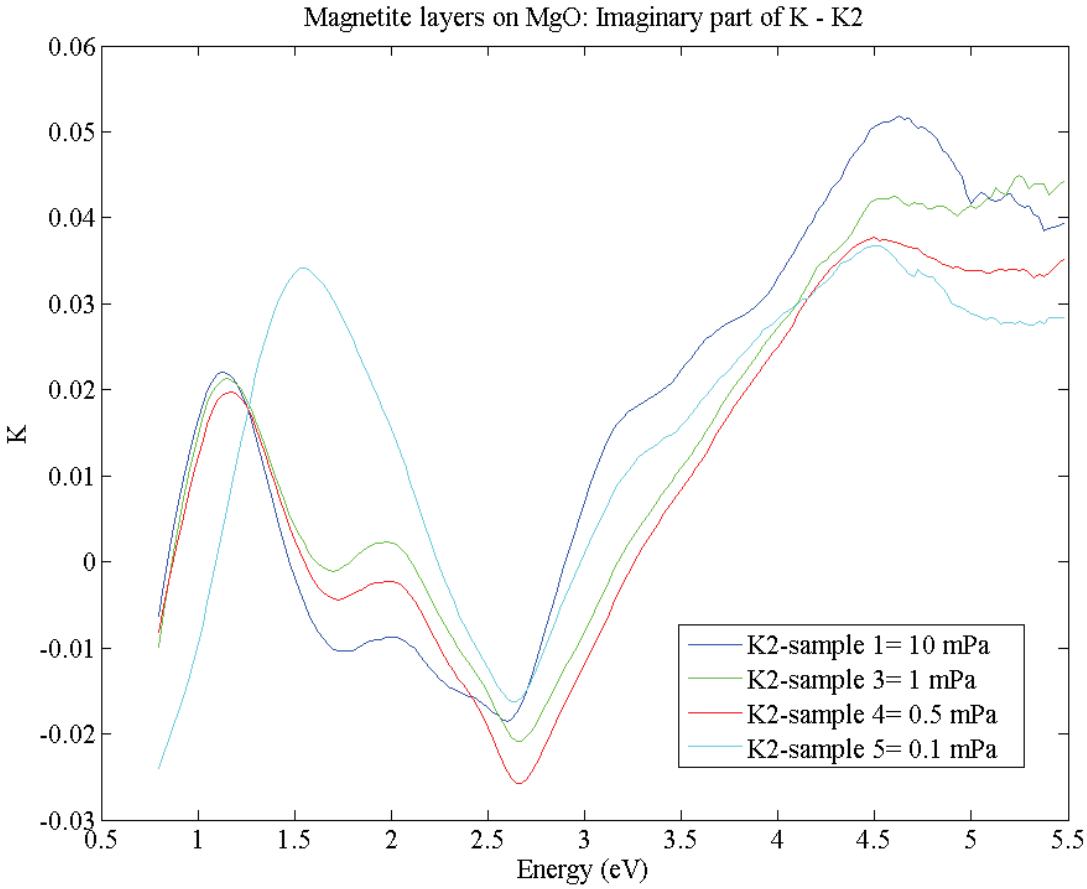

Figure 3.52: *The dependence of imaginary part of material constant K on energy for the first magnetite set of samples.*

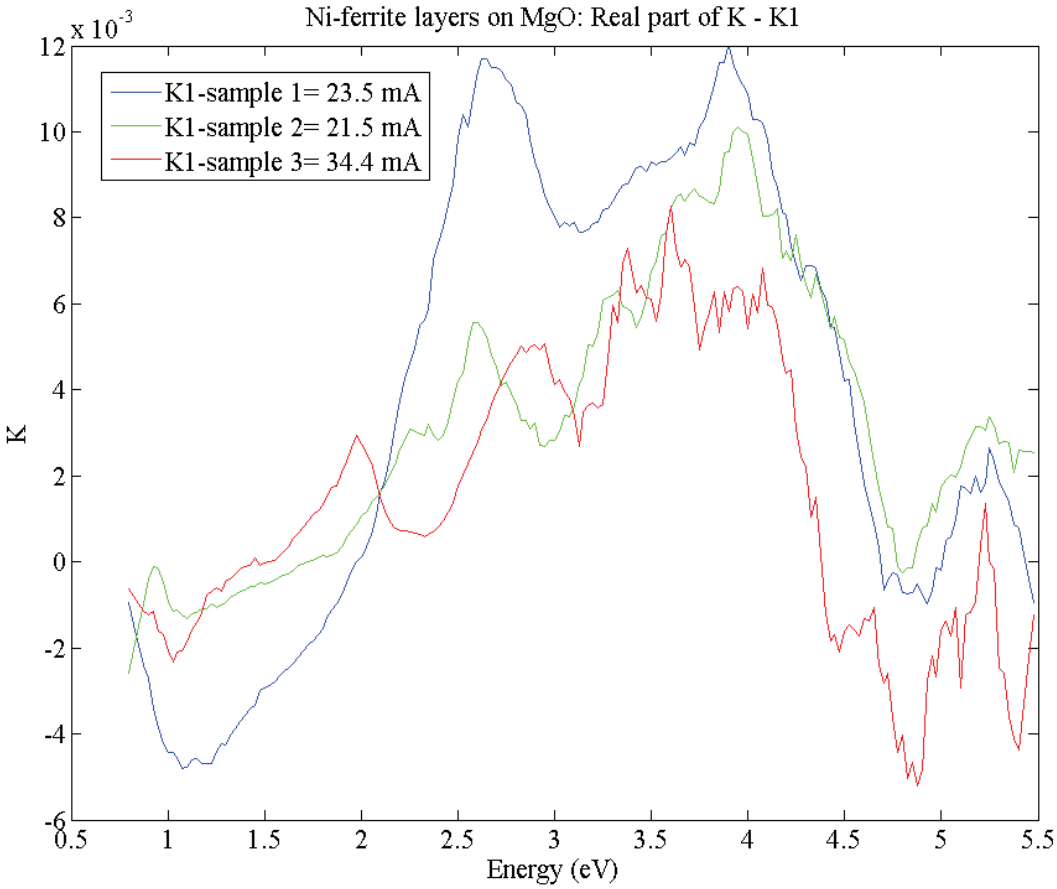

Figure 3.53: *The dependence of real part of material constant K on energy for the second Ni-ferrite set of samples.*

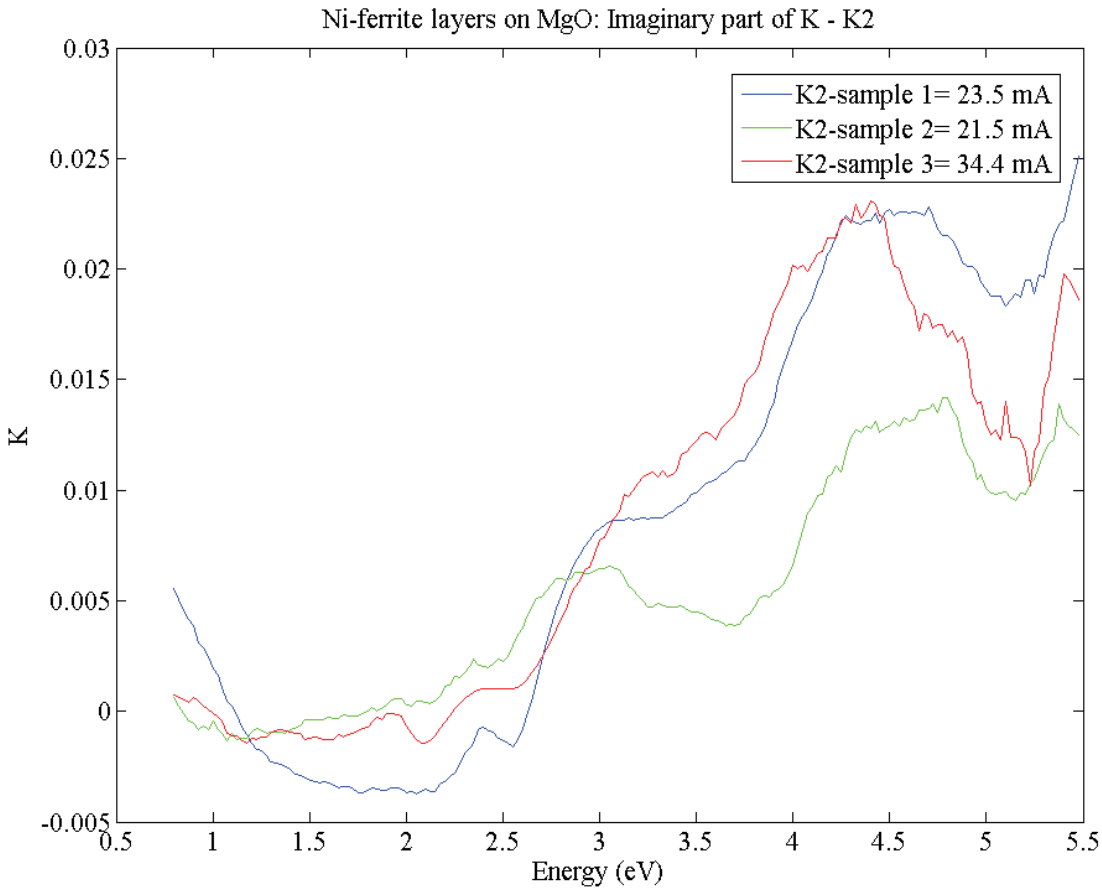

Figure 3.54: *The dependence of imaginary part of material constant K on energy for the second Ni-ferrite set of samples.*

atoms, which are located inside spinel structure. [67]

4 Conclusion

The goal of this thesis was to prepare epitaxial thin films of magnetite and Ni-ferrite on MgO(001) substrate. Two sets of samples were prepared. Five samples of magnetite layers on MgO substrate from the first set were deposited at different pressures of oxygen in deposition chamber during deposition process. The second set contains three samples of Ni-ferrite on MgO substrate, which were deposited at different amount of Fe in deposition chamber. Namely, the value of Fe flux and emission was changed for each Ni-ferrite sample.

AFM and XRR data provided us information about roughnesses and thicknesses of prepared samples. The values of roughnesses obtained by AFM and XRR are slightly different, nevertheless all values of roughnesses are very small, usually around 2.5 nm or lower. One exception is value of roughness 5.8 nm that was obtained using AFM of Ni-ferrite sample 1 (the second set). A possible explanation for the discrepancy between the rougness values is that AFM is a local probing technique and XRR gives us average value of rougness from entire sample. Thus, the values may differ.

The calculated XRR data provide models for the samples, where two other layers are needed to describe the data next to the MgO. The first layer correspond to deposited layer and the second layer can denote a layer of impurities on the top of the oxide film. However, the second layer is usually very thin, typically below 1 nm with exception of magnetite sample 3 (5.96 nm) , sample 4 (1.6 nm) and Ni-ferrite sample 3 (1.8 nm). At sample 3 (1.8 nm) of Ni-ferrite layer, the higher amount of impurities could be caused by longer exposure to ambient conditions.

Magnetite and Ni-ferrites are iron oxides, providing inverse spinel structure. In electron diffraction pattern the structure of this structure shows a $(\sqrt{2} \times \sqrt{2})$R45° structure, while clean MgO exhibits a (1×1) structure.

The magnetite sample of the first set exhibit a $(\sqrt{2} \times \sqrt{2})$R45° structure and thus, we conclude it crystallizes in the inverse spinel structure. The best diffraction pattern with sharp spots and low diffuse background intensity is observed for magnetite sample 3 (1 mPa of oxygen pressure) and 4 (0.5 mPa of oxygen pressure). Hence, we conclude that these are the best preparation conditions for magnetite.

In the diffraction patterns of samples 1 (500 nA of Fe flux) and 3 (5000 nA of Fe flux) from the second set the structure (1×1) with weak $(\sqrt{2} \times \sqrt{2})$R45° structure is observed. Sample 2 (300 nA of Fe flux) exhibits at reciprocal space clear (1×1) structure. After this, sample does not crystallize at inverse spinel structure. Therefore, it seems like the crystalline quality of pure magnetite cannot be reached by MBE preparation of the ferrites.

VSM data reveal rather large dependence of saturation magnetization on preparation procedure (for both magnetite and nickel-ferrite). This is rather surprising as optical techniques (ellipsometry, MOKE spectroscopy) provide relatively small dependence on preparation procedure (and particularly MOKE spectroscopy is usually very sensitive to details in magnetic properties). Namely, in case of Ni-ferrite, the saturation magnetization for samples prepared at different Fe flux differs by factor 9, such a large change of properties between different $NiFe_2O_4$ samples was not observed by other techniques we have used for our investigations. In case of Fe_3O_4, we found that saturation magnetization is smaller than expected for bulk material, showing imperfections in spin arrangement of the material in comparison with bulk crystallite magnetite. On the other hand, with exception of sample prepared at pressure 0.1mPa, the coercivity of Fe_3O_4 was found low, suggesting that magnetic material is homogeneous, allowing free propagation of domain walls.

The ellipsometric data were processed using the function B-spline, where the obtained values of thicknesses and roughnesses were used. The dependence or dielectric function on energy was drawn for every samples. Imaginary part of permittivity is associated with absorption of material. The values of permittivity and course of the curves of magnetite samples were very similar for each sample, with exception of sample 1 (the lowest oxygen pressure 0.1 mPa). At the second set of Ni-ferrite samples the dependencies of permittivity on energy have very similar course.

Using the Linear MOKE the dependencies of Kerr rotation and Kerr ellipticity on energy were measured. Further, these values were used to calculate the material constant K. The Kerr ellipticity and real part of material constant K correspond to absorption of material. Comparing of sample 5 (0.1 mPa of oxygen pressure) with other samples of the first magnetite set, this sample has little different behaviour than another samples.

In conclusion, small value of MOKE and material constant K of the second set of samples suggests that there is a reduction of spin-orbit splitting in Ni-ferrites and how was mentioned in previous text, K is about one order smaller compared to PMOKE of 3d-metals, corresponding to small spin-orbit splitting in $NiFe_2O_4$, which we attribute to small orbital angular momentum of both Ni and Fe atoms, which are located inside spinel structure.

References

[1] Krpoun Karel. Iron and its compounds. Master's thesis, VUT Brno, 2008.

[2] D. Vojtěch. Struktura, vlastnosti a zpracování kovových materiálu. *VĹ CHT Praha*, (ISBN 80-7080-568-4), 2005.

[3] Kolouch M. Základy krystalografie. krystalografická stavba látek., 2006.

[4] SvobodovĂ˘ Anna. Ĺ″elezo., 2009.

[5] Sakaguchi et al. Genes produce nanocrystals: Sulfate-reducing bacteria. *Ask Nature*, 2002.

[6] Mineral Website. Maghemite mineral data, 2000.

[7] John Bland. Investigation into the crystal and magnetic structure of magnetite (fe3o4) using mosssbauer spectroscopy, 1998. Description of Magnetite Structure.

[8] Bc. Cabáková Silvie. Nestechiometrie nanočăstic Îł-fe2o3 a fe3o4 a jejich projev v jejich magnetickšch vlastnostech. Master's thesis, Palacký University Olomouc, https://theses.cz/id/0lpmm6/Diplomka-Silvie$_C$*abakova.txt*, 2012.

[9] Bc. Kašlík Josef. Teplotně indukované strukturní změ ny v systé mu magnetit - maghemit. Master's thesis, Palacký University Olomouc, 1993.

[10] Kocián Karel. The study of degasing process during thermal treatment of advanced ceramic. Master's thesis, VUT Brno, 2013.

[11] Onyenwoke. Magnetite: Structure, properties and applications. 2010.

[12] Division of Spang and Company. A critical comparison of ferrites with other magnetic materials. Technical report, Magnetics, 2000.

[13] European Commission. Definition of a nanomaterial, 2 2016.

[14] Gusev Alexander I. Nanostructured materials, 2011.

[15] doc. Dr. Mgr. Kamil Postava. Thin films. Learning text, 2014.

[16] Epitaxy. Epitaxial growth., 2002. Textbook.

[17] J.E. Greene. Thin solid films, 1999. 0040-6090.

[18] Moravcová Z. Types of nanoobjects and their clasifications, 2015.

[19] Knotek M. Gallium-nitride thin-film deposition on substrates structured by electron beam lithography. Master's thesis, VUT Brno, 2013.

[20] Brian S. Mitchell Claudio L. De Castro. *Nanoparticles from Mechanical Attrition*. 2002 2002.

[21] Paul Fry. Electron beam lithography. principles of operation. patterning of electron sensitive resists., 2016.

[22] Pinos Jakub. Microstructural stability of mg-alloys prepared by several plastic deformation. Master's thesis, VUT Brno, 2011.

[23] J. R. Creighton and P. Ho. *Introduction to Chemical Vapor Deposition (CVD)*. Sandia National Laboratories, 2001.

[24] Lifshits V.G. Saranin A. Zotov A.V. Katayama M. Oura, K. *Surface Science*, volume XII, 440 of *1439-2674*. Springer-Verlag Berlin Heidelberg, 1 edition, 2003.

[25] Milton Ohring. *Materials Science of Thin Films*. 2nd. 2016 Elsevier B.V., 2007.

[26] Dvořák Martin. Deposition of ga and gan ultrathin layers on graphene substrates. Master's thesis, VUT Brno, 2003.

[27] Brian K. Jones G.P. Zhigalskii. The physical properties of thin metal films, 2003.

[28] Major differences. Distinguish between physical adsorption and chemisorption, 2015.

[29] The Editors of Encyclopedia Britannica. Adsorption. surface phenomenon., 1994.

[30] Paul A. Webb. Introduction to chemical adsorption analytical techniques and their applications to catalysis. *Micromeritics Instrument Corp., Norcross, Georgia 30093*, January 2003. MIC Technical Publications.

[31] Physics and Technology of Thin Films. Condensation and thin film growth. 1992.

[32] Justinas Palisaitis. Epitaxial growth of thin films. *Linkoping University, Sweden*, 2004. Physics of Advanced Materials Winter School.

[33] Chris Woodford. Molecular beam epitaxy, December 2015.

[34] The University Warwick. Pvd - physical vapour deposition, 1996. Department of Physics.

[35] Robert Chow Walter S. Knodle. *Molecular Beam* $Epitaxy_E quipmentandPractice.$ 2000.

[36] Vá vra Roman. Electronic microscopy and microanalysis, 2013.

[37] Křepelka Jaromír. Př ehled použ ítí tenkých vrstev. *Palacký University Olomouc*, 2014.

[38] D. T. Attwood E. M. Gullikson M. R. Howells J. B. Kortright Y. Liu A. C. Thompson, J. Kirz and A. L. Robinson;. X-ray reflection, 1997. X-ray data booklet.

[39] Bruker Comporation. X-ray reflectivity (xrr), 2001.

[40] Neill Serman. Production of x-rays and interactions of x-rays with matter. page 20, 1998.

[41] Materials Research Laboratory UCSB. Philips xpert mpd, 2016. UC Santa Barbara.

[42] Stack Exchange Inc. X-ray diffraction analytical principle, 2016.

[43] Mike Roger Smart Stewart McIntyre Mike Bancroft Igor Bancroft Igor Bello Roger Smart, Stewart McIntyre. X-ray photoelectron spectroscopy ray photoelectron spectroscop, 1992.

[44] Matějka Pavel. Photoelectron spectroscopy esca, ups and auger spectroscopy, 1995.

[45] Jaroslav Reichl. De broglie hypothesis, 2002.

[46] KubĂnek R. The basic principle of spm. page 14, 2004.

[47] Wenjie Mai. Fundamental theory of atomic force microscopy, 1998.

[48] Nanoscience Instruments. How an afm works, 2016.

[49] CSI Company. Nano-observer afm microscope. the atomic force awakens, 2001.

[50] Macmillan Publishers. Magnetic materials, 2016.

[51] Electricity and Magnetism. Dielectric and magnetic polarization, 2003. Texbook.

[52] Fedorov Alexey. Production of manganese-zinc ferrits and influence of composition on their properties. 2011.

[53] NDT Resource Center. Diamagnetic, paramagnetic, and ferromagnetic materials, 2005. Introduction to Magnetic Particle Inspection.

[54] IJERT. Pspice simulation of vibrating sample magnetometer circuitry. *International Journal of Engineering Research and Technology*, Vol.2 - Issue 9(2278-0181), 2000.

[55] MicroSense. Vibrating sample magnetometer (vsm), 2016.

[56] J.A. Woollam Co. Spectroscopic ellipsometer, 2008.

[57] J-P. Gaston L.Yan E. Garcia-Caurel, A. De Martino. Application of spectroscopic ellipsometry and mueller ellipsometry to optical characterization. 1999.

[58] Jakob Bork Tobias Holmgaard Niels Anker Kortbek Kjeld Pedersen, Jesper Jung. Ellipsometry. *AALBORG UNIVERSITY, Institute of Physics and Nanotechnology*, (7):132, 2001.

[59] N.N. Magneto-optical kerr effect (moke), 2013.

[60] Prof. Dr. B. Hillebrands. Magneto-optic kerr effect magnetometry and microscopy (moke), 2006. Deparment of Physik.

[61] I. Berthold. Principle of operation of the moke measurements, 1996.

[62] Topac Inc. Miniature knudsen cell - molecular effusion source, 1999.

[63] Eric Gullikson. X-ray interactions with matter, 2015. X-Ray Database.

[64] G. Y. Guo Horng-Tay Jeng. First-principles investigations of the electronic structure and magnetocrystalline anisotropy in strained magnetite fe3o4. *PHYSICAL REVIEW B, VOLUME 65, 094429*, Semptember 2001.

[65] R. J. Choudhary I. V. Shvets O. N. Mryasov Hongzhi Yao S. K. Arora, Han-Chun Wu and W. Y. Ching. Giant magnetic moment in epitaxial fe3o4 thin films on mgo(100). 2008. PHYSICAL REVIEW B 77, 134443 2008.

[66] O. Gaier B. Hillebrands R. Schafer M. Jourdan J. Hamrle, S. Blomeier. Magnetic anisotropies and magnetization reversal of the $co_2cr_{0.6}fe_{0.4}alheuslercompound.JOURNALOFAPPLIEDPHYSICS100, 103904, 2006.$

[67] D. Kodderitzsch A. Svane L. Petit Z. Szotek, W. M. Temmerman and H. Winter. Electronic structures of normal and inverse spinel ferrites from first principles. *Phys. Rev. B 74, 174431*, 2006.